Technische Universität Braunschweig

pvz Zentrum für Pharmaverfahrenstechnik

4th International Symposium on Pharmaceutical Engineering Research

SPhERe

CONFERENCE PROCEEDINGS

15 – 17 September 2021

OPEN ACCESS EDITION

TU Braunschweig • Center of Pharmaceutical Engineering

https://doi.org/10.24355/dbbs.084-202110251021-0

Notes on Content of SPhERe Conference Proceedings

Conference abstracts authorised for Open Access Publication are listed alphabetically according to the surname of the presenting author. The names of the presenting authors are underlined in each conference presentation.

https://doi.org/10.24355/dbbs.084-202110251021-0

Table of Contents

https://doi.org/10.24355/dbbs.084-202110251021-0

VALIDATING THE CRYOPRESERVATION OF TISSUE ENGINEERED CONSTRUCTS WITHIN CRYOBAGS

S.-A. Barker[1,2], B. Glasmacher[1,2,3], O. Gryshkov[1,2]

[1] Institute for Multiphase Processes, Leibniz University Hannover; An der Universität 1; 30823 Garbsen; Germany; barker@imp.uni-hannover.de, glasmacher@imp.uni-hannover.de, gryshkov@imp.uni-hannover.de

[2] Lower Saxony Center for Biomedical Engineering, Implant Research and Development; Stadtfelddamm 34; 30625 Hannover; Germany

[3] Center of Pharmaceutical Engineering; Franz-Liszt-Str. 35a; 38106 Braunschweig; Germany

ABSTRACT

The cryopreservation of cells and tissue engineered constructs is determined by multiple factors, such as possible cellular damages due to mass and heat transfer during the freezing and thawing process. It is assumed that the utilization of cryobags improves the heat transfer during freezing and thawing and is therefore superior in comparison to currently applied cryovials and multiwell plates. Therefore, we have analysed the cryopreservation of cell-seeded electrospun polycaprolactone/polylactide scaffolds within cryobags. Additionally, the performance of four different cryoprotective agents was analysed, which included 10% (v/v) dimethyl sulfoxide and 10% (v/v) ethylene glycol as separately applied agents as well as their combination with 0.3 M sucrose. The samples were frozen in in-house made cryobags with a controlled rate freezer. The cell viability was analysed by fluorescence microscopy before freezing and after thawing. The results show, that the application of cryobags in combination with 10% (v/v) ethylene glycol can have a positive impact onto the cell viability.

Keywords: cryopreservation, cryobags, tissue engineered constructs, cryoprotective agents, cell viability

INTRODUCTION

In recent years, the development and analysis of tissue engineered constructs (TECs) has increased within regenerative medicine [1], as TECs hold the potential application as substitutes for the regeneration of tissue defects [2-4]. Especially the development of suitable scaffolds is of upmost importance. A desired cell type is seeded onto the scaffolds' surface and proliferates *in vitro*. Finally, the scaffolds can be applied to the defective site [5]. Regarding this methodical approach, the electrospinning method is a widely utilized and versatile scaffold fabrication technique. Thereby a thin fibre is formed out of a polymeric solution due to the application of an electric field and is collected. Dependent upon the set process parameters, the fibre mats can be tailored [6-8].

However, a remaining challenge is the long-term storage of biological products. Currently, the frequently applied hypothermic preservation methods do not allow a sufficient long-term storage [9, 10]. Therefore, new preservation methods have to be evolved in order to ensure a sufficient availability of TECs. A possible alternative to overcome these limitations in storing duration of TECs is cryopreservation. This method enables the storage at sub-zero temperatures, thus reducing metabolic activity and increasing the shelf-life. It has to be noted though, that also this preservation method is influenced by various parameters [11, 12]. Due to the cryogenic conditions as well as due to multiple parameters, such as mass and heat transfer during freezing and thawing, cellular injury can occur [13, 14]. A possibility to enhance the heat transfer is the utilization of cryobags since they possess a comparably flatter structure. However, different cell types have already been cryopreserved within cryobags [15-19] but to the field of TECs this method is fairly new and the various influences of the preservation method onto the specimen have to be investigated further.

Therefore, the aim of this study was to analyse the viability of cryopreserved cells, seeded onto electrospun scaffolds and stored within cryobags as well as the impact of different cryoprotective agents (CPAs). The results were compared to previous studies of our group, in which the cell-seeded TECs were cryopreserved within multiwell plates.

https://doi.org/10.24355/dbbs.084-202110251021-0

RESEARCH CONCEPT

Electrospinning and sample preparation

The scaffolds were fabricated by electrospinning. Polycaprolactone (PCL, from Aldrich) with an average Mn of 80,000 and polylactic acid (PLLA, from Natureplast) with an average Mn of 150,000 were dissolved in 2.2.2-trifluoroethanol (TFE, from abcr) with a mass concentration ratio of 100:50 (mg ml^{-1}: mg ml^{-1}). The solution homogenized for 24 h before electrospinning.

Electrospinning was performed in a horizontal orientation. The polymer solution was ejected through a metallic needle (0,8 mm inner diameter, from B. Braun) at an applied flow rate of 3 ml h^{-1} and a voltage of 15 kV with a spinning distance of 21 cm and a duration of 100 min. The fibres where collected on a rotating drum collector at 220 rpm.

Finally, the electrospun fibre mats were UV sterilized on each side for a duration of 15 min and punched into 16 mm scaffolds.

Cryopreservation

SaOS-2 cells were utilized for the viability analysis. The cells were seeded onto the surface of the electrospun scaffolds at a density of 5×10^4 cells cm^{-2} and proliferated for 3 days under physiological conditions in an incubator before cryopreservation. Control samples were analysed before preservation.

Prior to cryopreservation, the samples were loaded with different CPA-solutions (Table 1) at 4°C for 10 min, before being transferred into cryobags (ProfiCook) and cooled in a controlled rate freezer (Planer) at 1 K min^{-1} to -100°C, then being plunged into liquid nitrogen and stored at -140°C in a cryogenic freezer (Fisher Scientific). Every cryobag contained four identical TECs and was frozen in our previously described "in-air" method [20].

After low temperature storage the TECs were rapidly thawed in a water bath at 37°C for 15 s. The samples were placed in multiwell plates (TPP) containing warm culture medium and incubated for 5 min. The medium was refreshed and the samples were cultured for 24 h before the viability analysis.

Cell viability analysis

The cell viability was analysed by live-dead assay with a fluorescence microscope (Zeiss). Prior to staining, the samples were washed twice in 2 ml PBS before and after applying the staining solution. Calcein AM (Biotium) and Ethidium Homodimer-1 (Aldrich) served as fluorescence dyes. Images were taken in a z-stack mode and the cell viability was analysed with the ImageJ software (NIH).

Table 1: Four different CPA solutions were prepared. Dimethyl sulfoxide (DMSO, from Roth) and ethylene glycol (EG, from Aldrich) with and without sucrose (Suc, from Aldrich). All solutions contained 20% fetal bovine serum (FBS, from Biochrom) and Dulbecco's Modified Eagle Medium (DMEM, from Biochrom). Values in percent are v/v.

Solution	DMSO	EG	Suc
DMSO	10%	-	-
DMSO+Suc	10%	-	0.3 M
EG	-	10%	-
EG+Suc	-	10%	0.3 M

Data analysis and statistics

All data were collected from four individual experiments and are represented as the mean and standard deviation.

RESULTS

Cell viability analysis

Two different morphologies of attached cells were present on the TECs surface. The dominant cell morphology had a round shape, but also stretched cells were visible. Additionally, the cells were also partially aligned in fibre orientation. It was discovered, that the cell morphology was not affected by the cryopreservation process.

On day 3, a viability of 97% ± 2% could be obtained for the cultivated cell-seeded TECs prior to cryopreservation, serving as a control.

After the cryopreservation and recultivation, the post-thaw cell viability was influenced by the applied CPA-solution. In this study, the highest cell viability with a mean value of 80% ± 11% could be obtained with 10% (v/v) EG as well as its combination with 0,3 M sucrose (79% ± 7%), respectively. In comparison, the application of 10% (v/v) DMSO yielded in a post-thaw viability of 77% ± 6%. Combining DMSO with sucrose lead to a viability of 78% ± 7%.

It has to be noted, that the post-thaw viability can be influenced by rupture of the cryobags during the thawing procedure and will yield in a reduced viability.

Generally, the trend of viability also corresponds with the number of total cells. This indicates that the highest

https://doi.org/10.24355/dbbs.084-202110251021-0

post-thaw cell number was present for a CPA-solution containing 10% (v/v) EG as well as its combination with sucrose.

Figure 1: Post-thaw viability. n=64 ([1]n=44, [2]n=60)

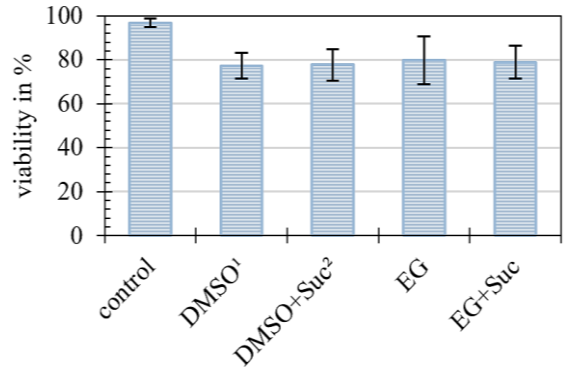

Figure 2: Representative live-dead images. Control (left) and 10% (v/v) EG (right). Scale bars are 150 µm.

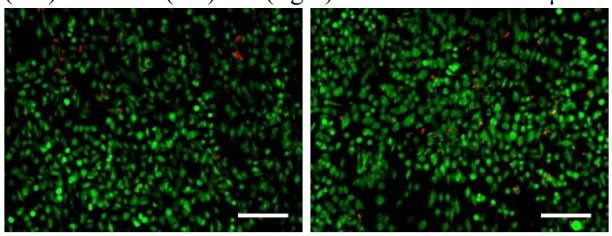

DISCUSSION

Within the field of cryobiology, the application of CPAs is of vital importance in order to achieve a sufficient post-thaw viability. In this study, all analysed CPA-solutions enabled a viability of >70%. Furthermore, the highest viability was obtained for solutions containing 10% (v/v) EG. Since the applied concentrations of DMSO and EG are identical and the membrane permeation is known to dependent upon the molecular weight of the CPA [21], this could provide an explanation for the obtained viability. Therefore, EG could provide a suitable alternative to DMSO, which is known to induce a toxic effect above 4°C [22]. However, possible toxic effects of EG on the cells should still be elaborated in future. Furthermore, sucrose only had a subdominant effect on the viability. This correlates with previous findings [23]. It is also known, that the diffusion rate of sucrose into tissue is lower than other CPAs such as DMSO [24].

The utilization of cryobags holds a promising approach to increase the post-thaw cell viability. Compared to current cryopreservation methods in cryovials or in multiwell plates, the cryobags possess the advantage of being customizable to the individual volume and geometry of each sample. It has to be noted though, that the cryobag material can be potentially susceptible to rupture during the thawing process and can cause cell loss, as discovered in our study. The material failure has also been previously described by other authors [25, 26]. In this current study, a possibility to overcome this limitation was achieved be thawing in a warm PBS bath. Previously our group also cryopreserved TECs within multiwell plates. A comparison indicates that a higher post-thaw viability could be obtained within the cryobags (data not shown). Therefore, cryobags seem to improve the heat transfer and thus enable an enhanced cryopreservation outcome.

CONCLUSIONS

The current cryopreservation methods enable the long-term storage of cell-seeded TECs. In view of the utilized CPAs, 10% (v/v) EG offers a suitable alternative to the commonly applied but more toxic DMSO. Also, the application of sucrose can have a beneficial impact onto the cell viability. Regarding the storage method of TECs, cryobags improve the post-thaw cell viability compared to multiwell plates, and therefore represent an alternative preservation method.

ACKNOWLEDGMENT

This work was supported by the Lower Saxony Ministry of Science and Culture (“HypSpin”, project number 98009).

REFERENCES

[1] Dlaska, C. et al. (2015): Clinical translation in tissue engineering – The Surgeon’s View. In: Curr. Mol. Bio. Rep. 1 (2), S. 61–70. DOI: 10.1007/s40610-015-0013-3.

[2] Miszuk, J. et al. (2018): Functionalization of PCL-3D electrospun nanofibrous scaffolds for improved BMP2-induced bone formation. In: Appl. Mater. Today 10, S. 194–202. DOI: 10.1016/j.apmt.2017.12.004.

[3] Schofer, M. et al. (2011): Electrospun PLLA nanofiber scaffolds and their use in combination with BMP-2 for reconstruction of bone defects. In: PLoS One 6 (9), S. 1–9. DOI: 10.1371/journal.pone.0025462.

[4] Yao, Q. et al. (2017): Three dimensional electrospun PCL/PLA blend nanofibrous scaffolds with significantly improved stem cells osteogenic differentiation and

https://doi.org/10.24355/dbbs.084-202110251021-0

cranial bone formation. In: Biomaterials 115; S. 115–127. DOI: 10.1016/j.biomaterials.2016.11.018.

[5] van Belleghem, S. et al. (2020): Overview of tissue engineering concepts and applications. In: Biomaterials Science; Wagner, W. R.; Sakiyama-Elbert, S. E., Zhang, G.; Yaszemski, M. J. (eds.), S. 1289–1316. DOI: 10.1016/B978-0-12-816137-1.00081-7.

[6] Ma, Z. et al. (2005): Potential of nanofiber matrix as tissue-engineering scaffolds. In: Tissue Eng. 11 (1-2), S. 101–109. DOI: 10.1089/ten.2005.11.101.

[7] Peijs, T. (2017): Electrospun polymer nanofibers and their composites. In: Comprehensive Composite Materials II; Zweben, C. H.; Beaumont, P. (eds.), S. 162–200. DOI: 10.1016/B978-0-12-803581-8.10025-6.

[8] Xue, J. et al. (2019): Electrospinning and electrospun nanofibers: Methods, materials, and applications. In: Chem Rev 119 (8), S. 5298–5415. DOI: 10.1021/acs.chemrev.8b00593.

[9] Pogozhykh, D. et al. (2015): Influence of factors of cryopreservation and hypothermic storage on survival and functional parameters of multipotent stromal cells of placental origin. In: PloS one 10 (10); S. 1–16. DOI: 10.1371/journal.pone.0139834.

[10] Van Buskirk, R. et al. (2004): Hypothermic storage and cryopreservation. In: Bioprocess Int. 2, S. 42–49.

[11] Baust, J. et al. (2009): Cryopreservation: An emerging paradigm change. In: Organogenesis 5 (3), S. 90–96. DOI: 10.4161/org.5.3.10021.

[12] Hunt, C. (2019): Technical considerations in the freezing, low-temperature storage and thawing of stem cells for cellular therapies. In: Transfus. Med. Hemother. 46 (3), S. 134–150. DOI: 10.1159/000497289.

[13] Mazur, P. et al. (1972): A two-factor hypothesis of freezing injury. In: Exp. Cell Res. 71 (2), S. 345–355. DOI: 10.1016/0014-4827(72)90303-5.

[14] Gao, D. et al. (2000): Mechanisms of cryoinjury in living cells. In: ILAR J. 41 (4), S. 187–196. DOI: 10.1093/ilar.41.4.187.

[15] Heidemann, R. et al. (2010): Characterization of cell-banking parameters for the cryopreservation of mammalian cell lines in 100-ml cryobags. In: Biotechnol. Prog. 26 (4), S. 1154–1163. DOI: 10.1002/btpr.427.

[16] Junker, B. et al. (2002): Use of frozen bagged seed inoculum for secondary metabolite and bioconversion processes at the pilot scale. In: Biotechnol. Bioeng. 79 (6), S. 628–640. DOI: 10.1002/bit.10323.

[17] Massie, I. et al. (2014): GMP cryopreservation of large volumes of cells for regenerative medicine: active control of the freezing process. In: Tissue Eng Part C Methods 20 (9), S. 693–702. DOI: 10.1089/ten.tec.2013.0571.

[18] Ninomiya, N. et al. (1991): Large-scale, high-density freezing of hybridomas and its application to high-density culture. In: Biotechnol. Bioeng. 38 (9), S. 1110–1113. DOI: 10.1002/bit.260380920.

[19] Solanki, P. et al. (2017): Thermo-mechanical stress analysis of cryopreservation in cryobags and the potential benefit of nanowarming. In: Cryobiology 76, S. 129–139. DOI: 10.1016/j.cryobiol.2017.02.001.

[20] Mutsenko, V. et al. (2020): Effect of 'in air' freezing on post-thaw recovery of callithrix jacchus mesenchymal stromal cells and properties of 3D collagen-hydroxyapatite scaffolds. In: Cryobiology 92, S.215–230. DOI: 10.1016/j.cryobiol.2020.01.015.

[21] Wang, S. et al. (2014): Protein stability in stored decellularized heart valve scaffolds and diffusion kinetics of protective molecules. In: Biochim. Biophys. Acta 1844 (2), S. 430–438. DOI: 10.1016/j.bbapap.2013.11.016.

[22] Best, B. (2015): Cryoprotectant toxicity: Facts, issues, and questions. In: Rejuvenation Res. 18 (5), S. 422–436. DOI: 10.1089/rej.2014.1656.

[23] Newton, H. et al. (1998): Permeation of human ovarian tissue with cryoprotective agents in preparation for cryopreservation. In: Hum. Reprod. 13 (2), S. 376–380. DOI: 10.1093/humrep/13.2.376.

[24] Vásquez-Rivera, A. et Al. (2018): Simultaneous monitoring of different vitrification solution components permeating into tissues. In: Analyst 143, S. 420–428. DOI: 10.1039/c7an01576c.

[25] Khuu, H. et al. (2002): Catastrophic failures of freezing bags for cellular therapy products: description, cause, and consequences. In: Cytotherapy 4 (6), S. 539–549. DOI: 10.1080/146532402761624700.

[26] Leemhuis, T. et al. (2014): Essential requirements for setting up a stem cell processing laboratory. In: Bone Marrow Transplant. 49 (8), S. 1098–1105. DOI: 10.1038/bmt.2014.104.

https://doi.org/10.24355/dbbs.084-202110251021-0

SDS AFFECTS THE PHYSICOCHEMICAL PROPERTIES OF PVA-STABILIZED SOLID TRIGLYCERIDE NANOPARTICLES

N. Bauer[1,2], H. Bunjes[1,2]

[1] Technische Universität Braunschweig / Institut für Pharmazeutische Technologie und Biopharmazie; Mendelssohnstr. 1; 38106 Braunschweig / Germany; n.bauer@tu-braunschweig.de; heike.bunjes@tu-braunschweig.de
[2] Technische Universität Braunschweig, Zentrum für Pharmaverfahrenstechnik – PVZ; Franz-Liszt-Str. 35a, 38106 Braunschweig / Germany

ABSTRACT

Solid triglyceride nanoparticles are under intensive investigation as drug delivery systems. In the solid state, triglycerides exist in three polymorphic modifications which differ from each other in their physicochemical properties. Thus, it is particularly important to know the influence of parameters affecting the polymorphic behavior of the solid triglyceride nanoparticles to get a stable product with defined physicochemical properties over an appropriate storage time. This study investigated the effect of subsequent addition of SDS to tripalmitin nanoparticles, which had been stabilized with partially hydrolyzed poly(vinyl alcohol) (PVA). The polymorphic behavior was characterized with DSC and X-ray diffraction over a storage time of 28 d at 20 °C. A faster transition into more stable polymorphic modifications was observed after the addition of SDS to the nanoparticles.

Keywords: triglycerides, polymorphism, PVA, SDS

INTRODUCTION

Nanoparticles of solid lipids were first investigated by Speiser et al. [1986] and further developed as potential drug delivery systems for poorly water-soluble drugs [Bunjes, 2010]. The physicochemical properties of the nanoparticles depend on, e.g., the used matrix lipid, the stabilizer as well as additional substances. As matrix lipid e.g., triglycerides can be used. Triglycerides are polymorphic substances and mainly occur in three different polymorphic modifications. These modifications differ from each other in their physicochemical properties due to a different arrangement of the triglyceride molecules [Chapman, 1962]. According to Ostwald's step rule, triglycerides crystallize in the metastable α-modification and undergo time- and temperature dependent monotropic transitions into the stable β-modification, sometimes via the β'-modification. The different physicochemical properties of the solid triglyceride particles when present in different crystal modifications might influence the drug loading capacity as well as the physical stability of the dispersion. Therefore, it is essential to understand the effect of additives to obtain a stable product over the necessary shelf life. In this study, tripalmitin was used as matrix lipid and the nanoparticles were stabilized with partially hydrolyzed poly(vinyl alcohol). SDS was added to the dispersions to investigate the effect on the physicochemical behavior of the PVA-stabilized nanoparticles and to get further information about how PVA interacts with the matrix lipid.

RESEARCH CONCEPT

For this study, dispersions consisting of 5 % tripalmitin (Dynasan® 116, Condea), 5, 7.5, 10 or 15 % Kuraray Poval 3-83 (Kuraray Europe GmbH) and bidestilled water, in which the PVA was dissolved, were prepared by high pressure melt homogenization (all concentrations w/w). To each dispersion 0.1 or 0.3 % SDS (Carl Roth GmbH) was added after the homogenization procedure as described in this section. A dispersion without SDS was used as reference.

First, the lipid and the aqueous phase were heated at approx. 80 °C separately. Afterwards, both phases were combined and pre-homogenized with an ultra-turrax (IKA T25 digital Ultra-Turrax; SN25-10G, IKA-Werke) at 13.000 rpm for 4 min. The premix was homogenized in a preheated Microfluidizer M110-P instrument (Microfluidics) for 10 cycles at 800 bar. The hot dispersion was divided into three parts. To two parts

https://doi.org/10.24355/dbbs.084-202110251021-0

SDS in the respective concentration was added as a powder in the heat and dissolved under gentle shaking. In a following cooling step, the matrix lipid was allowed to crystallize in an ice-water bath.

The particle size was measured with a Zetasizer Nano ZSP instrument (Malvern) at 25 °C and an angle of 173 °. The dispersions were diluted with purified and particle free water. The z-average diameter and PDI were given as mean of three measurements of 5 min each after 5 min of equilibration.

Differential scanning calorimetry (DSC) measurements were performed in a DSC 3 Star^e System with a full range sensor (FRS 6+) and a sample robot (Mettler Toledo GmbH). 15 µl of the dispersions were accurately weighed into aluminum crucibles that were cold sealed. The samples were heated from 0 to 85 °C with a heating rate of 10 K/min, held at that temperature for 10 min and cooled to -5 °C with a cooling rate of 10 K/min. As a reference, an empty aluminum pan was used, and all measurements were performed under nitrogen purge. The enthalpies obtained as areas under the curve upon evaluation were normalized for the weight of the samples.
The melting enthalpies were used to approximate the formation of particles in the stable β-modification.

X-ray measurements were performed with a small- and wide-angle X-ray diffraction setup (SAXSess mc², Anton Paar) equipped with a copper radiation source (λ = 0.154 nm) and a CCD detector as well as a Mythen detector. The sample was measured in a quartz capillary sample holder in 20 runs of 60 s each at 20 °C. Background subtraction and desmearing was performed for all diffractograms.

RESULTS

All dispersions had a milky white appearance. However, the more PVA was used as emulsifier, the more transparent was the dispersion. After the addition of SDS, the appearance did not change. The z-average and PDI values were 75 - 100 nm or 0.10 - 0.20, respectively, and depended on two parameters. First, the more PVA was used, the smaller were the particles. Second, with addition of SDS the z-average and PDI values increased. This effect on the particle size was less pronounced when more PVA was used in the original dispersion.
During cooling the sample in the DSC, the crystallization temperature increased with the addition of SDS from approx. 25 to 28 °C for tripalmitin

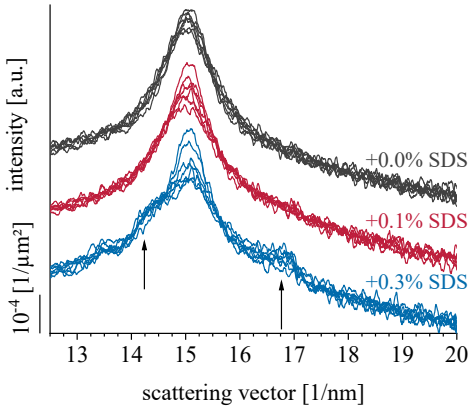

Figure 1: Wide angle X-ray diffractograms of tripalmitin nanoparticles. The composition of the dispersions was 5 % tripalmitin, 5 % Kuraray Poval 3-83 and 0, 0.1 or 0.3 % SDS, respectively. The diffractograms were recorded after 0, 1, 4, 7, 14, 21 and 28 d of storage at 20 °C.

nanoparticles, which were stabilized with 5 % PVA. Comparable to the effect on the particle size, the influence on the crystallization temperature also decreased with increasing total PVA concentration in the sample. In this case, the crystallization temperature was nearly constant at 22 °C for dispersions, which were stabilized with a total PVA-concentration of 15 %.
After crystallization, all particles were present in the metastable α-modification, which was confirmed with DSC and X-ray measurements. According to the SAXS patterns, the triglyceride in the lipid particles was arranged with a reduced lamellarity. The SAXS signals increased over the storage time for all samples. The 0.3 % SDS-containing sample displayed additional signals in the wide-angle scattering pattern at approx. 14.2 and 16.8 nm^{-1} (fig. 1). During the observed period of storage, the matrix lipid underwent time-dependent polymorphic transitions into more stable modifications. This could be confirmed with DSC measurements, which showed an increased size of the melting event at higher temperatures after 28 d of storage.
In contrast, there were no indications for the presence of particles in the β'-modification in the wide-angle range of the sample without SDS (fig. 1). These effects were also observed for the dispersions stabilized with higher concentrations of PVA or only 0.1 % additional SDS.

DISCUSSION

The addition of SDS to tripalmitin nanodispersions stabilized with partially hydrolyzed PVA had an

https://doi.org/10.24355/dbbs.084-202110251021-0

influence on their physicochemical behavior. It is known that PVA has a strong stabilizing effect on metastable polymorphic modifications in triglyceride nanoparticles [Rosenblatt et al., 2008]. The assumption in the present study was that the stronger the interaction between PVA and the matrix lipid, the lower is the crystallization temperature and the higher the stability of the metastable α-modification. The increase of the crystallization temperature with increasing SDS concentration might be an indication that the interaction between the matrix lipid and PVA is weakened in comparison to the reference dispersion without SDS.

Another indication for the reduction of the interaction between the matrix lipid and the main emulsifier, PVA, is the more pronounced polymorphic transition into more stable modifications. The particles with SDS addition transformed more rapidly into the β'-modification, which could be detected in the WAXS-pattern in fig. 1 [Chapman, 1962].

A possible cause of the observed phenomena might be an interaction between PVA and the additional SDS, which might influence the stabilization properties of PVA. It is supposed that SDS associates with PVA thus leading to a stretching of the polymer [Ramirez, 2020]. This could cause a more hydrophilic character of PVA. Consequently, the interaction between PVA and the matrix lipid would be reduced, which is reflected in the increasing crystallization temperature of the triglyceride nanoparticles.

The higher the PVA concentration, the lower is the effect of SDS addition on the observed effects on the crystallization temperature as well as on the particle sizes and the polymorphic behavior of the solid triglyceride nanoparticles.

This concentration dependent effect could be due to the relatively low SDS concentration in comparison to the high PVA concentration. Possibly, the SDS concentration is not high enough to exhibit a major effect on the high number of PVA molecules, which are located at the particle surface, or is preferably associated with free PVA molecules, which are assumed to be present in the aqueous phase.

There were no clear indications that SDS acts as main stabilizer by adding it after homogenization. A particularly prominent indication that PVA was still the main stabilizer is the less ordered structure of the particles after crystallization, which was not observed for SDS-stabilized triglyceride particles [Bunjes et al., 2002].

CONCLUSIONS

This study indicated that PVA-stabilized solid tripalmitin nanoparticles can undergo polymorphic transitions into more stable modifications more easily after the addition of SDS. This knowledge is important for the estimation of the stability of the product as potential drug delivery system. Furthermore, the addition of SDS might contribute to a better understanding of how PVA physically stabilizes the triglyceride nanoparticles and induces such a high stability of the metastable α-polymorph.

ACKNOWLEDGMENT

The ministry of Science and Culture (MWK) of Lower Saxony, Germany, is acknowledged for financial support within the Smart BioTecs alliance.

REFERENCES

Bunjes, H. (2010): Lipid nanoparticles for the drug delivery of poorly water-soluble drugs. In: Eur. J. Pharm. Pharmacol. 11, 1637-1645. DOI: 10.1111/j.2042-7158.2010.01024.x.

Bunjes, H.; Koch, M.H.J.; Westesen, K. (2002): Effects of surfactants on the crystallization and polymorphism of lipid nanoparticles. In: Colloid Polym. Sci. 121, 7-10. DOI: 10.1007/3-540-47822-1_2.

Chapman, D. (1962): The polymorphism of glycerides. In: Chem. Rev. 5, 433-456. DOI: 10.1021/cr60219a003.

Ramirez, J.C.; Flores-Villasenor, S.E.; Vargas-Reyes, E.; Herrera-Ordonez, J.; Torres-Rincon, S.; Peralta-Rodriguez, R.D. (2020): Preparation of PDLLA and PLGA nanoparticles stabilized with PVA and a PVA-SDS mixture: Studies on particle size, degradation and drug release. In: J. Drug Deliv. Sci. Technol. 60, 101907. DOI: 10.1016//j.jddst.2020.101907.

Rosenblatt, K.; Bunjes, H. (2008): Poly(vinyl alcohol) as emulsifier stabilizes solid triglyceride drug carrier nanoparticles in the α-modification. In: Mol. Pharm. 6, 105-120. DOI: 10.1021/mp8000759.

Speiser, P. (1986): Lipidnanopellets als Trägersystem für Arzneimittel zur peroralen Anwendung. In: EP 0167825 A2.

https://doi.org/10.24355/dbbs.084-202110251021-0

CONVENTIONAL AND FLOW SYNTHESIS OF ANTIBIOTIC CARBENE SILVER DERIVATIVES

Marcus Baumann, Cillian O'Beirne, Zoe Beato and Matthias Tacke

School of Chemistry, University College Dublin, Belfield, Dublin 4, Ireland;
marcus.baumann@ucd.ie or matthias.tacke@ucd.ie

ABSTRACT

Antibiotic resistance is undermining public health; it is imperative that new classes of antibiotics are discovered and developed by companies and academic institutions alike. Previous research by this group used the excellent adaptability of *N*-heterocyclic carbene (NHC)-silver compounds, which allowed for the discovery of the lead compound 1,3-dibenzyl-4,5-diphenylimidazol-2-ylidene silver(I) acetate (SBC3) [1]. SBC3 breaks the methicillin-resistance in *Staphylococcus aureus* (MRSA) [2] and has proven effective in *in vivo* tests using *Galleria mellonella* [3]. More recently, encouraging parts of the antibiotic mechanism of SBC3 were discovered, which underlines the ability of SBC3 to break antibiotic resistance patterns [4]. And SBC3 was tested successfully against biofilms *in vitro* and against MRSA in-infected mice *in vivo* [5]. In addition, a telescoped continuous flow route was developed which surpassed the previous batch approach. This provided for a scalable means to afford the targets in higher yield.

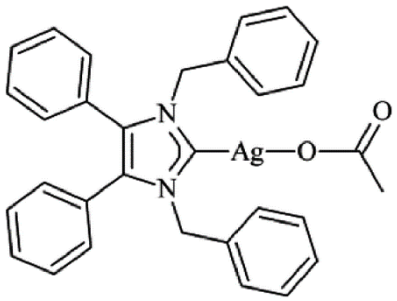

STRUCTURE OF THE ANTIBIOTIC DRUG CANDIDATE SBC3

REFERENCES

[1] Novel Benzyl-Substituted N-Heterocyclic Carbene–Silver Acetate Complexes: Synthesis, Cytotoxicity and Antibacterial Studies, S. Patil, A. Deally, B. Gleeson, H. Müller-Bunz, F. Paradisi, M. Tacke, Metallomics, **2011**, 3, 74 - 88. doi:10.1039/C0MT00034E

[2] Investigations into the Antibacterial Activity of the Silver-Based Antibiotic Drug Candidate SBC3, M. A. Sharkey, J. P. O'Gara, S. V. Gordon, F. Hackenberg, C. Healy, F. Paradisi, S. Patil, B. Schaible, M. Tacke, Antibiotics, **2012**, 1, 25 - 28. doi:10.3390/antibiotics1010025

[3] Assessment of Antimicrobial Activity of the Carbene Silver(I) Acetate Derivative SBC3 using Galleria Mellonella Larvae, N. Browne, F. Hackenberg, W. Streciwilk, M. Tacke, K. Kavanagh, Biometals, **2014**, 27, 745 - 752. doi:10.1007/s10534-014-9766-z

[4] The antibacterial drug candidate SBC3 is a potent inhibitor of bacterial Thioredoxin Reductase, J. O'Loughlin, S. Napolitano, F. Alkhathami, C. O'Beirne, D. Marhöfer, M. Tacke, M. Rubini, ChemBioChem., **2021**, 22, 1093 - 1098. doi:10.1002/cbic.202000707

[5] Continuous Flow Synthesis and Antimicrobial Evaluation of NHC* Silver Carboxylate Derivatives of SBC3 in vitro and in vivo, C. O'Beirne, M. E. Piatek, J. Fossen, H. Müller-Bunz, D. A. Andes, K. Kavanagh, S. A. Patil, M. Baumann, M. Tacke, Metallomics, **2021**, 13, mfaa011. doi: 10.1093/mtomcs/mfaa011

https://doi.org/10.24355/dbbs.084-202110251021-0

NUCLEATION AND CRYSTAL GROWTH OF ALPHA-GLYCINE

Andrew Cashmore[1,2], Mark Haw[1], Mei Lee[3], Jan Sefcik[1,2]

1. Department of Chemical and Process Engineering, University of Strathclyde, Glasgow, UK
2. CMAC Future Manufacturing Research Hub, University of Strathclyde, Glasgow, UK
3. GlaxoSmithKline, Stevenage, UK

ABSTRACT

Secondary nucleation is widely present in crystallisation processes and it is often relied upon to attain desirable critical quality attributes of crystalline products, such as polymorphic form and crystal size distribution. This is particularly the case in continuous crystallisation, where a good control of secondary nucleation can be crucial in order to achieve and maintain steady state operation.

This work utilises rapid, small-scale experiments in agitated vials with in-situ imaging for crystal counting and sizing (using the Crystalline platform), to quantify nucleation and crystal growth kinetics of α-glycine across a range of supersaturations in aqueous solutions under isothermal conditions. Both seeded and unseeded crystallisation experiments were conducted.

It was found that secondary nucleation and crystal growth rates determined from the same vials show a close correlation across the whole range of supersaturations investigated, which suggest a close relationship between the mechanisms of shear induced secondary nucleation and crystal growth in this system.

Keywords: Crystallisation, Nucleation, Crystal Growth

INTRODUCTION

Crystallisation from solution is a purification process used throughout the pharmaceutical and chemical industries to achieve desired crystalline particulate product properties, such as solid form, particle size, shape and purity. Control over these particulate properties facilitates downstream processing and resulting product performance. To achieve control of such a crystallisation process, an understanding of nucleation and growth, the two fundamental stages of crystal formation, is required.

In order to avoid problems associated with the intrinsic stochasticity of primary nucleation, secondary nucleation, the generation of new crystal nuclei from already-existing crystals, is often employed in industrial crystallisation. Secondary nucleation is often initiated at relatively low supersaturations to provide a controlled, steady supply of new crystals, accompanied by relatively slow crystal growth to achieve good purification and consistent process performance. This study aims to improve fundamental understanding of the relationships between crystal growth, nucleation and supersaturation in the metastable zone for crystallisation of α-glycine from aqueous solutions.

RESULTS AND DISCUSSION

Crystal growth rates for α-glycine estimated from in-situ imaging were in good agreement with values reported in literature from single crystal growth experiments. Plotting growth rates on a linear scale appears to indicate the presence of a ‘dead zone’ below a certain supersaturation, where growth does not seem to take place. However, if data is plotted on a log-log scale, they show a clear power law dependence on supersaturation, as may be expected from crystal growth theories. Therefore, there does not appear to be any dead zone for crystal growth of α-glycine.

Secondary nucleation rates [B] for both seeded and unseeded experiments were also estimated from in-situ imaging. The seed crystals were prepared and added to vials following a previously outlined workflow[1]. When the secondary nucleation rates were shown on a linear scale, data seem to indicate a secondary nucleation

https://doi.org/10.24355/dbbs.084-202110251021-0

threshold around S=1.1. Again, when data is shown on a log-log scale, they are consistent with a power law dependence on supersaturation. Although it cannot be ruled out that secondary nucleation completely ceases at some lower supersaturations, it can become too slow to measure with a given experimental technique at some point, and it can also become insignificant in a practical industrial crystallisation context. Furthermore, secondary nucleation rates in seeded and unseeded experiments were very similar (Figure 1), which is consistent with the concept of the 'single nucleus mechanism'[2]: in other words even in unseeded conditions, crystallisation proceeds through the formation of a single crystal seed from solution by primary nucleation, with further nuclei then appearing through secondary nucleation from this original seed crystal.

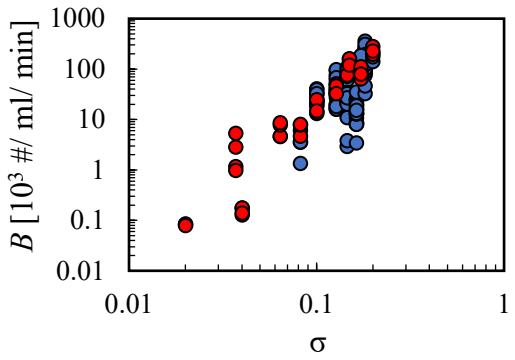

Figure 1. Comparison of secondary nucleation rates in seeded (red circles) and unseeded (blue circles) conditions plotted vs σ = S-1.

The primary nucleation rates were then estimated from induction time probability distributions[3] and plotted, along with secondary nucleation against the corresponding growth rates (Figure 2). The primary nucleation rate is much lower than secondary nucleation at all supersaturations suggesting that a high supersaturation is required to induce nucleation. Therefore, in a continuous crystallisation process, secondary nucleation is required to ensure that there is a constant supply of new crystals to achieve steady state operation.

Crystal growth and secondary nucleation are often studied and presented as two conceptually separate processes or mechanisms. Our approach allows us to compare the growth rate and the corresponding secondary nucleation rate from the same experimental vials, based on the same imaging-based measurement and image analysis. We see that there is a close relationship between growth and secondary nucleation kinetics across a wide range of supersaturations. This suggests a possible mechanistic relationship between the two phenomena, where the secondary nucleation induced by fluid shear is related to growth of the crystal boundary layer in contact with the supersaturated solution, where loosely bound crystalline domains are swept from the boundary layer and serve as crystal nuclei. This effect would be clearly distinct from mechanical breakage or attrition of seed crystals, as there is no reason why such a mechanical process would be related to the crystal growth rate and indeed solution supersaturation.

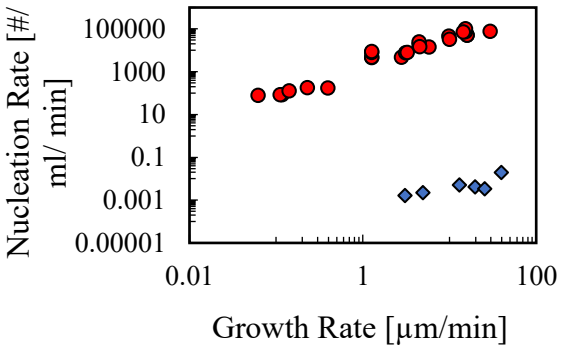

Figure 2. Primary (blue diamonds) and secondary (red circles) nucleation rates plotted vs corresponding growth rate. Secondary nucleation rate is many orders of magnitude faster than primary nucleation at all supersaturations.

CONCLUSIONS

Using a rapid small scale experimental technique utilising image analysis to quantify nucleation and growth kinetics, the metastable zone, primary and secondary nucleation kinetics and growth rates of α-glycine has been investigated. Results show that there is neither crystal growth dead zone nor secondary nucleation threshold present in this system. It is also shown that there is a close relationship between the secondary nucleation and the crystal growth rate across all supersaturations investigated. This work will provide better understanding of crystal nucleation and growth mechanisms while using rapid, small scale experiments and data analysis illustrated here should enable more facile crystallisation process development.

REFERENCES

(1) Briuglia, M.; Sefcik, J.; Ter Horst, J. H. Measuring Secondary Nucleation through Single Crystal Seeding. *Cryst. growth Des.* **2019**.

https://doi.org/10.24355/dbbs.084-202110251021-0

(2) Kadam, S. S.; Kramer, H. J. M.; Ter Horst, J. H. Combination of a Single Primary Nucleation Event and Secondary Nucleation in Crystallization Processes. *Cryst. Growth Des.* **2011**.

(3) Jiang, S.; Ter Horst, J.H. Crystal Nucleation Rates from Probability Distributions of Induction Times. *Cryst. Growth Des.* **2011**.

https://doi.org/10.24355/dbbs.084-202110251021-0

DIGITAL HEALTH - DIGITAL 2D/3D PRINTING OF PERSONALIZED MEDICATION

M. Dachtler[1], K. Eggenreich[2], T. Pflieger[3]

[1] DiHeSys Digital Health Systems GmbH; Schwäbisch Gmünd / Germany; markus.dachtler@dihesys.com
[2] Gen-Plus GmbH & Co. KG; München / Germany
[3] DiHeSys Digital Health Systems GmbH; Schwäbisch Gmünd / Germany

ABSTRACT

Without any doubt the young technology of additive manufacturing, including 2D and 3D printing, has been changing the world. A wide spectrum of objects in medical and pharmaceutical field can already be successfully printed. This ranges from a detailed figure in the micrometer regime to a full size residential house unit made from concrete [Sakin et al., 2017; Doherty et al., 2020]. In the pharmaceutical sector, additive manufacturing offers the option of medication customization [Pravin et al., 2018]. Integrating this new technology has several advantages over the current, well-established but outdated "one-size-fits-all" approach. Besides avoiding medication errors, printing tailored oral dosage forms is financially attractive for small scale on-demand production [Awad et al., 2018]. The development of dosage forms, production of sample batches and modification of samples can be done with little effort compared to generic powder-pressed pills which require heavy pharmaceutical machinery [Awad et al., 2018; Dachtler et al., 2020]. To further progress and to create the legal framework for the approval of additively manufactured drugs it requires a paradigm change of stakeholders who have the power to make decisions and changes [Horst et al., 2019].

Keywords: Healthcare Digitalization, Pharmaceutical Industry, Additive Manufacturing, 2D/3D Printing.

BENEFITS OF PERSONALIZED MEDICATION

Currently, the majority of pharmaceutical formulations have a predetermined dosage of one or more active ingredients [Rahman et al., 2018]. This is not tailored to the physiological constitution of the patient. Dosing drugs optimally depends on genetic, metabolic and gender-specific properties. Highly potent drugs in particular have a narrow therapeutic window, which varies from patient to patient. This calls for an individual treatment through personalized healthcare. Generic drugs do not meet the requirements for treating patients immaculately and there is a possibility of non-optimal or incorrect dosing [Reiner et al., 2020]. A wide variety of dosage forms and combinations of active pharmaceutical ingredients with tailored release kinetics need to be administered. This way, optimal therapy success is guaranteed and the risk of perilous medication errors is minimized. The problem of wrong medication should not be underestimated, as it is the third leading cause of death in the USA after cardiovascular diseases and cancer [Makary et al., 2016].

The decentralized production of drugs avoids complex process steps involved in the "classic" production of solid dosage forms. The idea includes patient data being transmitted in digital form, for example from the attending physician, directly to the 2D/3D printer in a pharmacy. The diagnosis is linked directly to individual medication. Small batches are produced cost-efficiently as required, which prevents drug bottlenecks or waste of active ingredients [Fasila et al., 2008]. Stocks of rare drugs can be preserved this way.

Classic powder-pressed tablets are still the first choice for the mass market, as they can be produced time- and cost-efficiently in large quantities. However, individual therapy is not possible this way. Conventional solid dosage forms are complex systems made up of a wide variety of active ingredients and excipients [Qiu et al., 2016]. The development of a conventional formulation is therefore associated with a high level of effort due to possible cross-side effects.

For new drug development, a large number of animal and clinical studies are necessary before a suitable carrier system, a generic combination of active ingredients and a suitable release profile can be found. This is where pharmaceutical 2D/3D printing has a decisive economic advantage. Dosage forms

https://doi.org/10.24355/dbbs.084-202110251021-0

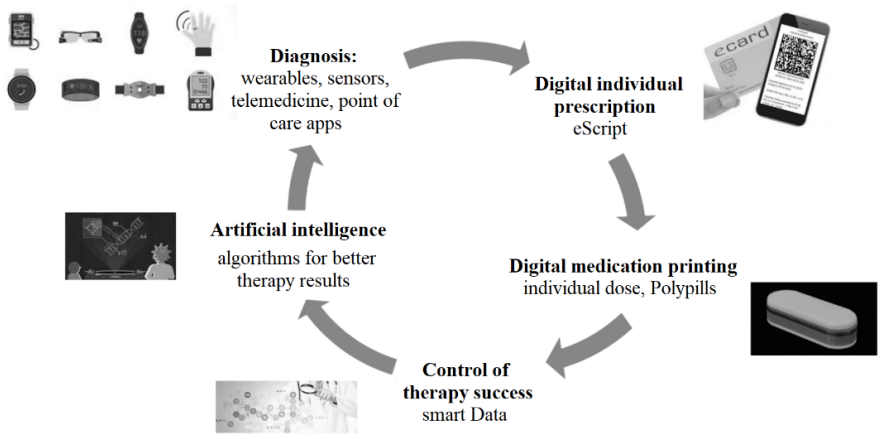

Figure 1: *The future of digital healthcare as a disruptive system including multiple steps to obtain optimal treatment individually tailored to the patient.*

would be developed, produced and modified at a minimum of cost and time.

INDIVIDUALIZED CARE – A DISRUPTIVE SYSTEM

In order to digitize the healthcare system as a whole, several separate players and stakeholders must be successfully linked. As part of a large multi-part disruptive system, the digital medication printing makes a decisive contribution to the personalization of medicine. Further important segments of the system as a whole include the use of artificial intelligence for data analysis, innovative methods for creating diagnoses and monitoring the success of therapy using smart data [Nohl-Deryk et al., 2018]. In a digitized healthcare system, active pharmaceutical ingredient systems are provided by supply companies for pharmacies, which manufacture tailored dosage forms on demand in small scales. While the doctor uses digitally obtained data to make an algorithm-based precision diagnosis for the patient, the data is forwarded directly to the formulator device in a pharmacy (see Figure 1). The reimbursement and big data collection for future optimization of diagnoses is carried out by the health insurance company [Baierlein, 2017]. Big data describes data sets that are, among other things, too large, complex, dynamic or loosely structured to be evaluated using conventional data processing methods and require innovative solutions therefore.

THE FUTURE OF HEALTH CARE

Medicine is a vivid science that lives from the introduction of innovations and new approaches and is therefore constantly developing. In the past, data acquisition in medicine was symptom-based and physicians depended their treatment on intuition. Today's diagnoses are made on the basis of patterns which results in actions based on evidence. Future application of rules, algorithms and big reference databases not only enable actionable clinical decision support but also individually efficient care [Wilckens, 2014]. Algorithms are going to convert personally generated data sets to precision treatment. Various studies indicate that integrating technology and digitalization have a positive impact on treatment success [Frias, 2017]. Wearable sensors and mobile gadgets already have been shown to increase therapeutic adherence in some cases. Nevertheless, there is still a long way to complete digitization of the health system [Kvedar et al., 2014].

https://doi.org/10.24355/dbbs.084-202110251021-0

REFERENCES

Awad, A.; Trenfield, S.; Goyanes, A.; Gaisford, S.; Basit, A. (2018): Reshaping drug development using 3D printing. In: Drug discovery today 23(8): S. 1547-1555.

Baierlein, J. (2017): Grad der Digitalisierung im Gesundheitswesen im Branchenvergleich: Hinderungsgründe und Chancen. In: Digitale Transformation von Dienstleistungen im Gesundheitswesen II, Springer: S. 1-11.

Dachtler, M.; Huber G.; Pries T. (2020): 2D & 3D-Print-Technologien in der pharmazeutischen Industrie. In: Digitale Transformation von Dienstleistungen im Gesundheitswesen VII, Springer: S. 53-66.

Doherty, R.; Varkevisser, T.; Teunisse, J.; Hoecht, J.; Ketzetzi, S.; Ouhajji, S.; Kraft, D. (2020): Catalytically propelled 3D printed colloidal microswimmers. In: Soft Matter 16(46): S. 10463-10469.

Fasola, G.; Aita, M.; Marini, L.; Follador, A.; Tosolini, M.; Mattioni, L.; Mansutti, M.; Piga, A.; Brusaferro, S.; Aprile, G. (2008): Drug waste minimisation and cost-containment in medical oncology: two-year results of a feasibility study. In: BMC Health Services Research 8(1): S. 1-8.

Frias, J.; Virdi, N.; Raja, P.; Kim, Y.; Savage, G.; Osterberg, L. (2017): Effectiveness of digital medicines to improve clinical outcomes in patients with uncontrolled hypertension and type 2 diabetes: prospective, open-label, cluster-randomized pilot clinical trial. In: Journal of medical Internet research 19(7): S. e246.

Horst, A.; McDonald, F.; Hutmacher, D. (2019): A clarion call for understanding regulatory processes for additive manufacturing in the health sector. In: Expert review of medical devices 16(5): S. 405-412.

Kvedar, J.; Coye, M.; Everett, W. (2014): Connected health: a review of technologies and strategies to improve patient care with telemedicine and telehealth. In: Health affairs 33(2): S. 194-199.

Makary, M.; Daniel, M. (2016): Medical error - the third leading cause of death in the US. In: BMJ, The British Medical Journal 353.

Nohl-Deryk, P.; Brinkmann, J.; Gerlach, F.; Schreyögg, J.; Achelrod, J. (2018): Hürden bei der Digitalisierung der Medizin in Deutschland - eine Expertenbefragung. In: Das Gesundheitswesen 80(11): S. 939-945.

Pravin, S.; Sudhir, A. (2018): Integration of 3D printing with dosage forms: A new perspective for modern healthcare. In: Biomedicine & Pharmacotherapy 107: S. 146-154.

Qiu, Y.; Chen, Y; Zhang, G.; Yu, L.; Mantri, R. (2016): Developing solid oral dosage forms: pharmaceutical theory and practice. In: Academic press.

Rahman, Z.; Ali, S.; Ozkan, T.; Charoo, N.; Reddy, I.; Khan, M. (2018): Additive manufacturing with 3D printing: Progress from bench to bedside. In: The AAPS journal 20(6): S. 1-14.

Reiner, G.; Pierce, S.; Flynn, J. (2020): Wrong drug and wrong dose dispensing errors identified in pharmacist professional liability claims. In: Journal of the American Pharmacists Association 60(5): S. e50-e56.

Sakin, M.; Kiroglu, Y. (2017): 3D Printing of Buildings: Construction of the Sustainable Houses of the Future by BIM. In: Energy Procedia 134: S. 702-711.

Wilckens, T. (2014): Pattern diagnostics and precision medicine. In: Precision Medicine World Economic Forum 2013.

https://doi.org/10.24355/dbbs.084-202110251021-0

CORONAVIRUS VACCINES – A BLUEPRINT FOR OTHER VACCINE DEVELOPMENTS?

Julia Bialek-Waldmann1, Leander Grode[1],

[1] Vakzine Projekt Management GmbH; Mellendorfer Strasse 9; 30625 Hannover; Germany;
grode@vakzine-manager.de

ABSTRACT

In December 2019, a series of pneumonia of unknown cause emerged in Wuhan, China, which developed into a global pandemic with more than 200 million cases and 4 million deaths worldwide as of August 2021. The enveloped RNA betacoronavirus which was found to cause the pandemic was named severe acute respiratory syndrome coronavirus-2 (SARS-CoV-2). Academia and industry started with non-clinical and clinical development of several SARS-CoV-2 vaccine candidates immediately and results were achieved enormously fast. As an example, BioNTech and Pfizer got their joint SARS-CoV-2 vaccine approved less than eight months after trials started, while under normal circumstances vaccine development takes up to 10 – 15 years. In the case of the SARS-CoV-2 vaccine the extremely fast turnaround time from start of clinical trials to approval of the first vaccine candidates was driven by the urgent medical need and made possible by the mobilisation of enormous financial resources from the private and public sectors, as well as manpower and effort and the willingness of regulators to speed up timelines and approval processes.

Looking at the extremely fast and successful development of several SARS-CoV-2 vaccine candidates, it is difficult to understand from a layman's perspective why for others diseases like Human Immunodeficiency Virus/ Acquired Immunodeficiency Syndrome (HIV/AIDS) and tuberculosis (TB), which are among the top ten causes of death worldwide, development of effective vaccines takes so long. More than 30 years after HIV has been discovered, there is still no vaccine available for prevention of HIV infection. Development of several vaccine candidates has failed in clinical trials. The difficulties stem in large part from HIV's unusual characteristics of replicating and mutating rapidly and high sequence diversity, its ability of immune system evasion and the creation of a persistent viral reservoir within the host. Development of the novel TB vaccine candidate VPM1002, which is designed to be a safe and effective vaccine for prevention of TB infection and TB recurrence, is an example of classical vaccine development. VPM1002 was invented in Germany, went through successful non-clinical development and is currently being tested in phase III clinical trial.

The achievements during the last year fast development of SARS-CoV-2 vaccines during the last year have proven that in case of a pandemic situation and an urgent medical need, fast vaccine development is possible. The achievements were reached with high financial commitment and regulators have shown willingness and engagement to accelerate timelines for review and approval processes. It would be desirable if further vaccine developments could benefit from these efforts.

Keywords: SARS-CoV-2, COVID-19, vaccine development

https://doi.org/10.24355/dbbs.084-202110251021-0

MULTI-STAGE LIQUID/LIQUID EXTRACTION WITH A ZAIPUT APPARATUS

C. Heiduk[1,2], I. Hohlen[1,2], S. Scholl[1,2*]

[1]TU Braunschweig, Institute for Chemical and Thermal Process Engineering, Langer Kamp 7, 38106 Braunschweig, Germany (*Corresponding author: s.scholl@tu-braunschweig.de)

[2]TU Braunschweig, Center for Pharmaceutical Engineering, Franz-Liszt-Str. 35a, 38106 Braunschweig, Germany

ABSTRACT

Poorly separable liquid/liquid mixtures often pose a major challenge in pharmaceutical extraction. In particular, compounds containing a low difference of density are difficult to separate using mixer-settler setups. The Zaiput device can prove an advantage over present liquid/liquid extractors. The research work involves characterizing the Zaiput apparatus for liquid/liquid extraction of pharmaceutical compounds with the model solvent system toluene-water. The extraction efficiency was investigated for a solvent mixture containing toluene-acetone-water residence times. To evaluate the separation success, the outlet's concentrations are measured via IR spectroscopy.

Keywords: multi-stage liquid/liquid extraction, countercurrent liquid/liquid extraction, continuous extraction, membrane separation

INTRODUCTION

Liquid/liquid extraction (LLE) represents an important processing step in the pharmaceutical industry and becomes more popular among the separation techniques. Compared to distillative separation, LLE provides reduced energy consumption and additionally, there is the opportunity to process thermosensitive compounds due to the low operating temperature. In practice, multi-stage processing is often carried out to achieve efficient separation and increase the recovery of a product. This approach is required when a small partition coefficient impedes the separation.

The Zaiput (Figure 1) represents a new device in which multi-stage countercurrent liquid-liquid extraction (MCCE) can be realized continuously even on a laboratory scale. Improved extraction rates result from higher mass transfer coefficients at the micro and milli scales. The high mass transfer rates in the slug flow led to equilibrium at each stage prior to the separation unit.

However, the separation of the phases is challenging since the surface forces dominate over the traditionally used gravity force. Membrane separation is based on the utilization of surface forces and suitable for realizing phase separation. This type of separation is used in the zaiput.

Advantages of the Zaiput compared to conventional LLE apparatus include: continuous operation, separation of liquids with the same density or emulsions, the plug-and-play functionality, as well as the easy and direct possibility to scale-up due to a modular design.

Figure 1: Zaiput multi-stage extraction platform [Weeranoppanant, 2020]

MCCE can be divided into two types based on the arrangement of the contacting units: differential and discrete arrangement (Figure 2). Differential contacting includes multiple stages operating continuously in a single device with no separator between the stages. On the contrary, discrete MCCE requires phase separation prior to pumping to subsequent stages. As in the Zaiput extraction and separation operate independently, this setup is scalable to a large number of stages.

LLE in industrial applications is usually arranged by countercurrent flow design (CC-LLE), which offers the

https://doi.org/10.24355/dbbs.084-202110251021-0

lowest consumption of extractant. With this approach, the aqueous raffinate is supplied from one stage to an earlier stage as feed, while the organic phase is conveyed in the reverse flow direction. Therefore, the overall system can achieve high recovery even if the recovery of the product in each stage is low. In multi-stage extraction, selectivity and process yield are accordingly decoupled, since yield depends on the number of extraction stages used.

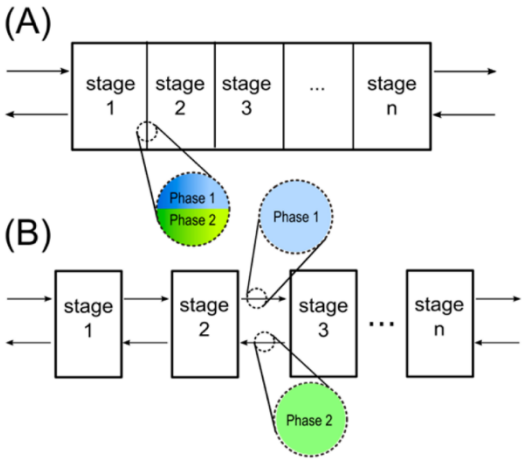

Figure 2: Two categories of MCCE's contacting unit arrangement: (A) differential and (B) discrete [Weeranoppanant, 2017].

Figure 3 displays the experimental set-up. Multi-channel peristaltic pumps convey the liquids from one stage to the next. Mass transfer is realized by droplet formation in capillaries by segmented flow mixing. In order to achieve equilibrium after each stage, a phase separation via membrane follows subsequently. A membrane acts as a barrier for the two immiscible phases. Preferably, the membrane is wetted by one of the phases whereas the other remains non-wetting. Moreover, each separator incorporates a self-tuning pressure regulating element which allows fluctuations caused by inaccurate pumping still allow robust operation (Figure 4). In case of a hydrophobic membrane, the organic (wetting phase; green) flows through the membrane, while the aqueous (non-wetting phase; blue) retains it.

Equilibrium stage is obtained when the mass transfer in the mixing tube is sufficiently long and the separator operates effectively.

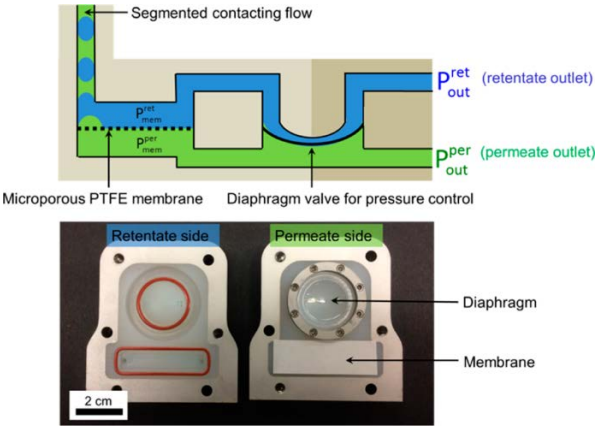

Figure 4: Schematic and photographic illustration of the membrane-based separator with self-tuning element (heavy curved line) providing a constant pressure difference across the membrane (vertical lines). The aqueous and organic liquids are shown in green and blue [Adamo, 2013; Weeranoppanant, 2017].

CHARACTIZATION OF THE DEVICE

In this study, the applicability of the Zaiput device for the liquid/liquid extraction of pharmaceutically relevant compounds is investigated. In the first step, a model compound system (toluene-water) without a transition component is considered and investigated with regard to the separation performance of the membrane.

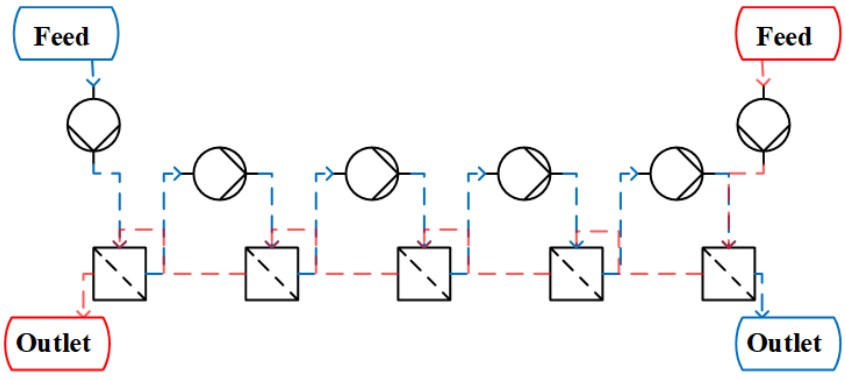

Figure 3: Flow diagram of countercurrent extraction process; aqueous phase in blue; organic phase in red

https://doi.org/10.24355/dbbs.084-202110251021-0

For this purpose, the residence time was varied over the volumetric flow rates of the organic and aqueous feed streams at a constant number of stages $N = 2$. The experimental matrix is shown in the Table 1.

Table 1: Variation of the volumetric flow rates of the experiments.

Q_{org}, mL/min	Q_{aq}, mL/min
1	2
2	1
2	2
3	1
2.5	1

In the preliminary tests without transition component, no influence could be detected when varying the volume flow. In all experiments, perfect separation occured so that retentate and permeate can already be obtained pure after the first residence time.

EXTRACTION EFFICIENCY

The obtained findings are applied to a classical ternary system to test the extraction efficiency. Water as the extraction solvent was used to extract acetone from toluene feed solvent. A high percentage of acetone was added to evaluate the system's ability to manage variations in flow rates across different stages. In addition, acetone significantly reduces the interfacial tension making it a challenging case study.

Analogous to the experiments without transition component, different residence times were set (Table 1). The organic phase constituted a mixture of toluene and acetone in a ratio of 1:1. In all experiments, a sample was taken after 1, 3 and 5 residence times. The duration of the sampling is set in each case equal to the duration of one residence time. Characteristic parameters for the extraction process, such as the minimum residence time, the depletion of the transition component as a function of the throughput, and the stage efficiency are determined.

The separation performance drops significantly during experiments with acetone. The permeate sample contain more than 20% acetone, whereas it should actually consist only of toluene. However, there is a trend toward worse separation performance in the experiments with a volumetric flow rate of 2.5 mL/min and above.

MEMBRANE SELECTION

The influence of the membrane is particularly noticeable, as the best results were obtained after the membrane was replaced. During the experiment, a deterioration of the separation performance is already evident, so that the amount of acetone in the organic phase increases over the course of the experiment. Since the duplicate determination of the tests was always carried out exactly one after the other, a similar course should have been shown if the membrane had not deteriorated. However, this conclusion does not occur, leading to the assumption that the membrane loses its filtering effect in the presence of toluene. Furthermore, the poor separation performance indicates that the membrane is not suitable for toluene. The influence of the mixing ratio of acetone and toluene is to be checked further, since different results can be expected with a lower proportion of acetone.

ANALYTICS

Furthermore, analytics are developed to evaluate the extraction success by determining the percent extraction and efficiency. The outlet concentration of each component was analyzed by IR spectroscopy. For calibration, signals with the highest intensity are used which are 1222.95 cm^{-1} for acetone, 733.54 cm^{-1} for toluene and 3551.12 cm^{-1} for water.

The three substances exhibit a miscibility gap, resulting in the formation of a two-phase system at certain mixing ratios which prevents the homogeneity of the sample. Thus, it is impossible to describe exactly the mixing ratio of the sample by means of a partial quantity of the sample. By adding a diluent, a homogeneous system is obtained but the detection capability decreases due to the dilution. The system also proves to be significantly more complex in terms of analysis.

A further challenge constitutes the high volatility of acetone (306 hPa at 25°C), which leads to falsified sample compositions. To counteract volatilization, the samples must be measured immediately or stored refrigerated.

Additionally, water has a high absorption coefficient compared to acetone and toluene. This leads to a

https://doi.org/10.24355/dbbs.084-202110251021-0

homogeneous broadening at certain intensities, since the linearity of the Lambert Beer law is limited by the Einstein coefficients and therefore, not all molecules can be energized. The high rate constant of autoproteolysis of water also proves troublesome. As a result, the natural linewidth is greatly widened and consequently, other signals are overlapped.

DISCUSSION

Operating limits can be caused by pressure difference either too large or too small (Figure 5). If the pressure difference across the membrane is large, the retained phase may break through. Possible reason for a high pressure difference can generate a low surface tension, which would require a replacement of the membrane. The flow rate also affects the internal pressure, so that a lower flow rate has to be set. Changing the solvent ratio could also led to better results.

If the pressure is unsuitably, the permeate phase is partially retained by the membrane and exits with the retentate phase. A possible solution could be to lower the flow rate of the permeating phase or changing the solvent ratio.

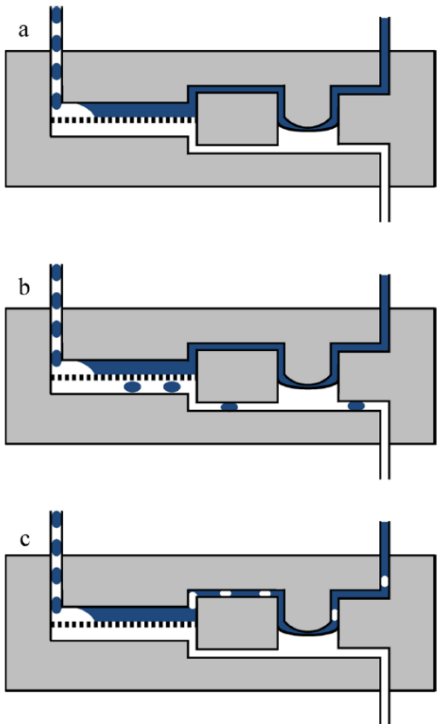

Figure 5: Schematic representation of the different modes of membrane-based separation: (a) under normal conditions; (b) breakthrough of the retained phase; (c) retention of the permeate phase [Adamo, 2013].

In the initial trials, only two-stage extractions were performed. For future work, higher numbers of stages will be investigated. Moreover, the statements obtained need to be reviewed by multiple determinations and transferred to other systems.

ACKNOWLEDGMENT

I gratefully acknowledge Friederike Stehmann for providing the Zaiput device. Furthermore, I thank Ilka Hohlen for experimental help and Tim Blinzer for IR spectroscopical analyses.

NOMENCLATURE

N	total number of stages in the setup
Q	volumetric flow rate, mL/min

SUBSCRIPT

aq	aqueous
org	organic

REFERENCES

Adamo, Andrea; Heider, Patrick L.; Weeranoppanant, Nopphon; Jensen, Klavs F. (2013): Membrane-Based, Liquid–Liquid Separator with Integrated Pressure Control. In: *Ind. Eng. Chem. Res.* 52 (31), S. 10802–10808. DOI: 10.1021/ie401180t.

Weeranoppanant, Nopphon; Adamo, Andrea (2020): In-Line Purification: A Key Component to Facilitate Drug Synthesis and Process Development in Medicinal Chemistry. In: *ACS medicinal chemistry letters* 11 (1), S. 9–15. DOI: 10.1021/acsmedchemlett.9b00491.

Weeranoppanant, Nopphon; Adamo, Andrea; Saparbaiuly, Galym; Rose, Eleanor; Fleury, Christian; Schenkel, Berthold; Jensen, Klavs F. (2017): Design of Multistage Counter-Current Liquid–Liquid Extraction for Small-Scale Applications. In: *Ind. Eng. Chem. Res.* 56 (14), S. 4095–4103. DOI: 10.1021/acs.iecr.7b00434.

https://doi.org/10.24355/dbbs.084-202110251021-0

THE ROTATING DISC REACTOR

MIXING CHARAKTERISTICS OF A NOVEL REACTOR CONCEPT

L. Jäger[1,2], N. Hofmann[1,2], S. Scholl[1,2*]

[1] Institute for Chemical and Thermal Process Engineering, TU Braunschweig,
Langer Kamp 7, 38106 Braunschweig, Germany; s.scholl@tu-bs.de (*Corresponding author)
[2] Center for Pharmaceutical Engineering, TU Braunschweig

ABSTRACT

Mixing is a crucial parameter for a wide range of processes in bio-/chemical engineering. In multiphase flows, the aim is a high and uniform mixing effect throughout the reaction volume without negative effects on the discrete phase. These are usually caused by the hydromechanical stress exerted by the mixing element. The present study introduces a novel reactor concept to overcome the use of fast rotating, locally acting mixing elements common in stirred tank reactors. Therefore, the reactor is designed of a flat, horizontally mounted cylinder, which enables mixing of the enclosed volume by its rotation around the central axis. To evaluate the mixing performance, a colorimetric method for mixing time determination is presented and the spatial evolution of mixing kinetics visualized. In addition, the method reveals the dependencies of the mixing time on the rotational speed and filling volume.

Keywords: Rotating Disc Reactor, rotating reactor, local mixing time, spatial mixing time distribution, flow visualization

INTRODUCTION

The mixing process plays a key role in reactors for process engineering, since it affects the process performance substantially. Various objectives can be encountered in heat transfer, chemical reactions, homogenization, generation of dispersions and suspensions, etc. with its individual process requirements. In general, not only a rapid mixing is aspired, but also a uniform distribution of the mixing effect over the entire filling volume without the formation of insufficiently mixed fractions.

For mixing tasks, one of the most frequently used reactors is the stirred tank reactor. Potentially adverse is the locality of the energy dissipation induced by the stirrer, which leads to a compartmentation [Fitschen, 2021] and highly inhomogeneous flow regimes over the filling volume [Machado, 2013]. Heterogeneities may imply undesirable process behavior, as mixing affects for example, primary nucleation in crystallization processes [Liu, 2015] or yield and by-product formation in cell cultivation [Bylund, 1998]. Additionally, the high speed of the rotating stirrer blades, to increase the mixing performance, determines the mechanical stress on suspended particles. This can detrimentally affect processes such as crystallization by attrition [Lakerveld, 2014] or biotechnological applications with shear-sensitive microorganisms [Jüsten, 1998].

To overcome the issues associated with the basic design of stirred tank reactors and to offer deep insights into the macroscopic mixing process, a method for local mixing time determination is presented and applied to the novel concept of the Rotating Disc Reactor (RDR).

ROTATING DISC REACTOR

As shown in Figure 1, the RDR essentially consists of a horizontally mounted, flat cylinder with partial filling. The cylinder exhibits an inner diameter of 225 mm and a width of 10 mm with a maximum filling volume of approx. 130 mL. The clamped hollow disc rotates around its central axis which realizes the mixing of the reaction volume. This way, the power input takes place via the large wetted surface and the RDR manages mixing without an intrusive mixing element. The intended benefit is twofold: the moving surface extends the mixing effect to the entire volume, as opposed to the local restriction of a stirrer. Furthermore, the absence of rapid rotating internals potentially reduces shear in multiphase flows despite high mixing performance, which will be shown in future work.

https://doi.org/10.24355/dbbs.084-202110251021-0

Figure 1: CAD drawing of the Rotating Disc Reactor

The reactor is entirely made of transparent acrylic glass and illuminated by a homogeneous LED background panel of 30000 lumens to apply the method for mixing time determination by means of computer vision described below.

MIXING TIME DETERMINATION

Indicator system

In order to display and examine the mixing process, a colorimetric method has been developed. Therefore, the volume is stained with two pH indicators according to the Dual Indicator System for Mixing Time [Melton, 2002]. While methyl red turns from red to yellow in the pH interval 4.2 - 6, thymol blue turns from yellow to blue in 8 - 9.6. A narrow range with yellow color around pH 7 results, so that deviations in both directions - acidic and basic - can be displayed. The application of sodium hydroxide to a previously acidified indicator solution causes a color change from red to finally yellow with temporary overshoot into the basic range. This allows observation and objective evaluation by computer vision, while the local overshoot, indicated by blue color, can be accurately accounted for. High local base concentrations are not interpreted as mixed, as may be the case with a single indicator only. The color change is captured with a system camera at 25 Hz in a resolution of 3840 x 2160 and roughly 1.2 x 10^6 pixels in the region of interest.

Analysis

The algorithm to process the captured videos is written entirely in the Python distribution Anaconda and is built mainly on the packages NumPy and OpenCV.

First, the spatial distortion of the camera is corrected by reference images of a dot pattern that ensures an accurate allocation of an identical volume fraction for each pixel. Without the correction, the distortion can lead to inaccuracies in the derivation of the mixing time caused by different volume per pixel representations, which cannot be properly considered in the subsequent calculations. For further information and the technical implementation, the reader is referred to the docs of OpenCV's camera calibration. In the second step, the projection area of the filling volume is selected automatically by the logical combination of multiple thresholds within the color channels of the RGB color space and the hue in HSV color space. To obtain a reliable detection method, the so found preselected areas are converted into contours by canny edge detection and sorted according to their area. The contour with the largest area represents the correct projection area and is converted to a boolean mask for further use in masked NumPy arrays. Hence, all mathematical operations are performed only within the mask.

To evaluate the individual videos, the first and last frame are loaded and converted to HSV color space. The hue (H) proves to be most suitable to track the color change, since it shows a large change in value while being least prone to light heterogeneities and noise. Afterwards, the pixel-based difference is calculated for normalization of each pixel value with its position in the matrix (i, j). Frame by frame, the first frame is subtracted and the output divided by the predetermined difference as shown in Eq. 1. Thus, the pixel values range from 0 at the beginning and reach 1 in steady state.

$$H_{norm,i,j}(t) = \frac{H_{i,j}(t) - H_{i,j}(t=0)}{H_{i,j}(t=\infty) - H_{i,j}(t=0)} \quad (1)$$

Each pixel is then checked for its mixing state, in which the pixel is classified as mixed for values ≥ 0.95 and unmixed otherwise. Only the mixed pixels are summed up and divided by the total number of pixels in the mask to calculate the mixed fraction. By means of the percentage representation, the global mixing time is derived by the commonly used 95 % criterion and the corresponding time stamp assigned after which the mixed fraction fulfills the criterion for at least 5 following time stamps.

Mixing map

Besides global mixing time, the spatial distribution of local mixing times offers advanced insights in the mixing process. To extract this information for all mixed pixels of a frame, the corresponding time stamp (t) is stored in a container with identical dimensions as mask. Before a new stamp is written to the container, the previous container value (i, j) is proofed zero for its initial state to avoid an overwrite of already classified pixels. Finally, the container holds all local mixing times and represents the spatial, so-called mixing map of the

https://doi.org/10.24355/dbbs.084-202110251021-0

reactor volume. Due to the movement of the mixed and unmixed regions caused by the macroscopic flow during the mixing process, a second container is implemented. This allows a partial overwrite, since all pixels which were mixed in the previous frame (t - 1) but are unmixed in the current frame (t) are reset. Therefore, the container considers local changes of the mixing state not only from unmixed to mixed but also the other way around and is called updated mixing map in this study. The maps can be divided by the respective global mixing time to achieve an improved comparison of mixing maps resulting from various operating parameters.

RESULTS & DISCUSSION

narrow dark band as well as a second region with less mixing beneath. Another characteristic of the mixing process can be seen from the top left, darkest blue parts, which show the first point of visible tracer distribution. Thus, after the right-hand application, the tracer has to move through the volume without significant expansion until the left turnover point is reached and the color changes.

While the general mixing map reveals information about the macroscopic flow, the circulation of the colored tracer volume blurs this information in the updated mixing map. Therefore, the updated mixing

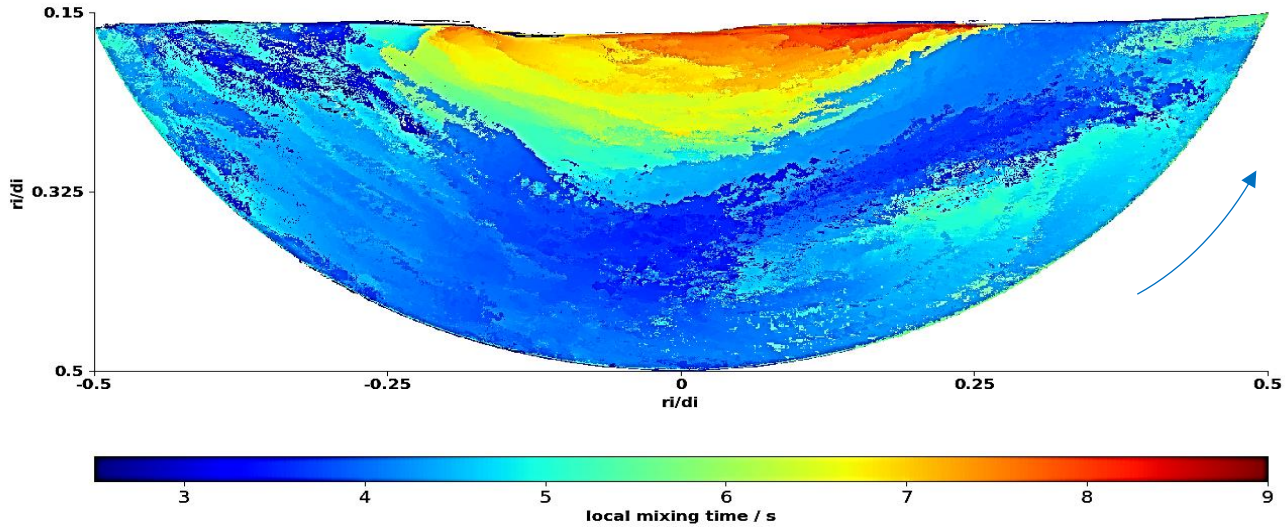

Figure 2: Mixing map, di = 225 mm, application position ri/di = 0,4, filling volume = 120 mL, speed = 25 rpm

Both types of mixing maps provide different insights into the mixing behavior of the reactor and combined the most comprehensive results. The basic mixing map shown in Figure 2 displays the spatial evolution of the initial disturbance induced by the base application at position ri/di = 0,4 during rotation to the right side.

Obviously, the main flow segments the volume into different compartments characterized by fractions of similar local mixing times. Centered near the surface appears an area with comparatively high mixing times which indicate low mixing performance. An explanation may be the dependence of the tangential velocity on the reactor radius that leads to a decrease of the local velocity of the wetted wall as the center of the disc is approached. Furthermore, a circulation flow is visible, represented by the darker blue color in the right half, bounding the low mixed area. This region contains the turnover point of the flow with a subsequent downward trailing vortex that passes tight over the darker colored area and ends in the center blue spot. Apparently, the vortex expands only in a limited space and forms a

map accounts for regions turning back to unmixed state and is not dominated by mixing times assigned at the beginning and during the mixing process. Consequently, it is primary suitable for the representation of critical regions, where the mixing takes the largest period of time. As shown in Figure 3, this region is located directly behind the starting point of the trailing vortex, as well as a region of lesser mixing on the lower right and a late disappearing color streak on the left. Whereby the latter is rather a statistical phenomenon.

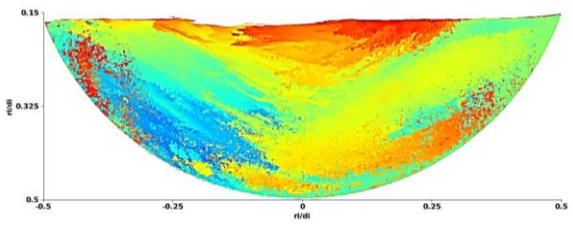

Figure 3: Updated mixing map, di = 225 mm, application position ri/di = 0,4, filling volume = 120 mL, speed = 25 rpm

https://doi.org/10.24355/dbbs.084-202110251021-0

Besides the local mixing time, the global mixing time is the scalar quantity of the mixing process, which is the typical parameter to compare different influencing factors and scale the mixing process. Figure 4 shows the dependence of the global mixing time on rotational speed and filling volume. In general, a high influence of the filling volume appears in an increase of the mixing time when the volume is also increased. This illustrates the importance of a suitably selected filling volume in order to achieve a required mixing performance. In addition, the mixing time becomes smaller at higher rotational speed, as expected. Building on the results, future work will extend the experimental matrix for different reactor dimensions to address the scaling of the mixing process.

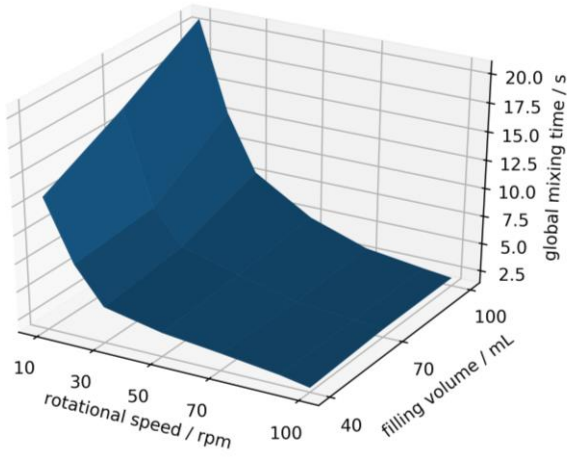

Figure 4: Influence of the rotational speed and filling volume on the global mixing time (95 % criterion)

CONCLUSIONS

The presented, computer vision based method for mixing time determination offers the opportunity to visualize the spatial kinetic of the advancing mixing process. With both mixing maps combined and the global mixing time, it is possible to obtain deep insights in the mixing behavior of a reactor: the dominating macroscopic flow, different mixing zones, critical regions of low mixing as a possible starting point for design optimizations and the scaling of the mixing process with the various influencing parameters. The derivation of local mixing times allows the spatial and temporal history of the mixing process to be taken into account. This can be utilized prospectively for a comparative assessment of different mixing setups and will be applied to the RDR compared to the standard stirred tank reactor. One approach may be the mean of the updated mixing map for similar global mixing times. The spatial distribution is thus converted in a comparable scalar quantity, which has smaller values for a premature, partial tracer distribution. Next to the proposed evaluation algorithm, the mixing behavior of a flat, horizontally mounted cylinder is presented for the first time, providing extensive opportunities for further investigations.

NOMENCLATURE

d_i	[mm]	inner diameter of the hollow disc
r_i	[mm]	inner radius of the hollow disc
$H_{i,j}$	[-]	hue of HSV color space at pixel i, j

REFERENCES

Fitschen, J.; Hofmann, S.; Wutz, J.; Kameke, A. v.; Hoffmann, M.; Wucherpfennig, T.; Schlüter, M. (2021): Novel evaluation method to determine the local mixing time distribution in stirred tank reactors. In: Chem. Eng. Sci. X (10). DOI: 10.1016/j.cesx.2021.100098.

Machado, M. B.; Bittorf, K. J.; Roussinova, V. T.; Kresta, S. M. (2013): Transition from turbulent to transitional flow in the top half of a stirred tank. In: Chem. Eng. Sci., 98 (9), 218 - 230. DOI: 10.1016/j.ces.2013.04.039.

Liu, J.; Svärd, M.; Rasmuson, Å. C. (2015): Influence of Agitation on Primary Nucleation in Stirred Tank Crystallizers. Cryst. Growth Des. 15, 4177 - 4184. DOI: 10.1021/cg501791q.

Bylund, F.; Collet, E.; Enfors, S.-O.; Larsson, G. (1998): Substrate gradient formation in the large-scale bioreactor lowers cell yield and increases by-product formation. In: Bioprocess Engineering 18, 171-180. DOI: 10.1007/s004490050427.

Lakerveld, R.; van Krochten, J. J. H.; Kramer, H. J. M. (2014): An Air-Lift Crystallizer Can Suppress Secondary Nucleation at a Higher Supersaturation Compared to a Stirred Crystallizer. In: Cryst. Growth Des. 14, 3264 - 3275. DOI: 10.1021/cg500090g

Jüsten, P.; Paul, G. C.; Nienow, A. W.; Thomas, C. R. (1998): Dependence of *Penicillium chrysogenum* growth, morphology, vacuolation, and productivity in fed-batch fermentations on impeller type and agitation intensity. In: Biotechnol. Bioeng. 59 (6), 762-775. DOI: 10.1002/(sici)1097-0290(19980920)59:6<762::aidbit13>3.0.co;2-7.

Melton, L. A.; Lipp, C. W.; Spradling, R. W.; Paulson, K. A. (2002): DISMT-Determination of mixing time through color changes. In: Chem. Eng. Commun. 189, 322-338. DOI: 10.1080/00986440212077

https://doi.org/10.24355/dbbs.084-202110251021-0

EFFECT OF CRYOPRESERVATION ON THE INTEGRITY OF COAXIAL ALGINATE CAPSULES

D. Khayyat[1,2*], B. Glasmacher[1,2], O. Gryshkov[1,2]

[1] Institute for Multiphase Processes, Leibniz University Hannover, Germany
[2] NIFE, Lower Saxony Centre for Biomedical Engineering, Implant Research and Development, Stadtfelddamm 34, 30625 Hannover, Germany; *khayyat@imp.uni-hannover.de

ABSTRACT

Encapsulation of clinically relevant cells, such as multipotent stromal cells (MSCs), in three-dimensional (3D) core-shell alginate structures is a promising method for the treatment of various diseases as well as drug testing and development. By utilizing the alginate capsules, drugs and active substances can be delivered specifically to the desired place within the patients' body. The aim of this work was to investigate the effect of cryopreservation on the integrity of cell-free coaxial alginate capsules after thawing using slow freezing to ensure their long-term storage. Alginate capsules were produced by electro-spraying and cryopreserved using different cryoprotective agents (CPAs), incubation time and thawing temperature. The results suggest that the capsules loaded with 10% (v/v) dimethyl sulfoxide (DMSO) and 0.3 M sucrose and using high thawing rates demonstrated a beneficial effect on the integrity of capsules, as compared to 10% (v/v) DMSO alone and applying low thawing rates. This study is a further development towards the application of cryopreservation for long-term storage and the emerging cell-based medicine.

Keywords: electro-spraying, tissue cryopreservation, core-shell capsules, alginate hydrogels, membrane

INTRODUCTION

Regenerative medicine includes a wide range of applications, ranging from organ and tissue transplantation to highly sophisticated tissue engineered scaffolds and cell therapeutics [1]. In particular, stem cell-based cell therapies represent a promising and future-oriented method [2]. MSCs are increasingly required for therapeutic applications due to their differentiation ability. In turn, cryopreservation enables a safe and effective long-term storage of cells [2]. This can ensure the sufficient availability of cells [3]. Studies from the Food and Drug Administration (FDA) confirm that 80% of MSCs submissions use the cryopreservation for a long-term storage and preservation of cells [1].

However, freezing MSCs is associated with many complications. Cell encapsulation in hydrogels is a promising alternative to conventional cryopreservation in suspension. Alginate biomaterial is often used for this purpose due to its gel-forming, high biocompatibility and semi-permeable properties. 3D core-shell gel structures can be produced using coaxial electro-spraying, where the cells are centrally positioned inside the alginate capsules. The hydrogel protects the cells from cryodamage and also acts as an extracellular matrix [4]. It also enables the maintenance of cellular metabolic activities. Moreover, the utilization of coaxial alginate capsules has been shown to lower immune responses in patients, circumventing side effects. A variation in membrane thickness and pore size of the envelope membrane allows a better control of diffusion. Consequently, the delivery of cell therapeutics is made controllable [5, 6].

For a successful cryopreservation in the alginate capsules, the osmotic effects during freezing and subsequent thawing, the thermal behavior of the capsules, and the effects of applied CPAs and their incubation time are important [7, 8]. Therefore, the development of a suitable freezing protocol is required. Gryshkov et al. [9, 10] have already produced and optimized the cell-free and cell-laden core-shell capsules. This paper serves to further develop and improve the integrity of cell-free coaxial alginate capsules (Ø 3000 µm) and is performed with a focus on the CPA loading time (45, 90 min), container type (cryovials), CPAs (DMSO, DMSO + sucrose), thawing temperature (37°C, 60°C) and thawing time (60 s). The aim of this parameter study is to obtain the maximum number of intact alginate capsules after cryo-preservation. The capsules were prepared using the

https://doi.org/10.24355/dbbs.084-202110251021-0

electro-spraying method. The optimization of parameters is performed with reference to the cell encapsulation of MSCs and is used to improve the cryo-preservation protocol of encapsulated MSCs within hydrogels, consisting of alginate.

RESEARCH CONCEPT

All chemicals used in this study were purchased from Carl Roth (Germany), unless stated otherwise. Low viscosity (molecular weight of 100–200 kDa [11], viscosity of 100–300 cP (2%, 25°C), from Sigma-Aldrich) alginate sodium salt from brown algae was used in the current study.

Preparation of coaxial capsules

The production of cell-free core-shell capsules was conducted using the electro-spraying approach developed by Gryshkov et al. [5, 9]. The general process of electro-spraying included the pumping of the alginate solution and cell suspension at defined flow rates through a coaxial nozzle, the application of a high voltage between the nozzle and gelling solution and the transportation of the produced alginate droplets to a bath containing a gelling solution of 100 mM calcium chloride ($CaCl_2$, Carl Roth) for cross-linking. For the core-shell capsules sodium alginates were dissolved in 10 mM 4-(2-hydroxyethyl)-1-piperazi-neethanesulfonic acid (HEPES, pH 7.4) prepared in 0.9% sodium chloride. The final concentration of alginate solution was 2.5% (w/v). The membrane (alginate) and core (HEPES) solutions were pumped simultaneously at different flow rates through the custom developed coaxial nozzle. After gelling for 30 min, the alginate capsules were collected and washed once with a washing solution (20 mM $CaCl_2$ in 10 mM HEPES containing 0.9% NaCl (pH 7.4) and used for further analysis.

The alginate and HEPES solutions were pumped through an outer (outer diameter 1.83 mm, B Braun) and inner (outer diameter 0.4 mm, B Braun) needle using two syringe pumps (KD Scientific). The coaxial nozzle was charged positively, whereas an electrode was grounded and immersed into the gelling solution. The distance between the tip of the outer needle and the surface of the gelling solution represents the spraying distance. The following parameters were applied to produce the alginate capsules with a centrally located core and with an outer diameter of 3000 ± 99 µm, an inner diameter of 1700 ± 90 µm and a membrane thickness of around 650 µm: a high voltage of 12 kV and a ratio of the flow rate of the alginate to the inner fluid (HEPES) of 4:20 (ml/h : ml/h).

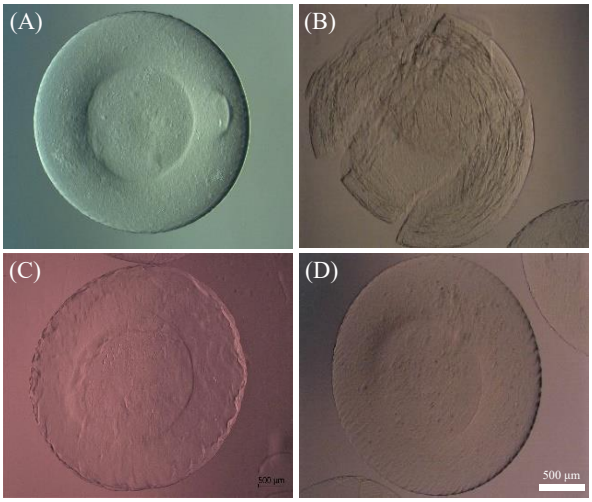

Figure 1: Prepared capsules before freezing (**A**) and the damaging effects of the capsules after thawing (**B–D**). Destroyed capsules (**B**). Damaged capsules (**C**). Here the membrane is not intact and the gel structure is severely damaged. Intact capsules that have an intact outer layer, minor membrane damage, a barely visible core, and a highly visible core (**D**). Scale bars are 500 µm.

Cryopreservation

After washing, the prepared alginate capsules were transferred into cryovials (TPP) with 20 capsules per vial and placed on ice for CPA loading. Afterwards they were incubated for 45 and 90 min in two different cryoprotective solutions: 10% DMSO (DM) and 10% DMSO with 0.3 M sucrose (Sigma-Aldrich) (DMS). The cryoprotective solutions were prepared in a pure cell culture medium supplemented with Fetal Bovine Serum (FBS, Biochrom) in a final concentration of 20% (v/v). In this study, the capsules were frozen "in air", which included removal of the excess of the CPAs after loading. The samples were frozen with 1 K min^{-1} to -80°C in the controlled rate freezer Planer Kryo 560-16 (Planer) and stored in liquid nitrogen in a cryogenic (Fischer Scientific) at -140°C for at least 7 days. Thawing was realized in a water bath pre-warmed to 37°C or 60°C with gentle shaking for 60 s. The last thawing step included addition of pre-warmed Dulbecco's modified Eagle's (DMEM, Biochrom) (37°C or 60°C). After thawing, the capsules were transferred into 6-well culture plates (TPP) and used for further analysis. Analysis and imaging of the capsules were performed using an AxioVert. A1 microscope and ZEN Blue software (Zeiss). The data referring to the capsule integrity was derived according to the damaging effects to the alginate capsules as shown in Figure 1: Category B (destroyed), Category C (damaged) and Category D (intact).

https://doi.org/10.24355/dbbs.084-202110251021-0

Statistical Analysis

Each experiment was repeated three times. The results are represented as mean ± standard deviation (SD) and the values of the intact capsules were assessed for normality according to the applied Shapiro-Wilk test.

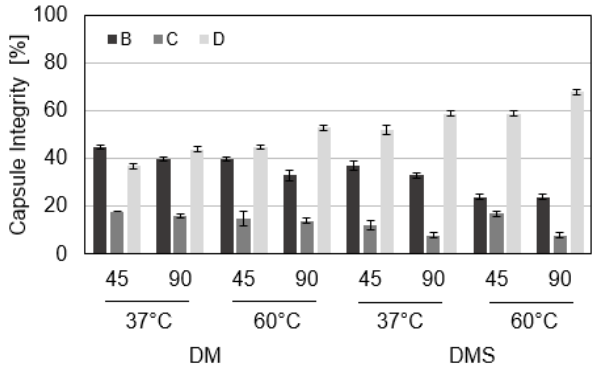

Figure 2: Capsules' integrity after thawing with an incubation time of 45 and 90 min in 10% DMSO (DM) and 10% DMSO with 0.3 M sucrose (DMS). Categorized as [B] destroyed, [C] damaged, and [D] intact. (n = 120).

RESULTS

In this study, core-shell capsules were produced from freshly prepared alginate solutions and samples were analyzed before and after freezing. The effect of 10% (v/v) DMSO (DM) for the applied incubation time of 45 and 90 min (Figure 2) showed that the number of intact alginate capsules increased with an increasing thawing temperature and incubation time. For an incubation time of 90 min and a thawing temperature of 60°C, 45% of alginate capsules were intact. The percentage for (C) was 15% and for (B) 40%. The lowest capsule integrity was obtained with the incubation time of 45 min and the temperature of 37°C. The percentage of intact capsules was 28%. Completely destroyed were 60% and damaged 13%.

Applying the second cryoprotective solution, DMS had different effects on the capsule integrity (Figure 2). The result show that the application of sucrose led to a decrease of destroyed and damaged capsules. Consequently, the samples that were thawed at 37°C and incubated for 45 min had a percentage of 52% of intact capsules. Therefore, these were classified in (D). The percentage of capsules assigned to (C) was 12% and for (B) the percentage was 37%. Increasing the temperature to 60°C, while keeping the incubation time constant at 45 min, caused an increase in intact capsules. The percentage of capsules allocated to (D) was 59%. 17% of the capsules were considered damaged and 24% were completely destroyed. The results (Figure 2) show the effect of the incubation time of 90 min on the capsule integrity. Applying a thawing temperature of 60°C and an incubation time of 90 min accounted for 68% of intact capsules. The best overall results were obtained by using this combination of parameters. Here, 24% of the capsules were found completely destroyed and 8% damaged.

DISCUSSION

Alginate has been investigated and used therapeutically and diagnostically for many biomedical applications due to its biocompatibility, low toxicity and relatively low cost [6, 12]. The semi-permeability of the alginate hydrogel allows the transport of drugs, nutrients, oxygen as well as metabolic products through the alginate, but prevents the attack of high molecular weight substances such as antibodies on the cells transported within the alginate capsules. The idea behind using electro-spraying approach is a coaxial flow of two liquids: alginate as an outer membrane and a cell suspension as a core. Moreover, the core-shell capsules size and the thickness of the alginate membrane can be varied [9, 10]. Based on the results obtained, it can be seen that the alginate hydrogel is an important factor in successfully preserving the alginate capsules using the optimal freezing protocols. Cryopreservation of the low-viscosity alginate capsules was successfully carried out with different percentages of CPAs, independent of the incubation time and thawing temperature.

In the current study several damaging effects can be seen which occur during cryopreservation. This could be due to several reasons: short incubation time of CPAs, poor penetration of CPAs into the alginate capsules, without using of sucrose as well as the thawing time and temperature.

Herein, we also analyzed the effect of the application of sucrose and high thawing temperatures. The utilization of a longer incubation time allowed an extended penetration of the CPA into the alginate capsules. Due to this, the protective properties increased which was reflected in the increase of intact capsules [10]. The longer incubation time caused a 6% increase in capsule integrity. The use of sucrose also supported the capsule integrity due to the fact that sucrose promoted dehydration and reduced the water content in the capsules [13]. Consequently, it prevented capsule bursting, and reducing the number of destroyed capsules. The addition of sucrose resulted in an average increase of 15% in integrity. Although a better result was obtained by the longer incubation time, it is inadvisable

https://doi.org/10.24355/dbbs.084-202110251021-0

to increase the penetration time of CPAs. In case a colonization of cells occurs, CPAs may be toxic to the cells over a longer period of time [2, 14].

CONCLUSIONS & OUTLOCK

In this paper we showed the effect of cryopreservation on the integrity of cell-free coaxial alginate capsules. The study was carried out for different process parameters: variation of the incubation time, CPAs and thawing rates. The aim of this study was to analyze the combination of parameters that showed the maximum number of intact alginate capsules and was performed in view of establishing the freezing protocol for encapsulated MSCs. In this study, we observed that the percentage of intact capsules increased with increasing incubation time and thawing temperature. The addition of 0.3 M sucrose to 10% DMSO caused an increase in capsule integrity. Almost 70% of the capsules survived after thawing and short-term storage. For the further optimization of the freezing protocol, which could result in an increase of intact alginate capsules, would be interesting: increasing the sucrose content, analysis of different cooling rates, optimization of freezing by applying cryobags as well using electroporation-assisted delivery of sucrose and trehalose or similar into MSCs.

ACKNOWLEDGMENT

The authors are grateful to the student Y. Kirupananthan for her excellent technical support. This research was in part supported by Leibniz Young Investigator Grants (LYIG) of the Leibniz University Hannover, Germany.

REFERENCES

[1] Hunt, C. J. (2019). Technical considerations in the freezing, low-temperature storage and thawing of stem cells for cellular therapies. *Transfus Med Hemother*, 46(3), 134-150.

[2] Gryshkov, O. et al. (2015): Multipotent stromal cells derived from common marmoset Callithrix jacchus within alginate 3D environment: effect of cryo-preservation procedures. *Cryobiology* 71 (1), 103-111.

[3] Gryshkov, O. et al. (2014). Encapsulating non-human primate multipotent stromal cells in alginate via high voltage for cell-based therapies and cryopreservation. *PloS one 9*(9), e107911.

[4] Pirnia, A. et al. (2017). Stemness of spermatogonial stem cells encapsulated in alginate hydrogel during cryopreservation. *Andrologia*, *49*(5), e12650.

[5] Gryshkov, O. et al. (2019). Advances in the application of electrohydrodynamic fabrication for tissue engineering. *J. Phys. Conf. Ser.* 1236(1), 012024.

[6] Schwinger, C. (2004). Vergleich verschiedener Verkapselungsarten zur Immobilisierung von Zellen Dissertation. Naturwissenschaftlich Technischen Fakultät, Martin-Luther-Universität Halle-Wittenburg.

[7] Gámez-Pastrana, R. et al. (2011). Thermal events in calcium alginate beads during encapsulation dehydration and encapsulation-vitrification protocols. *Acta Horticulturae*, 908, 47-54.

[8] Mohanty, S. et al. (2016). Impact of alginate concentration on the viability, cryostorage, and angiogenic activity of encapsulated fibroblasts. *Mater. Sci. Eng. C*, *65*, 269-277.

[9] Gryshkov, O. et al. (2014). Process engineering of high voltage alginate encapsulation of mesenchymal stem cells. *Mater. Sci. Eng. C*, *36*, 77-83.

[10] Gryshkov, O. et al (2021). Coaxial alginate hydrogels: From self-assembled 3D cellular constructs to long-term storage. *Int. J. Mol. 22*(6), 3096.

[11] Bruchet, M. et al (2013). Photochemical patterning of ionically cross-linked hydrogels. *Processes*, 1(2), 153-166.

[12] Gombotz, W. R. et al (1998). Protein release from alginate matrices. *Adv. Drug Deliv. Rev.* 31(3), 267-285.

[13] Bachiri, Y. et al (1995). Successful cryo-preservation of suspension cells by encapsulation-dehydration. *Plant Cell Tiss. Org.* 43(3), 241-248.

[14] Sambu, S. et al (2011). Predicting the survival rate of mouse embryonic stem cells cryopreserved in alginate beads. *Proc. Inst. Mech. Eng. H.* 225(11), 1092-1107.

[15] Mutsenko, V. et al (2019). Me2SO-and serum-free cryopreservation of human umbilical cord mesenchymal stem cells using electroporation-assisted delivery of sugars. *Cryobiology*, 91, 104-114.

[16] Pogozhykh, O. et al. (2015). Molecular and cellular characteristics of human and non-human primate multipotent stromal cells from the amnion and bone marrow during long term culture. *Stem Cell Res. Ther.* 6(1), 1-15.

https://doi.org/10.24355/dbbs.084-202110251021-0

SPHERICAL AGGLOMERATION OF BENZOIC ACID USING MEMBRANE EMULSIFICATION

I. Lackowska, M. Dragosavac, B. Benyahia*

[1] Loughborough University; Epinal Way LE11 3TU; Loughborough / United Kingdom
b.benyahia@lboro.ac.uk

ABSTRACT

Spherical agglomeration (SA) is a key crystal shape modification technique commonly used to improve processability and physical properties of active pharmaceutical ingredients (APIs), such as flowability and dissolution. SA involves the introduction of a bridging liquid in the form of droplets into a suspension of API crystals. A novel approach was successfully implemented in this study by adopting a membrane emulsification (ME) system to control the size of bridging liquid droplets and spherical agglomerates. The study investigated ways to achieve the critical quality attributes of the spherical agglomerates by varying operating conditions and design parameters, including mixing rate, bridging liquid injection rate and membrane pore diameter. Antisolvent crystallization of benzoic acid in ethanol (solvent) and water (antisolvent) in presence of toluene as a bridging liquid was used as a case study. Spherical agglomerates of benzoic acid with enhanced quality attributes and mean size of 300 µm were obtained using a membrane pore size of 18 µm, a bridging liquid flow rate of 0.025 mL/min and mixing rate in the range of 800 RPM and 1000 RPM.

Keywords: spherical agglomeration, membrane emulsification, droplet size, benzoic acid

INTRODUCTION

Crystallization is widely adopted in the pharmaceutical industry to purify active pharmaceutical ingredients. In crystallization, the most important challenges are the control of crystal size and shape distributions, polymorphism, and purity. These properties significantly impact the critical quality attributes of the drug product, such as solubility and efficacy, as well as the downstream processability of the resulting crystals such as flowability and filterability (Fysikopoulos et al., 2019). Compared to cuboid and spherical crystals, handling needle-like and plate-like crystals is very challenging due to their very poor flowability and filterability and tendency to break during operation. Several techniques have been developed to modify the crystal shape and aspect ratio including wet milling (Lo et al., 2012), shape additives (Hatcher et al., 2020; Fysikopoulos et al., 2019), layer crystallization (Zhou et al., 2013) and spherical agglomeration (SA) (Orlewski et al., 2018; Peña et al., 2019).

SA is an important shape modification technique which may reduce the number of unit operation and processing steps commonly adopted in the pharmaceutical industry by eliminating processes such as wet granulation. SA is essentially achieved by adding an appropriate bridging liquid at a specific ratio with respect to the mass of crystals, high enough to wet the particles and control the agglomeration process. An effective way to achieve this objective is add the bridging liquid in the form of droplets. Depending on the droplet size of the injected bridging liquid, several mechanisms come into play during the formation of the spherical agglomerates such us adsorption and immersion. The particle size and critical physical properties of the spherical agglomerates are determined by the droplet size distribution of the bridging liquid, mixing conditions and the level of supersaturation. However, the control of the droplet size distribution may be a very challenging task particularly at large scale.

In this work, we propose a novel SA approach based on a membrane emulsification system (Holdich et al., 2010) to effectively control the droplet size distribution of the bridging liquid which in turn can help enhance the critical quality attributes of the spherical agglomerates. Membrane emulsification is a membrane-assisted dispersion process used to generate emulsions of one liquid phase in another immiscible liquid phase, commonly used for oil and water emulsions. It is demonstrated that the membrane pore size widely affects the size and dispersity of the droplets formed. Membrane emulsification systems can be found in many configurations. The one used in this paper employs a dispersion cell with a glass chamber and a nickel

https://doi.org/10.24355/dbbs.084-202110251021-0

membrane at the bottom, where the dispersed phase can be injected through.

The objective of this study is to enhance the critical quality attributes of the spherical agglomerates of benzoic acid by optimizing the critical process parameters (i.e., operating conditions and design parameters) of a fed-batch membrane emulsification system. To achieve this objective, an experimental investigation was conducted to analyze the impact of the bridging liquid flow rate, mixing rate, and membrane pore size on the droplet size and consequently of the size distribution of the spherical agglomerates. In addition, a mathematical model was used to predict the mean droplet size, under the investigated operating conditions, and its impact on the measured mean size of the spherical agglomerates.

RESEARCH CONCEPT

Materials and Methods: A dispersion cell, supplied with a glass chamber holder and a two-blade paddle stirrer, which can hold a flat disc nickel membrane with a pore radius was used, $d_p = 18\ \mu m$ and $33\ \mu m$. Anti-solvent crystallization was performed using 30 wt% benzoic acid (Sigma Aldrich) dissolved in 99.8% ethanol (Fisher Chemical) as the solvent, with deionized water as the antisolvent. Toluene (Fisher Chemical) was used as bridging liquid, to form droplets through the membrane, which would allow for the spherical agglomerates to form. A bridging liquid to API solid weigh ratio (BSR) of 0.7 was used. The crystals were observed under an optical microscope (Nikon Eclipse E100) and fluorescent (Nikon Eclipse TE300) off-line at the end of each crystallization and agglomeration experiment. Agglomerate size was analyzed and measured from optical images using ImageJ.

The spherical agglomeration was achieved in three main steps as shown in Figure 1. Firstly, the crystals were formed using an antisolvent crystallization. A solution of 30 wt.% benzoic acid dissolved in ethanol was added to 36 mL of water present in the dispersion cell to create supersaturation conditions. Once crystals were formed and the system reached equilibrium, the bridging liquid was fed into the system through the membrane forming droplets which initiated the agglomeration process. In the last step, the spherical agglomerates continued to form and grow in absence of any new bridging liquid droplets. Benzoic acid crystals obtained at the end of the crystallization step exhibited mainly needle-like shapes.

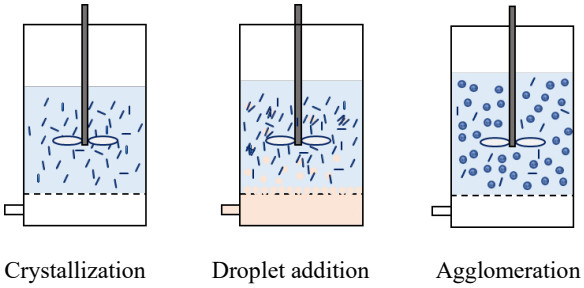

Figure 1: Spherical agglomeration steps

RESULTS AND DISCUSSION

Figure 2 shows the mean size of the bridging liquid droplets as a function of shear stress (mixing conditions) for 2 different membrane pore sizes predicted by a mathematical model which is not presented here for the sake of brevity. This clearly shows that the droplet size decreases as the shear stress increases, and smaller droplets can be obtained with smaller membrane pore sizes. Most importantly, the size of the spherical agglomerates obtained at different bridging liquid flow rates indicate that smaller spherical agglomerates were obtained, as the droplet size decreases then tends to reach a minimum value. To gain better insights, it is important to analyze the size distribution of the spherical agglomerates of benzoic acid. The agglomerate size distribution (ASD) is represented in Figure 3 at three different flow rates of the bridging liquid (Q_{inj}) and at a mixing rate of 800 RPM. Based on these results, smaller mean agglomerate sizes were obtained at lower bridging liquid feed rates (Q_{inj}). In addition, Figure 3 shows that broader size distributions were obtained at high and low bridging liquid feed rates (Q_{inj} = 0.05 mL/min and Q_{inj} = 0.01 mL/min). The best spherical agglomerates were obtained at a medium flowrate Q_{inj} = 0.025 mL/min.

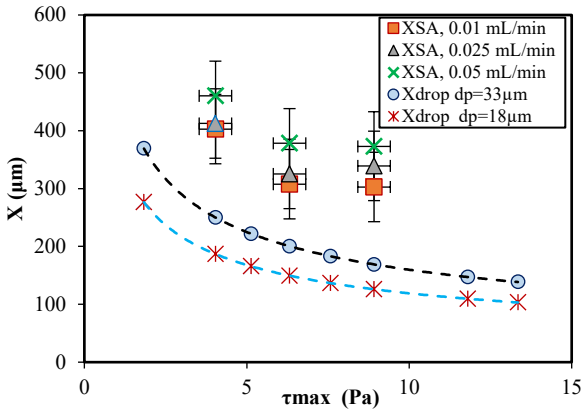

Figure 2: Predicted droplet size at membrane pore diameter d_p=18 and 33µm as a function of shear stress and corresponding measured mean diameter of agglomerates.

https://doi.org/10.24355/dbbs.084-202110251021-0

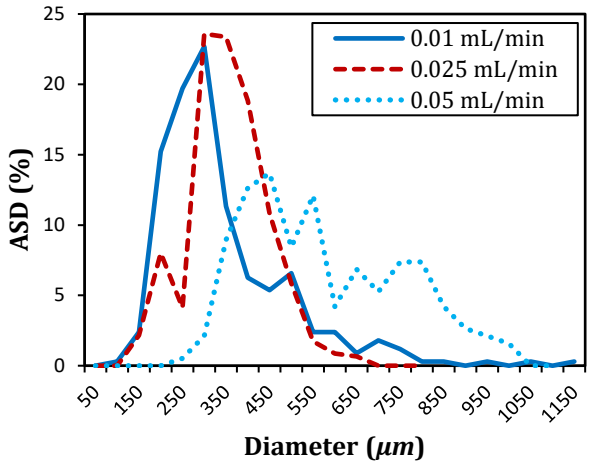

Figure 3: Agglomerate size distribution (ASD) of spherical agglomerates formed at varying Q_{inj} and 800 RPM, nickel membrane, d_p = 33μm.

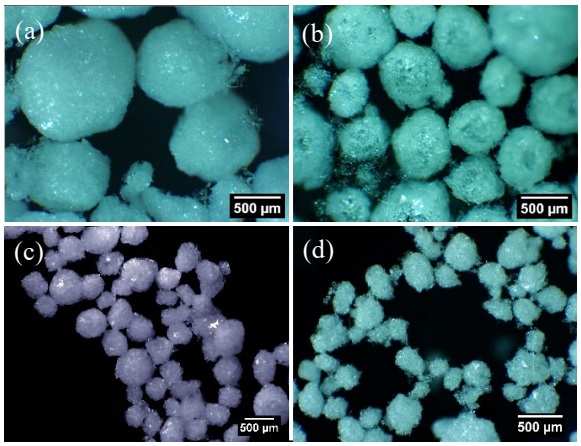

Figure 4: Optical microscopy of the spherical agglomerates of benzoic acid obtained at Q_{inj} = 0.025 mL/min and (a) 600 RPM, d_p = 33μm (b) 800 RPM, d_p = 33μm (c) 1000 RPM, d_p = 33μm (d) 1000 RPM, d_p = 18μm.

Figure 4 shows the optical microscopy of the spherical agglomerates obtained at the same bridging liquid feed rate of 0.025 mL/min at different mixing rates with 2 different membrane pore diameters. The first three images (a-c) represent the spherical agglomerates obtained using a membrane with d_p = 33 μm at different mixing rates, and (d) the spherical agglomerates with a membrane of d_p = 18 μm at 1000 RPM. These results show that large agglomerates with large size distribution are obtained at a lower mixing rate. The best spherical agglomerates were obtained under a mixing rate of 800 RPM and 1000 RPM, under the same Q_{inj} = 0.025 mL/min and using the same membrane pore size. Although the spherical agglomerates obtained under a high mixing rate (1000 RPM) using a small membrane pore size (d_p = 18μm), depicted in Figure 4d, look similar to those obtained under the same mixing rate but with a larger pore size (Figure 4c), the shape distribution and sphericity is enhanced in the latter case.

As no surfactant was added, it was not possible to stabilize and measure off-line the actual size of droplets formed at the membrane surface. The presence of surfactant would allow the formation of more stable small droplets which could result in smaller spherical agglomerates. However, the presence of surfactant may also prevent agglomeration. A process analytical tool such as particle video microscope (PVM) may be employed to measure the size of droplets in real time. However, due to the small size of the dispersion cell, the integration of a PVM probe was not possible. These limitations can be addressed in our future scale-up investigation. Nevertheless, a first principle mathematical model was used to predict the mean droplet size and its influence on the measured properties of the spherical agglomerates.

CONCLUSIONS

Spherical agglomerates of benzoic acid were obtained using a novel approach based on membrane emulsification system. The impact of the operating conditions and design properties were investigated and proved that the system is flexible and suitable to optimize the properties of the spherical agglomerates of benzoic acid. These advantages suggest that the process can be scaled-up reliably which will be the focus of our future work.

The optimization approach was based on both experimental observations and model predictions of the mean size of the bridging liquid droplets. However, a more rigorous modeling approach may be required to predict the properties of the spherical agglomerates.

ACKNOWLEDGMENT

The authors would like to thank the School of AACME, at Loughborough University for funding this project.

REFERENCES

De Luca, G., Di Renzo, A., Di Maio, F.P., et al. (2006) Modelling droplet formation in cross-flow membrane emulsification. *Desalination*, 199 (1–3): 177–179. doi:10.1016/j.desal.2006.03.038.

Egidi, E., Gasparini, G., Holdich, R.G., et al. (2008) Membrane emulsification using membranes of regular pore spacing: Droplet size and uniformity in the presence of surface shear. *Journal of Membrane Science*, 323 (2): 414–420. doi:10.1016/J.MEMSCI.2008.06.047.

https://doi.org/10.24355/dbbs.084-202110251021-0

Fysikopoulos, D., Benyahia, B., Borsos, A., et al. (2019) A framework for model reliability and estimability analysis of crystallization processes with multi-impurity multi-dimensional population balance models. *Computers & Chemical Engineering*, 122: 275–292. doi:10.1016/J.COMPCHEMENG.2018.09.007.

Hatcher, L.E., Li, W., Payne, P., et al. (2020) Tuning Morphology in Active Pharmaceutical Ingredients: Controlling the Crystal Habit of Lovastatin through Solvent Choice and Non-Size-Matched Polymer Additives. *Crystal Growth & Design*, 20 (9): 5854–5862. doi:10.1021/ACS.CGD.0C00470.

Holdich, R., Dragosavac, M., Williams, B., et al. (2020) High throughput membrane emulsification using a single-pass annular flow crossflow membrane. *AIChE Journal*, 66 (6): 1–10. doi:10.1002/aic.16958.

Holdich, R.G., Dragosavac, M.M., Vladisavljevic, G.T., et al. (2010) Membrane Emulsification with Oscillating and Stationary Membranes. *Industrial & Engineering Chemistry Research*, 49 (8): 3810–3817. doi:10.1021/ie900531n.

Lo, E., Mattas, E., Wei, C., Kacsur, D., Chen, C. K. (2012) Simultaneous API Particle Size Reduction and Polymorph Transformation Using High Shear. *Org. Process Res. Dev.*, *16* (1), 102–108. 10.1021/op2002529

Orlewski, P.M., Ahn, B. and Mazzotti, M. (2018) Tuning the particle sizes in spherical agglomeration. *Crystal Growth and Design*, 18 (10): 6257–6265. doi:10.1021/acs.cgd.8b01134.

Peña, R., Jarmer, D.J., Burcham, C.L., et al. (2019) Further Understanding of Agglomeration Mechanisms in Spherical Crystallization Systems: Benzoic Acid Case Study. *Crystal Growth and Design*, 19 (3): 1668–1679. doi:10.1021/acs.cgd.8b01519.

Zhou, L., Su, M., Benyahia, B., Singh, A., Barton, P.I., Trout, B.L., Myerson, A.S., Braatz, R.D. (2013) Mathematical modeling and design of layer crystallization in a concentric annulus with and without recirculation. AIChE J, 59(4), 1308-1321. doi.org/10.1002/aic.14049

https://doi.org/10.24355/dbbs.084-202110251021-0

UV-VIS SPECTRA AS POTENTIAL PROCESS ANALYTICAL TECHNOLOGY (PAT) FOR MEASURING THE DENSITY OF COMPRESSED MATERIALS: EVALUATION OF THE CIELAB COLOR SPACE

Tim D. Lillotte[1], Maike Joester[3], Benjamin Frindt[2], Andreas Berghaus[3], Robert F. Lammens[2], Karl G. Wagner[1]

[1] Department of Pharmaceutical Technology and Biopharmaceutics, University of Bonn, Gerhard-Domagk-Straße 3, 53121 Bonn, Germany; karl.wagner@uni-bonn.de
[2] Solids Development Consult GmbH, Peter-Joseph-Lenné-Str. 11, 51377 Leverkusen, Germany
[3] ColVisTec AG, Max-Planck-Str. 3, 12489 Berlin-Adlershof, Germany

ABSTRACT

In this study, a novel approach was developed for determining the density of compacts using ultraviolet–visible spectrophotometry. The assumption within this context was that a change in density affects the corresponding color information of the compact. From the obtained spectra of the visible range, the color information of the compact was calculated which turned out to be directly proportional to the density of the compact. In comparison, the obtained spectra were analyzed using partial least square regression. The results of this study showed that both methods could be used predicting the density of a compact from the corresponding visible spectrum at identical accuracy. In contrast to the partial least square regression, the correlation of the color information as a direct output parameter of the spectrophotometer with the density required no excessive data pre-processing. Subsequently, the easier and faster data processing of the color information over the partial least square regression, conceives using this novel approach as potential process analytical technology tool for implementation into a compression process e.g., tableting or roller compaction.

Keywords: process analytical technology (PAT), color space, tablet density, spectrophotometry, partial least square regression (PLS)

INTRODUCTION

The monitoring and controlling of the tablet or ribbon density and its corresponding porosity or solid fraction as critical quality attributes (CQAs) have become a major area of interest in the pharmaceutical industry with the goal of implementing fast and reliable measurement methods with the potential being used in process analytical technology (PAT) to ensure product quality particularly during continuous manufacturing.

During the last decades, various methods have been investigated that are based on electromagnetic radiation (NIR, THz etc.). The corresponding electromagnetic spectra are used for the analysis of the density or other mechanical properties, which is usually performed by multivariate data analysis using principal component analysis (PCA) and partial least square (PLS) regression.

However, little has been reported about the use of visible (VIS) spectroscopy for the purpose of monitoring CQAs of pharmaceutical compacts. Therefore, the current study aims to investigate the influence of densification on the corresponding VIS spectra (380 to 780 nm), with the goal to evaluate the use of this effect for determining the density of compacts. In this context, spectral data of different tablets were obtained with a UV-VIS spectrophotometer from ColVisTec AG (Berlin, Germany). In the present work, it was assumed that a change in the density of a compact affects the corresponding L*, a*, b*, C*, and h° values of the CIELAB color space. These values were determined for the compacts followed by comparing the calculated C* values with the density values determined from the geometry and weight of the compact. The obtained regression functions were used as prediction models for the density, and the properties of these functions were compared to PLS regression results to assess the use of the CIELAB color space as a novel tool for predicting the density of compacts.

Note: This abstract only focuses on the evaluation of the CIELAB color space of one of seven blends. The results of the PLS regression and its comparison with the results of the CIELAB color space is featured in [1].

https://doi.org/10.24355/dbbs.084-202110251021-0

MATERIAL AND METHODS

A blend consisting of 99.5% Microcelac® 100 and 0.5% Ligamed® was produced for the production of tablets. Six additional blends were made. However, the results are not shown in this abstract. Please refer to [1] for more information. A FlexiTab® (Röltgen GmbH, Germany) was utilized to produce four tablet batches. Based on the geometry and the weight of the tablets, the respective tablet (envelope) density was calculated.

ULTRAVIOLET-VISIBLE MEASURMENTS

The tablets were investigated using a spectrophotometer "InSpectro X" (ColVisTec AG, Germany). The probe was attached to a 3D printed template holding the tablet under investigation in a defined position. Based on the raw spectral data, the device calculated the L*, a*, b*, C*, and h° values using the spectral information in the range of 380 to 780 nm for each measurement.

CIELAB COLOR SPACE

Linear regression was used to investigate whether the C* value systematically correlated with the density of the tablet.

RESULTS

From the raw spectral data curves, the UV-VIS spectrophotometer calculated the L*, a*, b*, C*, and h° values of the sample under investigation. No pre-processing of the spectral data was performed. The C* value was calculated based on the a* and b* values and was used for a direct correlation with the measured (envelope) density of each individual tablet, according to the assumption that a change in density affects the corresponding color information of the sample. The results of the regression analyses are shown in Fig. 1. For each blend, a good linear relation between the C* value and the density of the tablets was observed, despite the overlap and shift in the raw spectra.

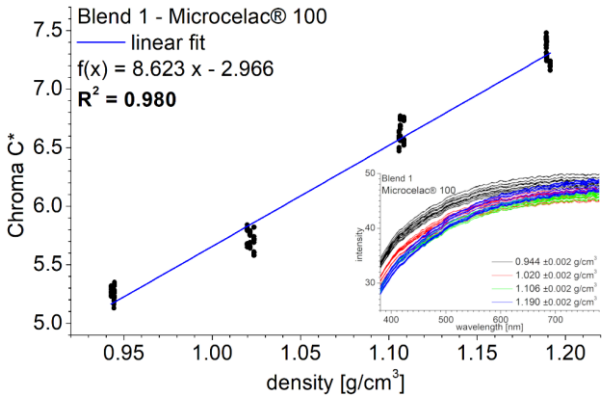

Fig. 1. Linear correlation of the C* value with the tablet (envelope) density.

DISCUSSION

The present study was designed to assess the applicability of the use of a compacts color information for determining its density. The assumption within this context was that a change in density affects the corresponding C* value of the compact. The C* value is a direct output parameter of the UV-VIS device and sufficiently sensitive to a change in density for predicting the density of compacts. The correlation of the C* value with the density can be easily and quickly performed and no additional software tools are required. The spectrophotometer is directly ready to use after calibration using polytetrafluoroethylene (Teflon®). Moreover, no pre-processing of the raw spectral data sets is necessary and the operator can use well-known linear regression to correlate the color information with the density. Altogether, this substantially reduces the amount of work required to establish and to maintain a model for predicting the density and applying it in pharmaceutical processes. Additionally, no skills training in multivariate data analysis and no advanced spectroscopic knowledge is required. This is an advantage over other spectroscopic techniques such as NIR or THz.

CONCLUSIONS

The present study provides a novel method for measuring the density of pharmaceutical compacts, demonstrating that the C* value can be used for this purpose. Please refer to [1] for the following:
The correlation of the C* value with the density was compared to the correlation based on PLS regression. The results of this comparison showed that the correlation results of the C* value were just as accurate as the results by PLS regression. The results of this work support the idea that the color information of the sample can be easily and effectively used for measuring the density using VIS spectroscopy, without the use of time-consuming and complex spectral analysis based on PCA and PLS regression.

REFERENCES

[1] T.D. Lillotte, M. Joester, B. Frindt, A. Berghaus, R.F. Lammens, K.G. Wagner, UV–VIS spectra as potential process analytical technology (PAT) for measuring the density of compressed materials: Evaluation of the CIELAB color space, International Journal of Pharmaceutics. 603 (2021) 120668. https://doi.org/10.1016/j.ijpharm.2021.120668.

https://doi.org/10.24355/dbbs.084-202110251021-0

MULTIFUNCTIONAL USE OF CASEIN AS RELEASE SYSTEM AND BLOCKING LAYER FOR IMPLANT COATINGS

N. Meier[1], H. Menzel[1]

[1] TU Braunschweig; Hagenring 30; Braunschweig / Germany; (nils.meier@tu-braunschweig.de)

ABSTRACT

In situ tissue engineering requires to functionalize the surfaces of implants, to achieve better biocompatibility or to release pharmaceuticals. Often a burst release of such pharmaceuticals takes place and the surface functionality is gone rapidly. Casein-micelles (M-Cas) offer unique release capabilities for hydrophobic and hydrophilic substances. In this work, M-Cas were reconstructed and used as release system for curcumin as a model drug. Modified electrospun polycaprolactone (PCL)-fiber mats were coated with chitosan / tripolyphosphate nanoparticles (CS/TPP-NP) and functionalized with the reconstructed M-Cas. [1] CS/TPP-NPs and Na-caseinate (Cas) were used as blocking layer to slow down the release of curcumin loaded micelles. The layers were investigated by surface zeta-potential (ZP). The release of the curcumin from surfaces was possible and the blocking layers had a significant influence on the kinetics.

Keywords: casein-micelles, surface functionalization, blocking layers, controlled release, tissue engineering

INTRODUCTION

Drug release systems can be applied to implant surfaces, for example, by means of a layer-by-layer (LbL) coating. These systems often suffer from a burst release. Furthermore, the coating process may influence the structure and the release of the drugs. The interpenetration of the layers, which are subsequently applied to the surface, effects the release properties, because often a continues layer not separated ones is formed. In this large layer the substances are widely dispensed and probably released faster as if they had to overcome interfaces at different layers. [2, 3, 4]

Casein is a natural release system and offers the possibility of transporting hydrophilic and hydrophobic substances. [5] It is already used in some medical applications, as in the encapsulation of poorly soluble drugs and in bone tissue engineering as scaffold. Surface modification with casein was also proven feasible. However, working with casein or casein-micelles can be difficult due to preparation and purification steps. [5, 6]

Here we report on using reconstructed casein-micelles as release system for modified electrospun PCL-fiber mats and further adjustment of the release kinetics with additional blocking layers of Na-caseinate.

RESEARCH CONCEPT

Electrospun PCL-fiber mats were modified with CS-g-PCL and further coated with alginate. [1] In order to functionalize this primal scaffold with casein micelles, a positively charge surface was prepared with a layer of CS/TPP-NP. [3] The reconstructed micelles or Na-caseinate now could be coated on the scaffold and used in model system to release curcumin, investigate the release capacity and the blocking efficiency.

Reconstruction of Casein-Micelle

A dialysis method was used to reconstruct casein-micelles. Na-caseinate was dissolved in dest. water (50 mg/mL) and dialyzed (MWCO 3.5 kDa) against a 5 mM $CaCl_2$-solution. The reconstructed micelles were collected after 16 h and characterized by dynamic light scattering (DLS) (nano ZetaSizer ZS) for the size and zeta-potential. [7]

Encapsulation of Curcumin

Curcumin (1 mg/mL) was dispersed in an aqueous micelle solution (1 mg/mL) and was shaken (200 rpm) for 2 h. After an additional 1 h of resting, the loaded micelles in the supernatant were used in the release experiments. [8]

https://doi.org/10.24355/dbbs.084-202110251021-0

Layer-by-Layer build up

In a dipping process CS/TPP-NPs (2 mg/mL) and Na-caseinate / casein-micelles (0.1 mg/mL - 5 mg/mL) were alternately coated onto a silicon-wafer. Each layer was dipped for 10 min and was washed 1 min with 0.1% of acetic acid (only CS/TPP layers) and water. The coatings were dried in a N_2-stream before the ellipsometry measurement. [3, 9]

Layer characterization

Surface zeta-potential measurements (SurPASS 3) of the casein layer on modified fiber mats were performed over a pH range from 9 to 2.

Release experiments

Micelles with encapsulated curcumin (1 mg/mL) were coated on modified fiber mats (8x16 mm). A second group was further coated with blocking layers (2 x (CS/TPP(1 mg/mL)-Cas(0,1 mg/mL))). The release was carried out over 6 h in a Na_2CO_3-buffer (1 mg/mL; pH 11), which is necessary to dissolve the curcumin and quantified by UV/Vis-analysis.

RESULTS

After 16 h of dialysis reconstructed Na-caseinate micelles had a size as z-average of 120 nm and a polydisperse index (PDI) of 0,224. The zeta potential at pH 7.4 was -19.1 mV. Longer dialysis time tend to result in smaller particles.

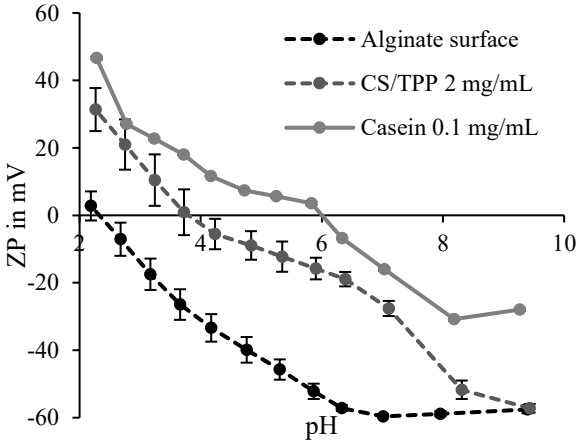

Fig. 1: Zetapotential measured as surface streaming potential measurements of modified PCL fiber mats, with different surface functionalization's, in a pH range from 9 to 2. A 1 mM KCl solution was used as electrolyte. Alginate is used as the negatively charged surface which is further coated with CS/TPP (1 mg/mL) and Na-caseinate (0.1 mg/mL).

The negative charge of reconstructed casein micelles and Na-caseinate itself makes them applicable in a layer-by-layer build-up alternating with positively charged CS/TPP nanogels. Various concentrations of casein were applied. A partial detachment of the casein layers was observed, while the next CS layer was coated. With less concentrated casein solution (0,1 mg/mL), no detachment was observed and the same thickness as after the detachment was reached.

The layers were further characterized by surface streaming potential measurements, shown in Fig. 1. The surface modifications manifest themselves in a change of the isoelectric point (IEP) as well as the general curve shape.

The release data for layers prepared with reconstructed casein micelles and the blocking capacity of additional Na-caseinate layers, is shown in Fig. 2.

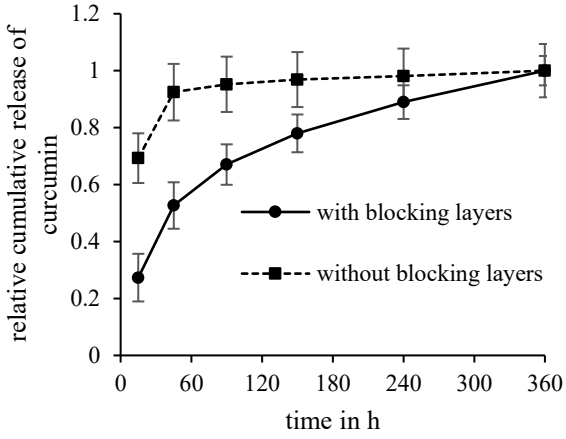

Fig. 2: Relative release of curcumin from fiber mats functionalized with reconstructed casein micelles at 37 °C in a Na_2CO_3 (pH 11), a) without blocking layers and b) with blocking layers (2 x (CS/TPP(1 mg/mL)-Cas(0,1 mg/mL))). The additional blocking layers showed a change in the release kinetics for curcumin.

DISCUSSION

A reconstruction of casein-micelles was possible with the dialysis method. Time, concentration of $CaCl_2$, type of dialysis tube and the temperature are all parameters determining the amount and velocity of the Ca^{2+} diffusion and therefore effect the micelle formation but all these factors can easily be set, and the reconstruction was well reproducible. The casein-micelles had a z-average size of ~120 nm, which is similar to natural micelles (~150 nm). The negative ZP of roughly -20 mV makes them applicable to interact with the positively charged CS/TPP-NP. [5]

https://doi.org/10.24355/dbbs.084-202110251021-0

Curcumin was passively encapsulated by the micelles, after 2 h of shaking and 1 h resting the solution, the micelles had a yellow color. A rest of non-dissolved curcumin was still present at the bottom of the flask, meaning that not all of it could be encapsulated. By determining the undissolved curcumin, the encapsulation efficiency could be calculated. The supernatant of the curcumin loaded micelles were used to build up layers for the release experiments.

In the layer-by-layer method oppositely charged polyelectrolytes or particles are used to build-up the coating. While dipping in the CS/TPP-NP suspension the previously deposited casein layer was partly rinsed off and the layer thickness decreased somewhat. Using less concentrated casein solutions this effect was negligible, actually at a concentration of 0.1 mg/mL Na-caseinate and casein-micelles the thicknesses reached the same levels as without a rinse off effect. The LbL-method results in stable films because of the charge compensation of the two oppositely charged polyelectrolytes as well as the release of small counterions. [4] Furthermore, a certain degree of interpenetration of the layers occurs. In the case of higher casein concentrations besides the amount which is necessary to compensate the charge of the chitosan and to release the TPP ions, additional caseinate is adsorbed due to hydrophobic interactions, which are comparatively weak. However, this part is removed again when the substrate is dipped in the CS/TPP-NP dispersion. Interestingly the same effect occurred with the casein-micelles but in different extent. The layers in general were thicker, because of the Ca^{2+}-crosslinks within the micelles, but still a rinse off effect was observable. Similar explanations apply here. [9]

The coatings prepared by the LbL-method were characterized by surface streaming potential measurements (Fig1). The fundamental alginate layer, used as substrate for further coatings on the fiber mats [1] showed a typical curve shape for acid surfaces, where the zeta-potential rises but stays negative until very low pH values. In contrast, the chitosan/TPP layer behaves atypical. If chitosan/TPP is added as top layer onto the alginate a different behavior is observed (s. Fig1). The zeta-potential is rising faster for the alginate layer, but still negative. Furthermore, a plateau is observed. Decreasing the pH decreases the negative zeta-potential and at as isoelectric point of approximately 4 the potential turns positive This value is somewhat lower than expected for chitosan, Zemljič et. al. [10] reported an IEP of around pH 8. This can be reasoned to be a consequence of the interpenetration of the alginate and chitosan layers, resulting in a mixed layer. Similar observations were made by Sandri et. al. [11] for some chitosan systems and also attributed to the interaction / interpenetration of the layers, resulting in blended layers.

Finally, the casein (c = 0.1 mg/mL) layer was expected to show interpenetration and influences from the underlaying chitosan layer. However, for the casein layer the curve shape and isoelectric point (~6) fits to the literature IEP of the different caseins (~5-6) depending on the orientation and the casein on the surface. [12] With these results it can been assumed, that in this case the zeta potential is not influenced by the underlying chitosan and that there is no or only weak interpenetration. These are important findings for the use of the casein as blocking layers in a release system, because the casein builds a separated but attached layer. It can by hypothesized that the amphiphilic nature of the casein results in a layer with an inner hydrophobic phase, which being a barrier for the released drug.

Releasing curcumin from coated fiber mats with reconstructed casein micelles (1 mg/mL) as release system showed the burst release typical for this kind of release systems. [3] This changed markedly after the deposition of blocking layers (2 x (CS/TPP(1 mg/mL)-Cas(0,1 mg/mL))) on top of the micelles. The release of the curcumin slowed down significantly. The total release curcumin fluctuated between 3.2 µg and 4.6 µg, what strongly depends on the available surface. This proved that casein can be used as blocking layer and that reconstructed casein micelles are indeed a possible release system for hydrophobic substances.

CONCLUSIONS

In this work casein micelles were reconstructed with a dialysis method and were investigated for their use as release system for implant coatings. The direct use of casein-micelles is often not possible because of the requirement of separation and cleaning steps. The reconstructed micelles are more applicable. An encapsulation of curcumin as model drug was possible. Due to the negative charge of Na-caseinate and casein-micelles they can be used for surface modifications using the layer-by-layer method. Na-caseinate was used as blocking layer alternating with chitosan-tripolyphosphate nanoparticles. Surface zeta potential measurements indicated that the lower chitosan layer is not strongly interpenetrating the casein layer. The separation of the casein and the chitosan layers could provide different phases, which must be penetrated by the released substance. Indeed, the release of curcumin

https://doi.org/10.24355/dbbs.084-202110251021-0

as a model drug from fiber mats could be slowed down significantly with these additional “blocking" layers, realizing a more sustained release. It can hypothesized that the inner hydrophobic sections of the casein layers play a major role in the release kinetics. In future studies, the layer interactions will be further analyzed as well as the importance of the hydrophobic character. Furthermore, the casein system will be applied for more relevant drug, like for examples signaling proteins.

ACKNOWLEDGMENT

We would like to thank Ingo Krause and Marc Redling, for preforming a part of the practical work. Furthermore, we acknowledge funding from the *Deutsche Forschungsgemeinschaft* in the framework of the research unit FOR 2180 “Graded Implants” under the Project number 251503496.

REFERENCES

[1] Cassan, Dominik de; Sydow, Steffen; Schmidt, Nadeschda; Behrens, Peter; Roger, Yvonne; Hoffmann, Andrea; Hoheisel, Anna Lena; Glasmacher, Birgit; Hänsch, Robert; Menzel, Henning (2018): Attachment of nanoparticulate drug-release systems on poly(ε-caprolactone) nanofibers via a graftpolymer as interlayer. In: Colloids Surf. B 163, S. 309-320. DOI: 10.1016/j.colsurfb.2017.12.050.

[2] Boudou, Thomas; Crouzier, Thomas; Ren, Kefeng; Blin, Guillaume; Picart, Catherine (2010): Multiple functionalities of polyelectrolyte multilayer films: new biomedical applications. In: Adv. Mater. 22 (4), S. 441-467. DOI: 10.1002/adma.200901327.

[3] Sydow, Steffen; Cassan, Dominik de; Hänsch, Robert; Gengenbach, Thomas R.; Easton, Christopher D.; Thissen, Helmut; Menzel, Henning (2019): Layer-by-layer deposition of chitosan nanoparticles as drug-release coatings for PCL nanofibers. In: Biomater. Sci. 7. DOI: 10.1039/c8bm00657a.

[4] Dercher, Gero; Schlenoff, Joseph B. (ed.) (2004): Multilayer Thin Films. In: Wiley-VCH. ISBN: 3527304401.

[5] Livney, Yoav D. (2010): Milk proteins as vehicles for bioactives. In: Curr. Opin. Colloid Interface Sci 15 (1-2), S 73-83. DOI: 10.1016/j.cocis.2009.11.002.

[6] Raveendran, Sreejith; Rochani, Ankit K.; Maekawa, Toru; Kumar, D. Sakthi (2017): Smart Carriers and Nanohealers: A Nanomedical Insight on Natural Polymers. In: Materials 10 (8), DOI: 10.3390/ma10080929.

[7] Picchio, Matias Luis; Cuggino, Julio César; Nagel, Gregor; Wedepohl, Stefanie; Minari, Roque Javier; Alvarez Igarzabal, Cecilia Inés; Gugliotta, Luis Marcelino; Calderón, Marcelo (2018): Crosslinked casein-based micelles as a dually responsive drug delivery system. In: Polym. Chem. 9 (25), S. 3499-3510. DOI: 10.1039/C8PY00600H.

[8] Pan, Kang; Luo, Yangchao; Gan, Yundi; Baek, Seung J.; Zhong, Qixin (2014): pH-driven encapsulation of curcumin in self-assembled casein nanoparticles for enhanced dispersibility and bioactivity. In: Soft Matter 10 (35), S. 6820-6830. DOI: 10.1039/c4sm00239c.

[9] Szyk-Warszyńska, Lilianna; Kilan, Katarzyna; Socha, Robert P. (2014): Characterization of casein and poly-L-arginine multilayer films. In: J. Colloid Interface Sci. 423, S. 76-84. DOI: 10.1016/j.jcis.2014.02.031.

[10] Zemljič, Lidija Fras; Plohl, Olivija; Vesel, Alenka; Luxbacher, Thomas; Potrč, Sanja (2020): Physicochemical Characterization of Packaging Foils Coated by Chitosan and Polyphenols Colloidal Formulations. In: Int. J. Mol. Sci., 21 (2). DOI: 10.3390/ijms21020495.

[11] Sandri, Giuseppina; Rossi, Silvia; Bonferoni, Maria Cristina; Miele, Dalila; Faccendini, Angela; Del Favero, Elena; Di Cola, Emanuela; Icaro Cornaglia, Antonia; Boselli, Cinzia; Luxbacher, Thomas; Malavasi, Lorenzo; Cantu', Laura; Ferrari, Franca (2019): Chitosan/glycosaminoglycan scaffolds for skin reparation. In; Carbohydr. Polym. 220, S. 219-227. DOI: 10.1016/j.carbpol.2019.05.069.

[12] Belitz, H.-D.; Grosch, Werner, Schieberle, Peter (2007): Lehrbuch der Lebensmittelchemie. Springer 6. Aufl. ISBN: 978-3-540-73201-3.

https://doi.org/10.24355/dbbs.084-202110251021-0

TOWARDS MICRO ELECTRICAL IMPEDANCE TOMOGRAPHY ON CHIP

D. Metz[1,2], B. Matheis[1], I. Constantinou[1,2]

[1] Technische Universität Braunschweig, Institute for Microtechnology; 38124; Braunschweig, Germany; d.metz@tu-braunschweig.de

[2] Technische Universität Braunschweig, Zentrum für Pharmaverfahrenstechnik (PVZ); 38106; Braunschweig, Germany

ABSTRACT

This work presents initial design and testing of a miniaturized electrical impedance tomography platform. Electrical impedance tomography (EIT) provides a low-cost, non-invasive, radiation-free type of imaging and can be relatively easily implemented on other miniaturized systems like microfluidics. Herein, we describe a miniaturized EIT on chip, along with its measurement setup and image reconstruction pipeline. First imaging results demonstrating a well-functioning setup are presented and form the basis for further investigations.

Keywords: Electrical Impedance Tomography

INTRODUCTION

Electrical impedance tomography (EIT) is a low-cost, non-invasive, and radiation-free type of medical imaging [1–3]. EIT relies on the estimation of the conductivity of an object, based on currents/voltages applied to its surface. A typical medical application of EIT is the study of respiratory patterns. In this case, electrodes are placed on a transverse plane around the patient's chest. During breathing, the volume of the lungs changes. This change can be measured as a change in conductivity, since air and lung tissue have different conductivities [4]. In this project, we aim to miniaturize EIT for future applications in the characterization of biological samples on other miniaturized platforms such as organ-on-chip. Previous work already demonstrates the utility of EIT for detection/monitoring of biological samples and provides some proof of concept [5, 6]. The cost of integrating and fabricating electrodes in such microsystems remains low compared to the extensive and fast imaging results that can be achieved. However, progress still needs to be made on the reconstruction side, since low resolution remains a limitation.

Herein, we report on the development of a simplified EIT-on-chip platform and first imaging results using the implemented measurement setup. A brief introduction to the principles of EIT measurement and theory of image reconstruction is followed by a detailed description of the chip, its design, and the measurement setup. Finally, a first EIT-imaging experiment is presented and discussed.

RESEARCH CONCEPT

EIT measurement principle

During EIT measurements, samples are placed within an electrode array positioned on the inner surface of an imaging chamber. Then N small alternating currents $i_{i,j}$ are injected between electrode pairs i and j. After a short delay intended to allow the electric field to build up inside the cell culture chamber, a series of M voltage measurements are made between electrode pairs ($U_{i,j}$) for each injection. A complete measurement set of $N \times M$ voltages is obtained and used for the reconstruction of impedance maps. Different electrode arrangements, injection and measurement patterns can be used. A commonly used ring arrangement of 16 electrodes, as shown in Figure 1, is usually employed in combination with the “adjacent” injection and measurement pattern. Currents and voltages are injected and measured between each neighboring electrode ($j = i + 1$). In this case, the measurement set is composed of 16 injections x 16 measurements = 256 voltage measurements.

https://doi.org/10.24355/dbbs.084-202110251021-0

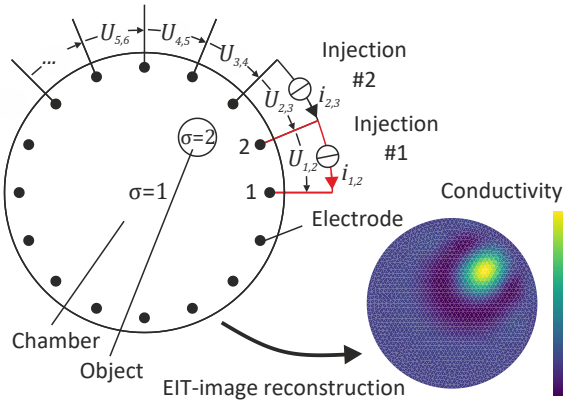

Figure 1: Principle of EIT measurement in a chamber with 16 electrodes arranged in a ring configuration. Adjacent injection and measurement pattern is partially shown.

EIT image reconstruction

In EIT, the conductivity $\boldsymbol{\sigma}$ of a body can be related to the measured voltages $\boldsymbol{U}$ through a non-linear function, F, also known as the forward model, as:

$$\boldsymbol{U} = F(\boldsymbol{\sigma}) \qquad (1)$$

In practice, this relation is linearized and reduced to a Jacobian matrix $\boldsymbol{J}$ as given in Eq. (2). This matrix describes the sensitivity of the electrode array for the given injection and measurement pattern. For more detailed definitions, see the works in [4, 7].

$$\boldsymbol{U} = \boldsymbol{J} \cdot \boldsymbol{\sigma} \qquad (2)$$

EIT image reconstruction is achieved by solving the inverse problem, where $\boldsymbol{U}$ is known and $\boldsymbol{\sigma}$ is searched. Usually this is done using standard regularization methods such as the one-step Gauss-Newton method [8]. In this work, the open-source Python package pyEIT has been used for image reconstruction [3]. Less developed than the popular open-source Matlab toolbox EIDORS [9], pyEIT allows rapid prototyping of EIT systems and is easily extensible. In pyEIT, a 2D chamber can be modeled as a finite element model using a reimplemented "distmesh" generator in Python. Typical dynamic EIT image reconstruction techniques are implemented and can be easily used.

This work focused on time-difference imaging (see also frequency-difference in [6]) using the dynamic Jacobian matrix reconstruction method implemented in the pyEIT package, similar to the one-step Gauss-Newton method. For EIT imaging, the voltage differences $\Delta\boldsymbol{U} = \boldsymbol{U_t} - \boldsymbol{U_0}$ need to be formed from the current measured voltages $\boldsymbol{U_t}$ and the initial voltages $\boldsymbol{U_0}$ (reference), and used to calculate the normalized conductivity changes $\Delta\boldsymbol{\sigma}$ as follows:

$$\Delta\boldsymbol{\sigma} = -((\boldsymbol{J}^T\boldsymbol{J} + \lambda\boldsymbol{R})^{-1} \cdot \boldsymbol{J}^T) \cdot \Delta\boldsymbol{U_{nom}} \qquad (3)$$

where λ is the regularization hyperparameter, $\boldsymbol{R}$ is the regularization matrix as: $\boldsymbol{R}_{i,i} = [\boldsymbol{J}^T\boldsymbol{J}]_{i,i}^{\ p}$ and $\Delta\boldsymbol{U_{nom}} = \frac{\Delta\boldsymbol{U}}{|\boldsymbol{U_0}|}$ are the normalized voltage differences. Here $\lambda = 0.01$, and $p = 0.5$ were used.

Chip platform

The ultimate goal of the project is to build an organ-on-chip platform similar to the one shown in Figure 2a, capable of monitoring the growth or behavior of cells (or other biological samples) placed/cultured in the center of the chamber, e.g., on a membrane. For EIT measurements within the chamber volume, electrode arrays should be integrated at the bottom and top of the chamber. As a first step, a simpler platform was developed and investigated, with an electrode array integrated on only one side of the chamber (Figure 2b). The platform consists of a 10 × 20 mm microfabricated chip (Figure 2c) placed in a 3D-printed holder to obtain an imaging chamber with a diameter of 5 mm and a height of 2 mm.

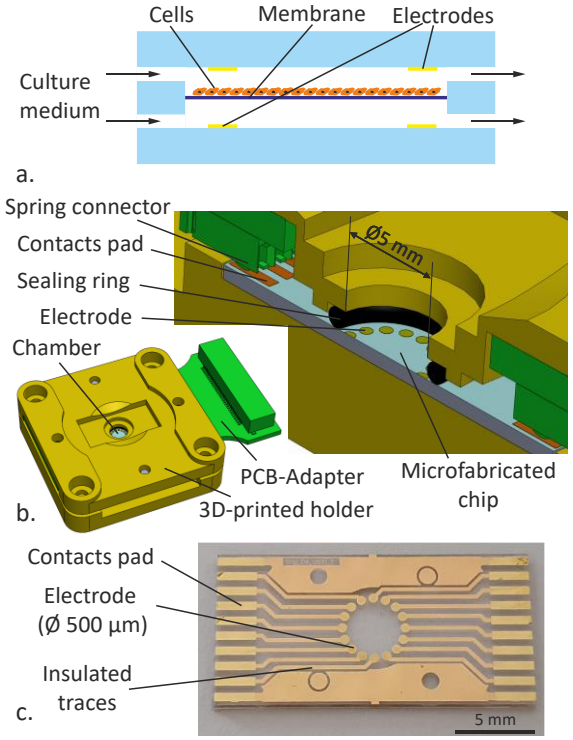

Figure 2: a. Schematic of planned organ-on-chip with electrode arrays on top and bottom of cell culture chamber, b. chip used in this work, electrode arrays only on one side, c. microfabricated chip used in b.

Electrodes of sputtered gold (about 400 nm thickness) were fabricated on the chip made of glass and structured by photolithographic wet etching. Finally, the electrical traces were insulated using a PECVD silicon oxide (SiO2) layer (about 300 nm thickness). Contact pads were placed at the ends of the chip for fast and easy electrical contacting of the electrodes. These contact

https://doi.org/10.24355/dbbs.084-202110251021-0

pads match the spring connectors of the PCB adapter for the EIT measuring device (Figure 3).

EIT measurement setup

An EIT device from Sciospec GmbH [10] was used for the EIT measurements (Figure 3). The device can deliver injection currents from 10 mA down to 100 nA with a frequency range of 100 Hz – 100 kHz and measure the voltages of up to 32 channels simultaneously. Voltages are measured using lock-in amplifier electronics in combination with a special "SineFit" algorithm from Sciospec. The connection to the OoC is made via a high-speed coaxial cable from Samtec (FCF8, see also connector FCS8).

A custom graphical user interface (GUI) was implemented in Python using pyQt5 to set up the device, capture and store the measurement voltages. The corresponding top view of the chamber was captured using a micro-camera. Thanks to multiprocessing implementation, this GUI allows live viewing of the measurement data and EIT imaging with pyEIT at a rate of up to 1 frame/s.

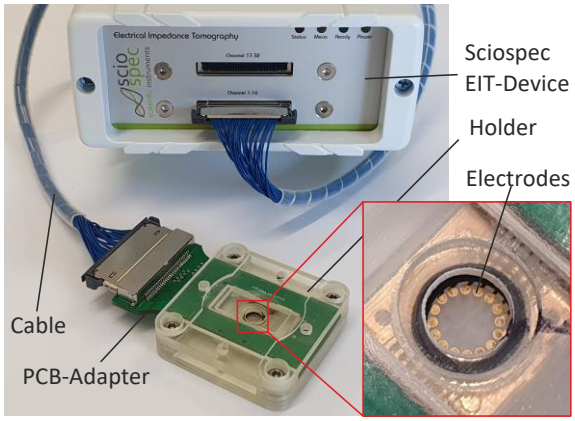

Figure 3: Micro-EIT platform connected to the Sciospec EIT measurement device.

RESULTS

To validate the measurement setup, the chamber was filled with Danieau's solution (conductive liquid) [11]. After measuring the reference/initial voltage $\boldsymbol{U_0}$, an object (Ø1 × 0.4 mm) made of an insulator (EPDM) was inserted into the chamber at two different positions. For both positions, the voltages $\boldsymbol{U_{ti}}$ were measured and an EIT image was calculated using the difference with $\boldsymbol{U_0}$. Measurements were performed with an injection current of 10 µA at a frequency of 10 kHz and adjacent injection and measurement patterns.

Figure 4 shows both experiments, the 256 measured voltages differences $\boldsymbol{\Delta U}$, the EIT reconstructed image, and a top view image of the chamber for comparison. The reconstructed impedance map shows normalized conductivity difference in comparison with the chamber without object. Each 16 measurements correspond to one injection pattern. In Figure 4a, we can observe that the highest voltage difference happens around injection #14 ($i_{14,15}$), which coincides with the position of the object. The position of the object, based on the chamber-top-view, was added to the reconstructed image as a circle to appreciate the reconstruction quality.

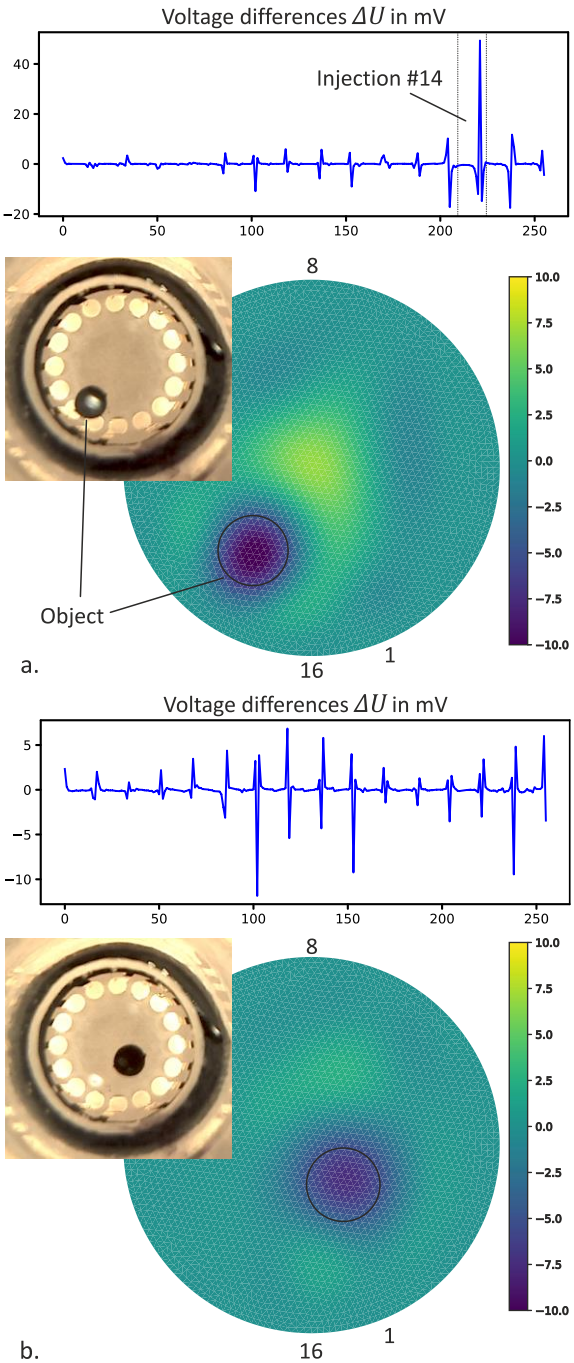

Figure 4: EIT imaging results with objet at different positions.

https://doi.org/10.24355/dbbs.084-202110251021-0

DISCUSSION

In Figure 4, same conductivity changes can be observed for the same object in the same liquid but at a different positions. Also, the position of the object in the EIT image matches its actual position in the chamber. This attests to a successful EIT imaging, validating the developed setup. A better contrast between the object and the medium can be observed in Figure 4a than in Figure 4b. This is related to the high sensitivity of the ring electrode arrangement with adjacent patterning and an object closer to the electrodes, as shown in [3]. However, this also leads to more artefacts, as observed in Figure 4a.

CONCLUSIONS

In this work, a first version of a miniaturized EIT has been presented and first investigations show the good functionality of the measurement setup and image reconstruction implemented on Python using the pyEIT package.

In the future, further investigations will be performed specifically for the imaging of biological samples. Additionally, modeling in pyEIT should be extended for better modeling in 2D and 3D (e.g. with planar electrodes). The use of machine learning should also be explored to improve image resolution and quality of the reconstruction [7]. In the future, a closed chip design will be considered for constant volume during long-term experiments.

ACKNOWLEDGMENT

This work has been performed within the framework of the SMART BIOTECS alliance between the Technische Universität Braunschweig and the Leibniz Universität Hannover. This initiative is supported by the Ministry of Science and Culture (MWK) of Lower Saxony, Germany.

REFERENCES

[1] A. Adler and A. Boyle, "Electrical Impedance Tomography: Tissue Properties to Image Measures," *IEEE transactions on bio-medical engineering*, vol. 64, no. 11, pp. 2494–2504, 2017, doi: 10.1109/TBME.2017.2728323.

[2] D. S. Holder, Ed., *Electrical impedance tomography: Methods, history and applications*. Bristol: Institute of Physics, 2005. [Online]. Available: http://www.loc.gov/catdir/enhancements/fy0653/2005279767-d.html

[3] B. Liu *et al.,* "pyEIT: A python based framework for Electrical Impedance Tomography," *SoftwareX*, vol. 7, pp. 304–308, 2018, doi: 10.1016/j.softx.2018.09.005.

[4] A. Adler and A. Boyle, "Electrical Impedance Tomography," in *Wiley Encyclopedia of Electrical and Electronics Engineering*, J. G. Webster, Ed.: Wiley, 1999, pp. 1–16.

[5] Y. Yang, J. Jia, S. Smith, N. Jamil, W. Gamal, and P.-O. Bagnaninchi, "A Miniature Electrical Impedance Tomography Sensor and 3-D Image Reconstruction for Cell Imaging," *IEEE Sensors J.*, vol. 17, no. 2, pp. 514–523, 2017, doi: 10.1109/JSEN.2016.2631263.

[6] Y. Yang and J. Jia, "A multi-frequency electrical impedance tomography system for real-time 2D and 3D imaging," *The Review of scientific instruments*, vol. 88, no. 8, p. 85110, 2017, doi: 10.1063/1.4999359.

[7] M. Schwarz, M. Jendrusch, and I. Constantinou, "Spatially resolved electrical impedance methods for cell and particle characterization," *Electrophoresis*, vol. 41, 1-2, pp. 65–80, 2020, doi: 10.1002/elps.201900286.

[8] A. Adler, T. Dai, and W. R. B. Lionheart, "Temporal image reconstruction in electrical impedance tomography," *Physiol. Meas.*, vol. 28, no. 7, S1-11, 2007, doi: 10.1088/0967-3334/28/7/S01.

[9] A. Adler and W. R. B. Lionheart, "Uses and abuses of EIDORS: an extensible software base for EIT," *Physiol. Meas.*, vol. 27, no. 5, S25-42, 2006, doi: 10.1088/0967-3334/27/5/S03.

[10] Sciospec, *Discover Sciospec's powerful EIT platform - Sciospec.* [Online]. Available: https://www.sciospec.com/eit/ (accessed: Jul. 20 2021).

[11] "Danieau's Solution," *Cold Spring Harbor Protocols*, vol. 2013, no. 5, pdb.rec074260-pdb.rec074260, 2013, doi: 10.1101/pdb.rec074260.

https://doi.org/10.24355/dbbs.084-202110251021-0

CHARACTERIZATION OF POLYMERIZED IONIC LIQUIDS-BASED HYDROGELS

A. Mildner[1,2], F. M. Teubner[1,2], J. Großeheilmann[1,2]

[1] Technische Universität Braunschweig, Institute for Chemical and Thermal Process Engineering; Langer Kamp 7, 38106 Braunschweig, Germany; a.mildner@tu-braunschweig.de

[2] Technische Universität Braunschweig, Center of Pharmaceutical Engineering; Franz-Liszt-Str. 35a, 38106 Braunschweig, Germany

ABSTRACT

Polymerized Ionic Liquids (PILs) are hydrogels synthesized from ionic liquids. They combine the positive characteristics of ionic liquids and polymers which is why they have a wide range of applications, e.g. in the pharmaceutical sector. They are characterized by properties such as high mechanical strength, biocompatibility, and favorable swelling behavior. In this study, the extremely high mechanical strength of novel polymerized ionic liquids (PILs)-based hydrogels was confirmed by mechanical tests. The swelling behavior was studied of hydrogels based on 1-Vinyl-3-alkylimidazolium bromide with different crosslinkers in various solvents – aqueous and organic.

Keywords: Hydrogel, Polymerized Ionic Liquids, Swelling Properties, Mechanical Properties

INTRODUCTION

Hydrogels are a unique class of polymeric materials that have a three-dimensional network structure which can absorb and retain large amounts – from few percent to thousands of times their dry weight – of water without dissolving. The insolubility as well as mechanical properties or swelling behavior are due to the chemical and/or physical crosslinker and its amount [Hussain, 2013]. Furthermore, there are hydrogels with a number of useful properties such as self-healing or biocompatibility [Ahmed, 2015]. Due to the favorable properties of hydrogels, there are numerous applications of hydrogels in medical and pharmaceutical fields, as contact lenses, as materials for artificial skin or drug delivery systems, but they also have potential applications as immobilization matrices for e.g. enzymes and catalysts [Grollmisch, 2018] or in other fields.

Most Hydrogels, which include polymerized ionic liquids (PILs) are formed by click-chemistry [Boehnke, 2015]. This has the advantage of no undesirable by-products being formed. The remaining PILs combine the features of ILs (e.g., ionic conductivity, thermal, and chemical stability, tunable solution properties) and the properties of polymers [Eftekhari, 2017].

For all the applications mentioned, however, it is crucial to know as much as possible about the properties of hydrogels in order to be able to use them in the most targeted way.

SYNTHESIS OF HYDROGELS

To characterize the hydrogels, the dimensionally stable PILs are being obtained by radical polymerization. An imidazolium-based ionic liquid bearing a vinyl group is polymerized with a crosslinker. Different crosslinkers, such as *N,N'*-Methylenebisacrylamide and Tri(ethylenglycol)divinylether, are used (Figure 1). There are several variations during synthesis, which have a decisive effect on the synthesis of the hydrogel, e.g. the content and type of crosslinker, water content and the ionic liquid monomer. At the same time, however, the properties of the hydrogel are of course also influenced by the variation. Another significant influence on the properties has the storage of the hydrogels, hence all experiments were performed with specimens, which were dried in a climatic chamber at a constant temperature of 25 °C and a relative humidity of 60% for different durations. All hydrogels were prepared in a specified size (d = 10 mm).

https://doi.org/10.24355/dbbs.084-202110251021-0

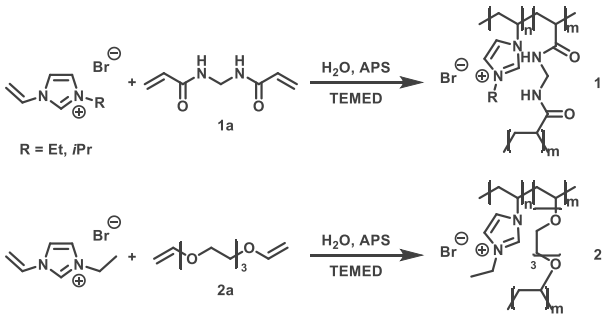

Figure 1: Radical polymerization of an imidazolium-based ionic liquid bearing a vinyl group, [VRIm][Br] – 1-Vinyl-3-alkylimidazolium bromide and cross-linker 1a *N,N'*-Methylenebisacrylamide (BisA); 2a Tri(ethylenglycol)divinylether (TEGDVE). APS – Ammonium peroxydisulfate, TEMED – *N,N,N',N'*-Tetramethylethane-1,2-diamine.

CHARACTERIZATION

Swelling Behavior

The swelling behavior of any polymer is significantly influenced by several factors such as the structure of the monomers used for hydrogel production, but also by the type and amount of crosslinker. Depending on the properties of the polymer network, the swelling behavior also changes with changes in external conditions, such as different solutions and solvents.

Table 1: Hydrogel - solvent combinations tested for swelling behavior at 23 °C.

Hydrogel \ Solvent	0.9% NaCl	0.1 M HCl	Ethanol	Acetone	Ethyl acetate
poly(VEImBr/BisA)	x	x			
poly(V*i*PrImBr/BisA)	x	x	x	x	x
poly(VEImBr/TEGDVE)	x				

Swelling measurements were performed in different solvents (Table 1) and analyzed gravimetrically. The drying conditions were 25 °C and 60% relative humidity (rh). The swelling ratio (SR) was determined as follows, as is common [Carvalho, 2013]:

$$SR = \frac{M_t - M_0}{M_0}. \qquad (1)$$

In Figure 2, a solvent-dependent swelling and shrinking can be observed. In the aqueous solutions, the hydrogel swells significantly, with the greatest swelling observed in HCl. In the solvents ethanol, acetone and ethyl acetate the hydrogel shrinks, with swelling occurring in ethanol after 1440 min.

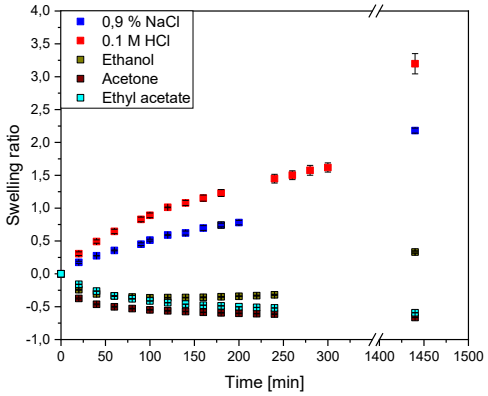

Figure 2: Swelling behavior of poly(V*i*PrImBr/BisA) hydrogels in different solvents at 23 °C.

That the swelling is not only dependent on the solvent, but also on the hydrogels respectively, IL monomers and crosslinkers used are shown in Figure 3. Here, a significantly higher swelling ratio can be observed with poly(VEImBr/TEGDVE). Poly(VEImBr/BisA) and poly(V*i*PrImBr/BisA) with the same crosslinker, show less difference in swelling behavior.

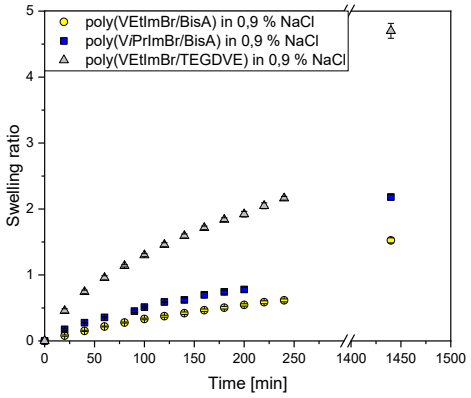

Figure 3: Swelling behavior of poly(VEImBr/TEGDVE), poly(VEImBr/BisA) and poly(V*i*PrImBr/BisA) in 0.9% NaCl solution at 23 °C.

https://doi.org/10.24355/dbbs.084-202110251021-0

Mechanical Properties

Due to their high water content hydrogels possess generally a weak mechanical strength. However, the advantage of PILs-based hydrogels over e.g. alginate-based hydrogels is their significantly higher mechanical stability [Bandomir, 2014].

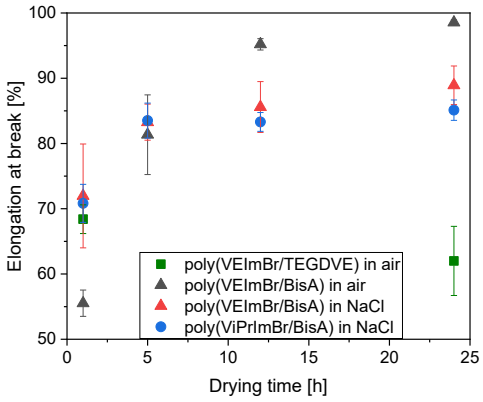

Figure 4: Elongation tests of poly(VEImBr/TEGDVE), poly(VEImBr/BisA) and poly(V*i*PrImBr/BisA) hydrogels with different degrees of drying at 25 °C and 60% rh partially in 0.9% NaCl solution with a loading speed of 0.1%/s.

The mechanical properties of poly(VEImBr/BisA), poly(V*i*PrImBr/BisA), poly(VEImBr/TEGDVE) were analyzed by means of elongation tests (Figure 4) and cyclic stress-strain relations (Figure 5). The influence of different drying times and also the influence of the surrounding medium (air or physiological saline solution) on mechanical behavior were investigated.

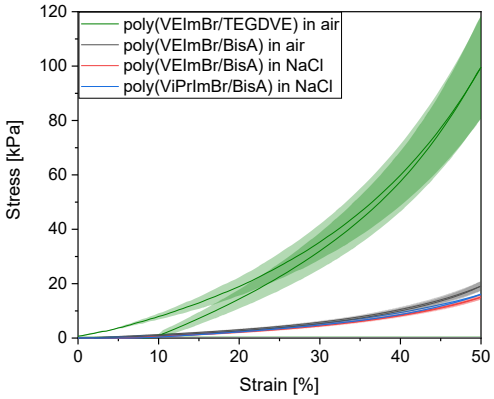

Figure 5: Cyclic stress-strain relation of poly(VEImBr/TEGDVE), poly(VEImBr/BisA) and poly(ViPrImBr/BisA) hydrogels with a drying time of 1 h at 25 °C and 60% rh partially in 0.9% NaCl solution with a loading speed of 0.1%/s.

The mechanical properties are affected by the IL monomer, composition, cross-linking density, degree of drying or swelling and drying method. Depending on the composition, they are compressible up to 98.5% without crack formation in the air and up to 88.9% in physiological saline solution. They show a reversible compression up to a strain increase of max. 8% for poly(VEImBr/TEGDVE) hydrogels. In comparison, the withstand stress differs significantly.

CONCLUSIONS

Stable PILs-based hydrogels were successfully synthesized by a radical polymerization. Two different ionic liquid monomers and two different crosslinkers were used. The swelling behavior and mechanical properties of the resulting hydrogels were analyzed. It was shown that the swelling behavior is solvent-dependent and depends on the composition of the hydrogel. The hydrogels exhibit high swelling behavior in aqueous media, while they shrink in organic media. The highest swelling ratio was observed in 0,1 M HCl. In a direct comparison in 0.9% NaCl solution of the different hydrogels, poly(VEImBr/TEGDVE) shows by far the greatest swelling ratio. The mechanical stability of the tested hydrogels has been extremely high, whereby the stability of the hydrogels increases with the drying time. The poly(VEImBr/BisA) hydrogel has shown a compression up to 98.5% without crack formation after 24 h drying time in the air and up to 88.9% in physiological saline solution and withstand a stress in the air up to 19.1 kPa. In comparison, poly(VEImBr/TEGDVE) hydrogels break slightly earlier, but withstand a much higher stress up to 99.6 kPa.

ACKNOWLEDGMENT

This work has been carried out within the framework of the SMART BIOTECS alliance between the Technische Universität Braunschweig and the Leibniz Universität Hannover. This initiative is supported by the Ministry of Science and Culture (MWK) of Lower Saxony, Germany.

The authors thank DFG for financial support [GR 5483/1-1].

https://doi.org/10.24355/dbbs.084-202110251021-0

NOMENCLATURE

APS	Ammonium peroxydisulfate
Bis A	*N,N'*-Methylenebisacrylamide
IL	Ionic Liquid
M	Mass [kg]
PILs	Polymerized Ionic Liquids
rh	relative humidity
SR	Swelling Ratio
TEGDVE	Tri(ethylenglycol)divinylether
TEMED	*N,N,N',N'*-Tetramethylethane-1,2-diamine
VEImBr	1-Vinyl-3-ethylimidazolium bromide
V*i*PrImBr	1-Vinyl-3-*iso*propylimidazolium bromide

REFERENCES

Ahmed, E. M. (2015): Hydrogel: Preparation, characterization, and applications: A review. In: J. Adv. Res. 6, S. 105–121. DOI: 10.1016/j.jare.2013.07.006.

Bandomir, J.; Schulz, A.; Taguchi, S.; Schmitt, L.; Ohno, H.; Sternberg, K.; Schmitz, K.; Kragl, U. (2014): Synthesis and Characterization of Polymerized Ionic Liquids: Mechanical and Thermal Properties of a Novel Type of Hydrogels. In: Macromol. Chem. Phys. 215, S. 716-724. DOI: 10.1002/macp.201400009.

Boehnke, N.; Cam, C.; Bat, E.; Segura, T.; Maynard, H. D. (2015): Imine Hydrogels with Tunable Degradability. In: Biomacromolecules 16 (7), S. 2101–2108. DOI: 10.1021/acs.biomac.5b00519.

Carvalho, R. N. L. de; Lourenço, N. M. T.; Gomes, P. M. V.; Fonseca, L. J. P. da (2013): Swelling Behavior of Gelatin-Ionic Liquid Functional Polymers. In: J. Polym. Sci. Part B Polym. Phys. 51 (10), S. 817–825. DOI: 10.1002/polb.23252.

Eftekhari, A.; Saito, T. (2017): Synthesis and Properties of Polymerized Ionic Liquids. In: Eur. Polym. J. 90, S. 245–272. DOI: 10.1016/j.eurpolymj.2017.03.033.

Grollmisch, A.; Kragl, U.; Großeheilmann, J. (2018): Enzyme Immobilization in Polymerized Ionic Liquids-based Hydrogels for Active and Reusable Biocatalysts. In: SynOpen 2, S. 192-199. DOI: 10.1055/s-0037-1610144.

Hussain, T.; Ansari, M.; Ranjha, N. M.; Khan, I. U.; Shahzad, Y. (2013): Chemically Cross-Linked Poly(Acrylic- *Co* -Vinylsulfonic) Acid Hydrogel for the Delivery of Isosorbide Mononitrate. In: Sci. World J. 2013, S. 1–9. DOI: 10.1155/2013/340737.

https://doi.org/10.24355/dbbs.084-202110251021-0

PREDICTION OF POWDER FLOW OF PHARMACEUTICAL MATERIALS FROM PHYSICAL PARTICLE PROPERTIES USING MACHINE LEARNING

L. Pereira Diaz[1], C.J. Brown[1], A.J. Florence[1]

[1] University of Strathclyde/ CMAC; 99 George St, G1 1RD; Glasgow/UK; laura.pereira-diaz@strath.ac.uk (presenting author underlined)

ABSTRACT

Understanding powder flow and how it affects pharmaceutical manufacturing process performance remains a significant challenge for industry. This work aims to improve decision making for manufacturing route selection, achieving the key goal of digital design within Industry 4.0 of being able to better predict properties whilst minimizing the amount of material required and time to inform process selection during early-stage development. A Machine Learning model approach is proposed to predict the flow properties of new materials from their physical properties. The model's implementation will enhance manufacturing quality by taking advantage of the data generated throughout the manufacturing process.

Keywords: pharmaceutical manufacturing, pharmaceutical materials, particle characterization, Machine Learning, digital design.

INTRODUCTION

Understanding powder flow and how it affects pharmaceutical manufacturing process performance remains a significant challenge for industry, adding cost and time to the development of robust production routes. It is therefore crucial improve our understanding of powder flow and how this relates to both tableting and capsule filling. Tablet formation can be addressed by several techniques; however, direct compression (DC) and wet granulation (WG) are the most widely used in industrial operations. DC offers lower-cost manufacturing due to it provides streamlined process with fewer steps compared with other techniques. However, to achieve the full potential benefits of DC for tablet manufacture, this places strict demands on material flow properties, blend uniformity, compactability, and lubrication, that need to be satisfied. On the other hand, WG improves flowability and compactability while preventing segregation through the use of binding agents and secondary process steps although it is not suitable for materials which are sensitive to heat or moisture. WG is, therefore, more expensive and time consuming. Due to these economic advantages, DC is increasingly the preferred technique for pharmaceutical companies for oral solid dose manufacture, consequently making the flow prediction of pharmaceutical materials of increasing importance (Schaller et al., 2019; Trementozzi et al., 2017). Flow properties are influenced by the particle size and shape, which are defined upstream during crystallization and/or milling processes. Currently suitability of raw materials and/or formulated blends for DC requires detailed characterization of the bulk properties. A key goal of digital design within Industry 4.0 is to be able to better predict properties whilst minimizing the amount of material required and time to inform process selection during early-stage development.

Traditionally, powder flow has been measured by experimental methods, such as angle of repose, bulk density, Carr's compressibility index, Hausner ratio, and FT4 powder rheometer. However, they are time and material consuming, which is inefficient at the beginning of the material development.

There have been several publications of different approaches to estimate powder flow, such as the study of packing efficiency based on measuring particle size of granular intermediates using Principal Component Analysis (PCA) (Sandler & Wilson, 2010), a big-data approach using shear cell test (Megarry, Swainson, Roberts, & Reynolds, 2019), the study of granular Bond number, which correlates to the flow function coefficient (Ghadiri et al., 2020); or using statistical modelling techniques (Barjat et al., 2021), which is focused on the prediction of flowability for loss in weight feeders.

https://doi.org/10.24355/dbbs.084-202110251021-0

RESEARCH CONCEPT

This work aims to improve decision making for manufacturing route selection in the early stages of the drug product manufacturing process development when time and amount and cost of available material are at a premium. A Machine Learning (ML) model approach is proposed to predict the flow properties, specifically the flow function coefficient (FFc) of a new material from its physical particle properties. The aim is that the model produced as an outcome can help decide whether a new material is suited for DC.

Initially, unsupervised learning algorithms were used; however, these were not useful to classify the data. Consequently, supervised learning algorithms were selected for classification, where FFc was defined as the target property (dependent variable), and the independent variables were particle size and shape distribution, and bulk density. The training data was experimentally generated using the Powder Rheometer – FT4 and a dynamic image analysis (QIC/PIC). Furthermore, a testing data set was generated to validate the model.

RESULTS

The data set used to build the ML model included 115 fully characterised materials. Regarding particle size distribution, 42 of the materials had a D50 smaller than 100 µm, 56 had a D50 between 100 µm and 250 µm, and 17 had a value of D50 greater than 250 µm. Concerning particle shape, most of the materials' aspect ratio falls between 0.6 and 0.8, which corresponds with a cubic shape (Yu, Liao, Bharadwaj, & Hancock, 2017). Based on the FFc, the 27 materials were classified into class 1 (cohesive materials with FFc < 4), 34 were classified into class 2 (easy-flowing materials, 4 < FFc < 10), and 54 materials were classified into class 3 (free-flowing materials, FFc > 10). The physical particle properties were ranked according to their correlation with the target variable, resulting particle size distribution (D10 and D50) and aspect ratio distribution (a90) the variables that provided more information.

Table 1: Number of Instances per class regarding their flow function coefficient and powder behaviour.

FFc	Behaviour	Number of materials
< 4	Cohesive	27
4 < FFc < 10	Easy flowing	34
>10	Free flowing	54

The supervised learning algorithms selected were compared between each other to analyse their performance; and the model was thereafter validated using the external data set, for which 6 of the 8 materials included were correctly classified.

DISCUSSION

A wide range of materials were included in the training dataset. Among the algorithms selected, Random Forest (RF) exhibited the best performance (0.802), which means that there is a probability of 80.2 % for the algorithm to correctly classify the powder flow class of a new material. The other algorithms included in this study exhibited a performance higher than 70 %. Regarding the validation set, 75 % of the materials were correctly classified.

CONCLUSIONS

The ML model's implementation enables the prediction of the material flow properties from their physical properties, enabling rapid decision-making regarding manufacturing route selection, achieving a key goal of digital design of being able to better predict properties whilst minimizing the amount of material and time required to inform process selection during early-stage development. This work suggests that particle size and shape distribution are sufficient to enable accurate prediction of flow properties, and hence, the application of this model will enhance manufacturing quality by taking advantage of the data generated throughout the manufacturing process.

ACKNOWLEDGMENT

Dr Ebenezer Ojo

Dr Cameron Brown

Prof Alastair Florence

https://doi.org/10.24355/dbbs.084-202110251021-0

REFERENCES

Barjat, H., Checkley, S., Chitu, T., Dawson, N., Farshchi, A., Ferreira, A., . . . Tobyn, M. (2021). Demonstration of the Feasibility of Predicting the Flow of Pharmaceutically Relevant Powders from Particle and Bulk Physical Properties. *Journal of pharmaceutical innovation, 16*(1), 181-196. doi:10.1007/s12247-020-09433-5

Ghadiri, M., Pasha, M., Nan, W., Hare, C., Vivacqua, V., Zafar, U., . . . Nadimi, S. (2020). Cohesive Powder Flow: Trends and Challenges in Characterisation and Analysis. *KONA, 37*, 3-18. doi:10.14356/kona.2020018

Megarry, A. J., Swainson, S. M. E., Roberts, R. J., & Reynolds, G. K. (2019). A big data approach to pharmaceutical flow properties. *INT J PHARMACEUT, 555*, 337-345. doi:10.1016/j.ijpharm.2018.11.059

Sandler, N., & Wilson, D. (2010). Prediction of granule packing and flow behavior based on particle size and shape analysis. *Journal of pharmaceutical sciences, 99*(2), 958-968.

Schaller, B. E., Moroney, K. M., Castro-Dominguez, B., Cronin, P., Belen-Girona, J., Ruane, P., . . . Walker, G. M. (2019). Systematic development of a high dosage formulation to enable direct compression of a poorly flowing API: A case study. *INT J PHARMACEUT, 566*, 615-630. doi:10.1016/j.ijpharm.2019.05.073

Trementozzi, A. N., Leung, C.-Y., Osei-Yeboah, F., Irdam, E., Lin, Y., MacPhee, J. M., . . . Zawaneh, P. N. (2017). Engineered particles demonstrate improved flow properties at elevated drug loadings for direct compression manufacturing. *Int J Pharm, 523*(1), 133-141. doi:10.1016/j.ijpharm.2017.03.011

Yu, W., Liao, L., Bharadwaj, R., & Hancock, B. C. (2017). What is the “typical” particle shape of active pharmaceutical ingredients? *Powder Technology, 313*, 1-8.

https://doi.org/10.24355/dbbs.084-202110251021-0

Tow-Photon Polymerization (2PP) enables 3D microsystems for Pharmatechnology

E.Taiedinejad[1,2], P. Erfle[1,2], C. Bausch[3], A. Dietzel[1,2]

[1] Technische Universität Braunschweig, Institut für Mikrotechnik; 38124; Braunschweig; Germany; e.taiedinejad@tu-braunschweig.de

[2] Technische Universität Braunschweig, Zentrum für Pharmaverfahrenstechnik- PVZ Franz-Liszt-Straße 35a, 38106 Braunschweig, Germany

[3] Fraunhofer-Institut für Mikrotechnik und Mikrosysteme IMM; Carl-Zeiss-Straße 18-20; 55129 Mainz; Germany

ABSTRACT

Two-photon polymerization(2PP) is a process for three-dimensional (3D) micro-and Nano structuring based on the locally controlled curing of liquid precursors (light-sensitive resins) by photochemical triggered polymerization. In this decade, will be hearing a lot about this technic being applied to pharmaceutical applications like fabricating 3D microchannels for nanoparticle precipitation, nano-porous membranes and scaffolds for cell culturing, biomimetic organ-on-chip systems. This paper presents 2pp applied microsystems for continuously generating lipid nanoparticles which are one of the most important drug carrier system. The most important advantages of 2pp is manufacturing 3D shapes that is not possible with lithographic micro and nano fabrication technologies. Also, it will be shown how 2pp fabricated microchannel can be integrated with continuous size measurement by flowDLS for the feed-back controlled generation of nanoparticles.

Keywords: Two-photon polymerization (2PP), 3D micro structure, pharmaceutical applications

INTRODUCTION

Two-photon polymerization (2PP) is an emerging technology for the manufacturing of 2D, 2.5D and 3D polymer structures with feature sizes from approx. 200 nm to several millimeters. In the laser focus, a sufficiently high intensity of the laser light causes local non-linear absorption and polymerization and thus curing of the coating. The use of a galvo scanner enables the precise control of the laser light in the resist, which allows a step-by-step construction of a complex three-dimensional object. It can be used in manufacturing of micro-mixers with different 3D parts like nozzles for coaxial injection, a sequence of stretch-and-fold elements and inlet filters, and many 3D structures that cannot be realized by conventional 2.5D techniques [1].

As examples Fig 1 shows two different 3D flow focusing micro-mixers that were fabricated with 2PP technics.

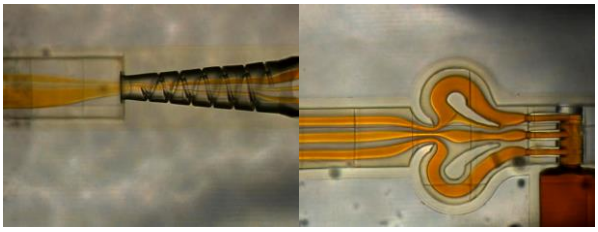

Fig 1. indicates 2 different 3D flow focusing micro-mixers fabricating with 2PP technic.

RESEARCH CONCEPT

With the advent of micro-mixers, another opportunity arose for the bottom up production of lipid nanoparticles as carrier systems or nanoparticle drugs. Lipid in a

https://doi.org/10.24355/dbbs.084-202110251021-0

water-miscible solvent is mixed with an aqueous solution and particles of less than 100 nm and narrow size distributions precipitate. A further advantage of microfluidic low-energy processing is that high temperatures, high shear stresses, high pressures and product contamination due to mill erosion which can cause damage to the active ingredients are avoided [2]. But still, the biggest obstacle is fouling by deposition of lipid on the channel walls, leading to a higher nanoparticle polydispersitye and even channel blocking [3]. Recently, a coaxial lamination mixer (CLM) enabled by 2PP was introduced to completely eliminate contact of the organic phase with the channel walls while efficiently mixing organic and aqueous [1].

A very unique application of 2PP fabricated micro-channels is the combination of controllable microfluidic nanoparticle generation with dynamic light scattering (DLS) for particle size analysis [6]. The system envisaged is a feedback-regulated nanoparticle reactor is to be realized with which the size, size distribution and shape of the manufactured particles can be precisely adjusted and a long-term stable process ensured. This is the aim of a cooperation project between Institute for Microtechnology (IMT) at the TU Braunschweig with the flowDLS developed at the Fraunhofer Institute for Microtechnology and Microsystems (IMM) in Mainz. The necessary verification of particle properties by measurement and counting has so far only been possible within a separate analytical system after preparation is completed. The evaluation of the nanoparticles in a collected sample provides only statements about a sample produced within a longer period of time and does not open any possibilities to constantly influence the precipitation process in the micro mixers or the emulsifying systems as this is only possible by in-situ measurement in the channels.

Fig. 2 shows the important parts of the flowDLS system including a laser, a detector for the scattered light and the transparent 3D micromixer for generating nanoparticles fabricated with 2PP technology. Laser light can shine through an optical aperture into the channel and the scattered light can give information about the particle size and morphologies.

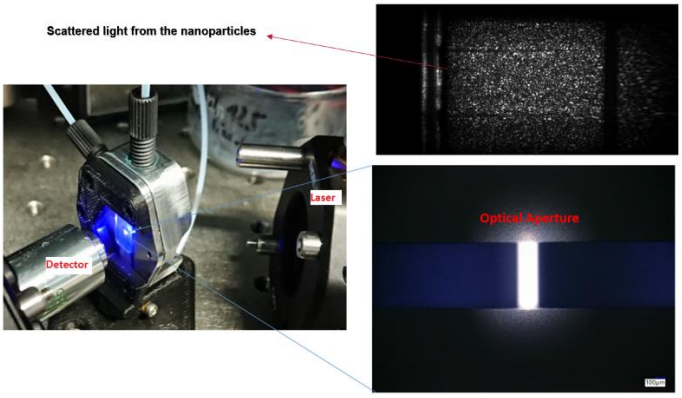

Fig 2- *The FlowDLS system for online and continuous measurement of generated nanoparticle inside the microfluidic channels.*

CONCLUSIONS

2pp can open a window of new opportunities to pharmaceutical engineering in fields where processes in micro and nano devices can be used beneficially. This technique enables fabrication of very complicated 3D designs and shapes with different non-toxic and even biocompatible polymers. An example is given by the microfluidic precipitation device that can be integrated with flowDLS nanoparticle measurement for feedback controlled nanoparticle production.

ACKNOWLEDGEMENT

This work is supported by the Deutsche Forscghungsgemeinschaft in the frame of the project ´´Detected (DLS feedback controlled Continuous particle production) ´´. This work is carried out within the Detected project between Technical Universität Braunschweig and Fraunhofer-Institut für Mikrotechnik und Mikrosysteme (IMM).

https://doi.org/10.24355/dbbs.084-202110251021-0

REFERENCES

1 Erfle, Peer, Riewe, Juliane, Bunjes, Heike, and Dietzel, Andreas, 'Goodbye fouling: a unique coaxial lamination mixer (CLM) enabled by two-photon polymerization for the stable production of monodisperse drug carrier nanoparticles ', Lab on a chip, 21/11 (2021) 2178-2193

2- Sinha, Biswadip; Müller, Rainer H.; Möschwitzer, Jan P. (2013): Bottom-up approaches for preparing drug nanocrystals. Formulations and factors affecting particle size. ln: *International Journal of Pharmaceutics* 453 (1), S. 126-141. DOI: 10.1 016/j.ijpharm.2013.01.019

3- Dietzel, Andreas (Ed.) (2016): Microsystems for pharmatechnology: Manipulation of fluids, particles, droplets, and cells. Springer, Cham. ISBN 978-3-319-26920-7

4- Erfle, Peer; Riewe, Juliane; Bunjes, Heike; Dietzel, Andreas (2017): Optically monitared segmented flow for controlled ultra-fast mixing and nanoparticle precipitation. ln: *Microfluidics and Nanofluidics* 21 (12), S. 1089. DOI: 10.1007/s10404-017-2016-2.

5- Liu, Lili; Cai, Xiaoshu; Zhang, Jie; Xu, Chengze (2015): Particle-size Measurements in a Microchannel with Image Dynamic Light Scattering Method. ln: *Procedia Engineering* 102, S. 904-910. DOI: 10.1 016/j.proeng.2015.01.211.

6- Destremaut, Fanny; Salmon, Jean-Baptiste; Qi, Ling; Chapel, Jean-Paul (2009): Microfluidics with on-line dynamic light scattering for size measurements. In: Lab on a chip 9 (22), S. 3289–3296. DOI: 10.1039/b906514h.

https://doi.org/10.24355/dbbs.084-202110251021-0

PHYSICAL STABILITY OF AMORPHOUS SOLID DISPERSIONS: HISTORICAL EXAMPLES AND SHELF-LIFE EXTRAPOLATION

Frank Theil[1], Kristin Lehmkemper[2], Yanxia Li[3]

[1] Analytical R&D, AbbVie Germany, Knollstraße, 67061 Ludwigshafen am Rhein
[2] Drug Product Development, AbbVie Germany, Knollstraße, 67061 Ludwigshafen am Rhein
[3] Drug Product Development, AbbVie Inc., 1 N Waukegan Road, North Chicago, IL 60064

ABSTRACT

Amorphous solid dispersions (ASDs) of a poorly water-soluble active pharmaceutical ingredient (API) in a polymer matrix can enhance the water solubility and improve the bioavailability of the API. Many ASD products are kinetically stabilized, and the inhibition of crystallization of an API within and beyond shelf life is still a matter of debate, since the formation of crystals may impact bioavailability. We present the first literature examples of ASD long-term stability studies over up to 25 years under ambient storage conditions where no API crystallization was observed. Additionally, a risk assessment and mitigation strategy of API crystallization in packaged ASD drug products (DP) is outlined. The risk of shelf-life crystallization and the respective mitigation steps are assigned for different DP development scenarios. Ultimately, the physical stability of ASD DPs during shelf-life storage is modeled by quantifying crystal growth kinetics by transmission Raman spectroscopy (TRS), modeling the impact of water sorption on the glass-transition temperature of the ASD, and predicting the moisture uptake by the packaged ASD DP during storage. This approach is applied to an ASD of an AbbVie-internal compound showing stability beyond the anticipated shelf-life.

Keywords: Amorphous Solid Dispersions, Crystal Growth, Transmission Raman Spectroscopy, Shelf-Life, Risk-Assessment

INTRODUCTION

Poor aqueous solubility and therefore scarcity of bioavailability of active pharmaceutical ingredients (APIs) is one of the main challenges in the development of solid oral dosage forms during the last few decades in the pharmaceutical industry.[1, 2] Formulating the API as an amorphous solid dispersion (ASD) has been proven to successfully enhance bioavailability of many APIs classified as biopharmaceutical classification system (BCS) class II and class IV.[3, 4] Many ASD formulations are thermodynamically unstable but kinetically stabilized due to low molecular mobility in the glassy ASD formulation.[5, 6] Accelerated API crystallization at high drug loads (DL) in kinetically stabilized ASDs is considered a potential risk for both, patients and pharmaceutical companies.[7]

In this work the long-term physical stability of two kinetically stabilized ASDs is presented: a 15 %DL ASD of Fenofibrate was investigated after 15 years of storage under uncontrolled ambient conditions, and a 20 %DL ASD of Nifedipine even after 25 years.[8, 9] Those observations show that even kinetically stabilized ASDs can be crystal free way beyond the desired pharmaceutical shelf-life.

Additionally, a strategy for crystallization risk assessment of ASD products, based on monitoring crystal growth in ASDs using transmission Raman spectroscopy (TRS), is discussed. Our approach classifies the crystallization risk in the drug product (DP) based on accelerated open dish studies. Depending on the observed data, proper mitigation steps are advised. In case of an anticipated crystallization in the packaged DP over shelf-life, the actual crystal growth in the DP is estimated. For this step, open dish crystallization rates obtained at accelerated conditions are combined with modeling of the glass transition temperature T_g and water content of the packaged DP during storage.

RESEARCH CONCEPT

One of the key factors in ASD formulations is the optimization of the drug load. It is essential that the drug

https://doi.org/10.24355/dbbs.084-202110251021-0

INNOVATIVE CEROSOMES AS CARRIERS FOR AN ENHANCED DERMATOSES' THERAPY

A. Vovesná[1], T. Mužíková[1], J. Zbytovská[1]

[1] University of Chemistry and Technology Prague, Faculty of Chemical Technology, Department of Organic Technology, Technická 5, 166 28 Prague, Czech Republic

ABSTRACT

Dermatoses are skin diseases caused by lowered level of lipids in the intercellular lipid matrix of skin's uppermost layer *stratum corneum*. A promising therapy is the application of liposomally formulated skin lipids (ceramides, cholesterol, fatty acids). These so called cerosomes proved very effective in disrupted skin barrier repair; however, they aim primarily on a mechanical surface restoration. For this reason an interesting idea is to combine the cerosomes and anti-inflammatory drugs (such as hydrocortisone) used for the treatment of pathophysiological processes in the skin. Unfortunately, liposomes generally show low drug encapsulation rates, hence they would not be very effective carriers. On the other hand, great encapsulation effectivity can be found in lipid nanocapsules (LNCs). We therefore aimed to create a combined system cerosomes-LNCs that would ensure the skin barrier restoration thanks to the ceramides and simultaneously effectively deliver hydrocortisone as a representative of anti-inflammatory drugs into lower layers of the skin. In this work, we characterized the formulations by dynamic light scattering and transmission electron microscopy to assess their size and morphology.

Keywords: atopic dermatitis, ceramides, cerosomes, lipid nanocapsules, hydrocortisone

INTRODUCTION

Human skin is the most effective barrier protecting our bodies from xenobiotics, UV light or bacteria. It ensures the proper thermoregulation and limits the water loss. All these vital properties are possible thanks mainly to the uppermost layer of the skin – *stratum corneum* (SC) and its unique composition. Its main building blocks are the skin cells keratinocytes that are connected by a complex intercellular lipid matrix. This lipid matrix consists of ceramides (40–50%), fatty acids (15–25%), cholesterol (20–25%) and cholesterol sulfate (5–10 %) (Harding, 2004).

Skin, as any other organ, can be affected by a disease that changes or limits its basic functions. The most common ones one can encounter nowadays are atopic dermatitis, or generally dermatoses, or psoriasis. These diseases are accompanied by loss of skin hydration, dryness and elevated permeation rates of xenobiotics. The affected sites are reddish and itchy, which can lead to the necessity to scratch the area and therefore to the probability to carry an infection into the deeper layers of the skin and to further spread of the disease. One of the common signs of the diseases compromising the skin barrier is the change in the SC lipid matrix composition. The most notable change here is a depletion of ceramides and long chain fatty acids (Shao et al., 2016; Wolf & Wolf, 2012).

The typical treatment of skin diseases is the application of ointments and creams, whose task is to ensure sufficient skin hydration and provide a healing environment. The most widely used therapy is application of corticosteroids and calcineurin inhibitors. These drugs are however administered in a form of suspension or dispersion, which are forms that cannot ensure the best biological availability of topically applied drugs. For this reason, we focus on the development of an alternative therapy concerning the direct application of the skin lipids, namely ceramides that help to restore the disrupted skin barrier properties.

Currently, we have a very effective liposomal system containing skin lipids with a composition imitating the SC lipid matrix – so called cerosomes. These cerosomes

https://doi.org/10.24355/dbbs.084-202110251021-0

are able to effectively restore chemically disrupted skin barrier (Vovesná, Zhigunov, Balouch, & Zbytovská, 2021). However, their effect is directed only to the outer surface disease manifestations. It is therefore vital to enhance this system and target even the pathophysiological processes in the deeper skin layers. For this purpose, we already have an experience with hydrocortisone-loaded cerosomes. Nevertheless, the encapsulation efficiency of cerosomes was not ideal and the system would not be as effective as needed. Typically for a topical administration of drugs, we use another carriers – lipid nanocapsules (LNCs). These nanoparticles are stable for a long time with great capability to encapsulate wide variety of drugs, including HC. We also know, that LNCs help to concentrate HC into SC and epidermis; however, they do not restore the skin barrier.

For this reason we aim to create a combined system of cerosomes and LNCs with encapsulated anti-inflammatory drug (eg. hydrocortisone). We will characterize the morphology of prepared particles and ultimately test their efficacy in disrupted skin repair and HC administration.

RESEARCH CONCEPT

Preparation of cerosomes-LNC system

The cerosomes are prepared by modified method of thin lipid film hydration. At first, all the lipids, ceramides 3 and 6, cholesterol and stearic acid are weighed in a round bottom flask and dissolved in a chloroform : methanol mixture. Hydrocortisone (HC) or HC-butyrate (HC-B) is added to this mixture as well. The ratio of these lipids and the drug is equimolar to best simulate the environment in the lipid matrix and to introduce sufficient amount of the drug into the formulation (Table 1). The solvents are then evaporated on a rotary evaporator until a thin film is formed on the walls of the flask. This film is further hydrated by phosphate buffered saline (PBS) solution with 10 % urea addition (PBS+U). The flask is alternatively placed in a heater on 95 °C and shook on a vortex until all the lipids from the flask walls are dissolved. Next, LNCs are prepared by the phase inversion temperature method (Heurtault, Saulnier, Pech, Proust, & Benoit, 2002). An MCT oil (Miglyol 812 N), nonionic (Kolliphor HS 15) and amphoteric (Phospholipon 90G) surfactants are weighed in a beaker. HC or HC-B are also added to this mixture. PBS with 10 % addition of urea (PBS+U) is added and the whole is placed on a heater (Table 1). The mixture is heated three times in the range from 50 to 85 °C. After the third heating cycle, the mixture is diluted with ice cold PBS+U. The cold shock induces the nanoparticle formation and also the encapsulation of the drug.

Table 1: Composition of prepared nanoparticular systems.

Cerosomes			LNCs	
Compound	**wt%**	**wt%**	**Compound**	**wt%**
Ceramide 3	0.18	0.17	Miglyol	30.0
Ceramide 6	0.18	0.18	Kolliphor	20.0
Cholesterol	0.22	0.26	Phospholipon	1.5
Stearic acid	0.24	0.23	HC, HC-B	0.75
HC	0.18		PBS+U	15.0
HC-B		0.17	PBS+U (0°C)	32.75
Urea	10.0	10.0		
PBS	89.0	89.0		

To combine these two systems, we took two approaches. One is to add the LNCs to the cerosomes. A freshly prepared batch of LNCs was added onto the thin lipid cerosomal film. The film was then hydrated and vortexed the same way as described above. The second variation of the preparation is to add the cerosomes to the LNCs. At first, cerosomes were prepared as described and then they were added to the LNC preparation instead the sole PBS+U.

Particle characterization

We characterized our nanoparticulate systems by dynamic light scattering (DLS) in order to get the information about the size of present particles. We describe our systems by number mean values of the size when we show characteristics of sole cerosomes or LNCs. Then to describe the combined system, we use volume mean values of the size for the reason that it is crucial to see both types of the particles largely differing in their sizes.

We also established the encapsulation efficiency (EE) of cerosomes, LNCs and cerosomes-LNCs for hydrocortisone and hydrocortisone-butyrate. The EE was determined by ultrafiltration of a sample through Centrisart 20 kDa MWCO filtration units and subsequent analysis of the supernatant.

https://doi.org/10.24355/dbbs.084-202110251021-0

RESULTS AND DISCUSSION

At first, we prepared and characterized both systems (cerosomes and LNCs) respectively to find the maximal content of the drug (HC, HC-B) and other limits for both formulations. Loading cerosomes with a drug like HC or HC-B did not pose any challenge in terms of preparation conditions. It was possible to hydrate the lipid films containing both drugs in normal hydrating time and temperature (6 h, 95 °C). The resulting liposomal formulation was of a smooth white appearance without any visible large particles, crystals or aggregates. The particles were stored in a dark place at laboratory temperature in order to minimize influences on the particle degradation. Liposomes prepared by film hydration method are large multilamellar vehicles with quite notable variations in size leading to higher values of polydispersity index (PDI). Our prepared cerosomes showed following characteristics: HC-cerosomes were of 651 ± 25 nm in size with PDI = 0.37 ± 0.12. HC-B-cerosomes did not differ significantly; they contained particles with size of 773 ± 45 nm, PDI = 0.45 ± 0.10. As the particle size is concerned, drug-loaded cerosomes were in every case smaller than cerosomes prepared without an API (active pharmaceutical ingredient). To show the difference, we can compare CER3+CER6 type of cerosomes prepared in our previous work (Vovesná et al., 2021). There we show the cerosomes to be 1196 ± 238 nm large with PDI of 0.15 ± 0.02. That is notably bigger size than HC or HC-B loaded cerosomes with the same composition. We assume that this fact can be ascribed to the molecular shape of both corticoids. The base structure of the sterol core of HC and HC-B is similar to the structure of cholesterol; therefore, HC could have the tendency to incorporate itself into the bilayered mixed structure of the cerosomes, opposed to more common adherence or bonding onto or into the liposomes. For this reason, we also chose the total content of HC and HC-B to be equimolar with all other components. Ultimately, the lipids form 1 % of the total formulation and HC or HC-B stand for approximately 0.18 % of total. The cerosomes as other liposomes do not possess great encapsulating capacity. That is also the main reason for this work on a combined system. In our case the encapsulation efficiency (EE) for HC was 25.3 ± 1.4 % and drug load (DL) 0.3 %. For HC-B these values were similar: $EE_{HCB,cersosomes}$ = 20.6 ± 0.9 and $DL_{HCB,cerosomes}$ = 0.2 ± 0.1 %. The encapsulation values around 20 % are in the expected range. DL usually reaches values < 10 % and for liposomes, these values are as always low.

The second formulation that forms the combination are the LNCs. The composition of the LNCs in this work was optimized to hold the highest amount of HC or HC-B possible without influencing the particle stability. The maximal content of the corticoids in LNCs is 0.75 % of the total formulation for both APIs. The size of empty LNC particles prepared with this composition (Table 1) is 101 ± 3 nm with PDI = 0.06. This size is comparable to other LNCs with quite same composition prepared in our laboratory (Pytlíková, 2020) that were sized circa 115 nm with PDI of 0.07. The introduction of an API into this system changed its characteristics only minimally. HC-LNC contained particles of 105 ± 2 nm, PDI = 0.08 and HC-B-LNC were sized 113 ± 1 nm, PDI = 0.09. These changes are very slight and can even be ascribed to variation in preparation and measurements. As was proposed, LNCs have great encapsulation ability for vast variety of drugs. Our system is not an exception, even though the selected corticoids are generally quite inert and insoluble. The EE for hydrocortisone was as high as 87.6 ± 3.1 % and DL was 1.0 ± 0.1 %. HC-B-LNCs encapsulated the drug by 85.8 ± 1.7 % with DL of 1.0 ± 0.1 % also. Additionally, all these characteristics did not change significantly during 2 weeks storage time, implying that HC and HC-B loaded LNCs are stable system capable to incorporate notable amount of the APIs.

For the last part of this work, we combined the two described systems in order to create a complex renewing and healing treatment for dermatitic conditions. The first approach was to use the HC(B)-LNCs as the aqueous phase for the HC(B)-cerosomes. However, the heating cycles at 95 °C seemed to disrupt and break the constitution of the LNCs due to such high applied heat. The DLS measurement revealed only particles sized around 1 μm, which suggests the presence of liposomal structures, but not the smaller LNC ones. It was not possible to lower the hydrating temperature for the ceramides would not hydrate in the needed time. We therefore applied another method for this combination. LNCs were again added onto the lipid film and the whole flask was placed in a water bath set at 40 °C and the mixture was intensely mixed overnight to simulate a kind of high shear homogenization conditions. After this time, the lipid film was completely hydrated from the flask walls; however, there could still be seen larger crystals of incompletely dissolved components of the formulation. The second approach to the preparation was to use the HC(B)-cerosomes as the aqueous phase of the HC(B)-LNCs. Their preparation process was not hindered by the exchange of PBS+U for the cerosomes

https://doi.org/10.24355/dbbs.084-202110251021-0

and was completed as described in the methods section. The resulting formulation was homogeneous, opalesque without visible particles. The DLS measurement confirmed the presence of two sizes of particles if evaluated by volume mean. For HC variation the first and larger peak was at 98 ± 2 nm at should belong to the LNC part of the combination. The second peak was visibly smaller and positioned at 835 ± 11 nm, which accords with the size of cerosomes. For HC-B the result was really similar. It was possible to obtain a formulation with two distinct sizes of 116 ± 5 nm and 956 ± 45 nm belonging to LNCs and cerosomes respectively. The EE and DL for this system are yet to be determined. Nevertheless, from the fact that the formulations did not contain any visible undissolved crystals, which it otherwise would if the HC and HC-B were not dissolved, we can expect the encapsulation rates to be at least as good as for the LNCs, but with the total amount of the API higher than in both sole formulations.

CONCLUSIONS

In this work we focused on a preparation of nanoparticulate systems for topical delivery of hydrocortisone and hydrocortisone-butyrate. It was possible to prepare lipid nanocapsules containing 0.75 % of HC or HC-B with 85 % encapsulation efficiency. Next, we successfully prepared cerosomes mimicking the composition of *stratum corneum* lipid matrix loaded with 0.18 % of HC and HC-B. In order to enhance the efficiency of dermatitic conditions treatment, we successfully combined the two systems and characterized it for the presence of both formulations. We propose that such complex formulation has high potential in disrupted skin barrier treatment.

ACKNOWLEDGMENT

Acknowledgements: This work was supported from the OP RDE registration no.: CZ.02.2.69/0.0/0.0/19_073/0016928, funded by the ESF and Czech Science Foundation (GACR19-09600S). We also thank IOI Oleochemical for generous supply of Miglyol® 812 N.

SUBSCRIPT

API	Active pharmaceutical ingredient
DLS	Dynamic light scattering
EE	Encapsulation efficiency
HC	Hydrocortisone
LNC	Lipid nanocapsule
PBS	Phosphate buffered saline
SC	*Stratum corneum*
TEM	Transmission electron microscopy

REFERENCES

Harding, C. R. (2004): The stratum corneum: structure and function in health and disease. In: Dermatol. Ther., 17 Suppl 1, 6-15.

Heurtault, B., Saulnier, P., Pech, B., Proust, J. E., & Benoit, J. P. (2002): A novel phase inversion-based process for the preparation of lipid nanocarriers. In: Pharm Res, 19(6), 875-880.

Pytlíková, S. (2020): Development of lipid nanoparticles containing hydrocortisone and its derivatives. (Diploma Thesis). UCT Prague.

Shao, M., Hussain, Z., Thu, H. E., Khan, S., Katas, H., Ahmed, T. A., Bukhari, S. N. A. (2016): Drug nanocarrier, the future of atopic diseases: Advanced drug delivery systems and smart management of disease. In: Colloids Surf. B, 147, 475-491. doi:10.1016/j.colsurfb.2016.08.027

Vovesná, A., Zhigunov, A., Balouch, M., & Zbytovská, J. (2021): Ceramide liposomes for skin barrier recovery: A novel formulation based on natural skin lipids. In: Int J Pharm, 596, 120264. doi:10.1016/j.ijpharm.2021.120264

Wolf, R., & Wolf, D. (2012). Abnormal epidermal barrier in the pathogenesis of atopic dermatitis. Clin. Dermatol., 30(3), 329-334. doi:10.1016/j.clindermatol.2011.08.023

https://doi.org/10.24355/dbbs.084-202110251021-0

load of an oral dosage form is as high as possible from a commercial point of view because smaller dosage forms and lower pill burden are typically better tolerated.[10] A higher drug load in turn often reduces the physical stability of the ASD formulation in terms of API crystallization.[11] From a thermodynamic perspective, the API is dissolved in an amorphous polymeric matrix. However, in many ASD formulations, the API content exceeds its solubility in the matrix at storage conditions: the ASD is thermodynamically unstable but kinetically stabilized due to low molecular mobility in the glassy ASD.[5, 6] In general, by increasing the drug load in kinetically stabilized ASDs, the degree of supersaturation of the dissolved API in the matrix and, therefore, the thermodynamic driving force for API crystallization is increased.[12] In addition, many APIs have a lower glass-transition temperature (T_g) than the polymer, leading to reduced T_g of the ASD with increasing drug load (**Figure *1***).[8, 13] Such a decrease of T_g increases the molecular mobility and therefore reduces kinetic stabilization of the ASD.[14, 15]

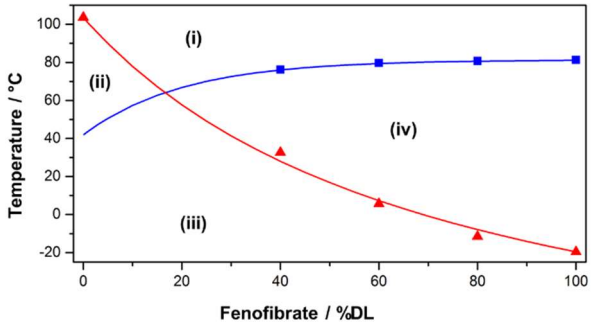

Figure 1: Exemplary phase diagram of a polymer-fenofibrate system.[9] The solubility temperature at different compositions is depicted in blue. The measured T_g values of different compositions are depicted in red. The symbols reflect measured data and the curves show modeling results. Different regions can be identified in the phase diagram: (i) thermodynamically stable melt, (ii) thermodynamically stable glass, (iii) kinetically stable glass and (iv) the undercooled or unstable melt, respectively.

The extend of stabilization and the required difference between storage temperature T and T_g of ASDs for avoiding API crystallization have been a matter of discussion in the literature for decades. As a rule of thumb, it has been assumed that a kinetically stabilized ASD needs to be stored at least 50 °C below T_g.[16] Assuming such an unnecessary high safety margin will hinder the development of high-drug load ASDs with low T_g. However, setting the safety margin to low will cause a potential patient safety risk. As a first measure to determine the physical stability of kinetically stabilized ASDs, long term stability studies have been conducted. In our studies we could show that no crystallization of the drug active is observed in ASDs of Nifedipine and Fenofibrate stored only 30 °C and even 8 °C below T_g after 15 years and 25 years of storage, respectively.[8, 9]

Despite those examples of long-term stability of kinetically stabilized ASDs, the demand for higher drug load and the occurrence of API crystallization in developmental stability studies makes it necessary for pharmaceutical development teams to have a proper risk assessment and mitigation strategy at hand. As time is of the essence in pharmaceutical development, we have developed a lean approach for API crystallization risk assessment in ASDs based on fast open dish studies, which excludes the patient risk of API crystallization over shelf-life storage while properly balancing the business risks involved (**Figure *2***).[17]

The starting point of the risk assessment is the standard open dish stress test at 40 °C / 75% RH. Ifcrystallization is detected in this study within 14 days of storage, an investigation of the crystallization risk is indicated. As in this stage of development crystallization is usually detected qualitatively by polarized light microscopy, the next step is to quantify the crystal growth and assign a rate constant. This investigation is performed in a Tier I investigation, preferably using TRS. In our experience, the non-destructive nature, inherent sample averaging, and chemometric data evaluation make this technology more than suited to quantify crystal growth in ASD samples. From our work on long term stability, we can assume that an ASD taking 14 days or longer to show complete API crystallization in an open dish experiment at 40 °C / 75% RH will not present a crystallization risk during shelf-life storage of the packaged material.[9] In cases where the ASD under investigation shows a considerable crystallization rate, the physical stability of alternate formulations can be compared in a Tier II study. A Tier III investigation is indicated if no alternate formulation with sufficient stability is found, or other reasons, like bioavailability or manufacturability, indicate the usage of a formulation considered not physically stable. In the Tier III investigation, the crystallization rate constant is measured for several storage conditions above T_g. The rate constants can be correlated with the ratio of T_g over T. Calculations of the moisture dependence of the T_g in the ASD and moisture content of the packaged DP can be used to determine the T_g of the product during storage.

https://doi.org/10.24355/dbbs.084-202110251021-0

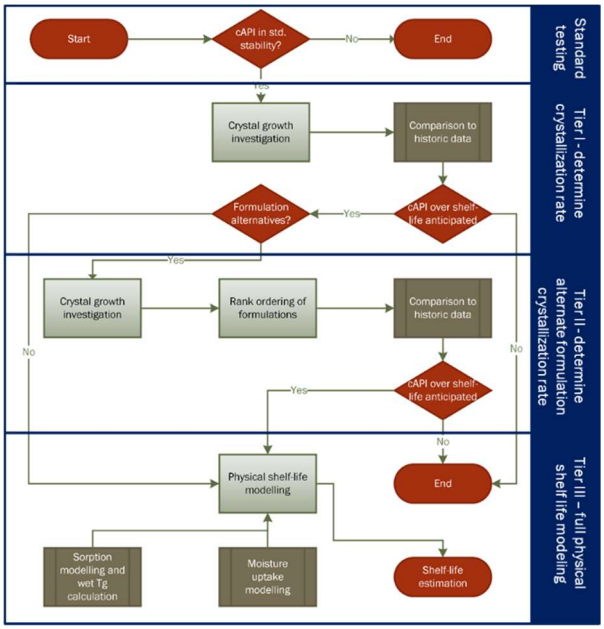

Figure 2: Workflow of the physical shelf life modelling risk assessment strategy for crystallization in ASD formulations. An investigation of the physical stability is indicated if API crystallization is observed in the standard open dish stability investigation at 40 °C / 75% RH within two weeks. In a Tier I investigation, the rate of crystallization in the ASD is determined. If crystallization is sufficiently fast to indicate a shelf life risk, the crystal growth rate in alternate formulations is determined in a Tier II investigation. If no sufficiently stable formulation can be used, a Tier III investigation is indicated and the crystal growth of the DP in the primary packaging container is approximated.

RESULTS

The risk assessment strategy is now routinely applied to AbbVies ASD development candidates. The application of the complete risk assessment strategy on a model compound will be presented in this talk. After crystallization of the lead formulation candidate was observed in an open dish study, the rate of crystallization was determined and compared to alternate formulations (**Figure *3***). As the lead formulation had shown complete API crystallization within 3 days at 40 °C / 75% RH open dish condition, an estimation of the physical shelf-life was indicated. Based on predicted water content of the blister packaged DP and calculated impact of water on the products T_g, a shelf-life till crystallinity limit of 67 months could be estimated.

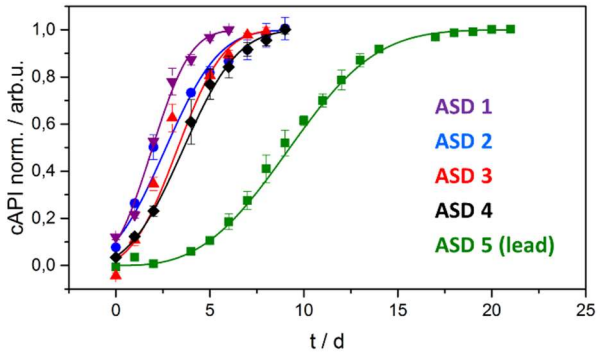

Figure 3: Crystal growth in five different ASD formulation candidates of an AbbVie internal compound. The crystal growth was recorded in samples stored at 30 °C / 75 %RH (open dish) using TRS. The fraction of crystallized API normalized to total API is shown in dependence of time.

DISCUSSION

Our investigations of nifedipine and fenofibrate ASD DPs present, up to now, the only long-term stability investigations of kinetically stabilized ASDs in the literature and proved that such DPs can be safe over the shelf-life, even if stored only a few degrees below T_g. As crystallization still might occur in accelerated stability studies, pharmaceutical development teams require a strategy to assess and mitigate crystallization risk. An essential step in developing the presented fast risk assessment approach was determining the relation of the API crystallization rate with the environmental conditions. In the literature, different attempts can be found from simple Arrhenius extrapolation approaches to linking the crystallization with relaxation time in glasses. Utilizing recent glass physics approaches, we could successfully correlate the logarithm of the crystallization rate with the ratio of T_g over T. Combining this approach with the modeling of the water uptake of the packaged DP and the water induced change in T_g, we were able to estimate crystal growth in packaged DP based on fast open dish studies. Applying the risk assessment and mitigation strategy as presented in **Figure *2*** is aiding project development teams in making proper decisions regarding the crystallization risk of the ASD DP. In cases where crystallization of the API over the shelf-life is anticipated, a safe shelf-life range or an alternate packaging material can be suggested.

CONCLUSIONS

With the results presented in this work, crystallization observed in open-dish studies is no longer a

https://doi.org/10.24355/dbbs.084-202110251021-0

showstopper in ASD development. Using historical examples, the possibility of long-term stability in kinetically stabilized ASDs even if stored only a few degrees below T_g could be shown. Utilizing recent results of the investigation of glass physics in ASDs and combining them with physical modeling tools, a risk assessment and mitigation framework for API crystallization in ASD formulation could be developed. The framework enables drug development teams to conduct rational risk-based actions in ASD development. It allows to successfully bring ASD formulations to market that were just a couple of years ago discontinued due to perceived stability issues.

ACKNOWLEDGMENT

Numerous AbbVie employees were involved in developing, producing and analyzing the presented examples. Their contributions are highly appreciated. We'd like to especially thank Jörg Rosenberg for having the foresight to store ASD samples over decades for later analysis and Sankaran Anantharaman as well as Holger van Lishaut for initiating the development of the risk assessment and mitigation approach. All authors are employees of AbbVie and may own AbbVie stock. AbbVie sponsored and funded the study; contributed to the design; participated in the collection, analysis, and interpretation of data, and in writing, reviewing, and approval of the final publication.

REFERENCES

1. Thayer, A.M., *FINDING SOLUTIONS.* Chemical & Engineering News Archive, 2010. **88**(22): p. 13-18.
2. Waring, M.J., et al., *An analysis of the attrition of drug candidates from four major pharmaceutical companies.* Nature Reviews Drug Discovery, 2015. **14**(7): p. 475-486.
3. Schittny, A., J. Huwyler, and M. Puchkov, *Mechanisms of increased bioavailability through amorphous solid dispersions: a review.* Drug Delivery, 2020. **27**(1): p. 110-127.
4. Pandi, P., et al., *Amorphous solid dispersions: An update for preparation, characterization, mechanism on bioavailability, stability, regulatory considerations and marketed products.* International Journal of Pharmaceutics, 2020. **586**: p. 119560.
5. Lehmkemper, K., et al., *Long-Term Physical Stability of PVP- and PVPVA-Amorphous Solid Dispersions.* Mol Pharm, 2017. **14**(1): p. 157-171.
6. Zhou, D., et al., *Assessing Physical Stability Risk Using the Amorphous Classification System (ACS) Based on Simple Thermal Analysis.* Molecular Pharmaceutics, 2019. **16**(6): p. 2742-2754.
7. Yu, L., *Amorphous pharmaceutical solids: preparation, characterization and stabilization.* Advanced Drug Delivery Reviews, 2001. **48**(1): p. 27-42.
8. Theil, F., et al., *Frozen in Time: Kinetically Stabilized Amorphous Solid Dispersions of Nifedipine Stable after a Quarter Century of Storage.* Mol Pharm, 2017. **14**(1): p. 183-192.
9. Theil, F., et al., *Extraordinary Long-Term-Stability in Kinetically Stabilized Amorphous Solid Dispersions of Fenofibrate.* Molecular Pharmaceutics, 2017. **14**(12): p. 4636-4647.
10. Mudie, D.M., et al., *A novel architecture for achieving high drug loading in amorphous spray dried dispersion tablets.* International Journal of Pharmaceutics: X, 2020. **2**: p. 100042.
11. Gupta, P., V.K. Kakumanu, and A.K. Bansal, *Stability and Solubility of Celecoxib-PVP Amorphous Dispersions: A Molecular Perspective.* Pharmaceutical Research, 2004. **21**(10): p. 1762-1769.
12. Zhou, D., et al., *Thermodynamics, molecular mobility and crystallization kinetics of amorphous griseofulvin.* Mol Pharm, 2008. **5**(6): p. 927-36.
13. Amharar, Y., et al., *Solubility of crystalline organic compounds in high and low molecular weight amorphous matrices above and below the glass transition by zero enthalpy extrapolation.* Int J Pharm, 2014. **472**(1-2): p. 241-7.
14. Kothari, K., V. Ragoonanan, and R. Suryanarayanan, *Influence of molecular mobility on the physical stability of amorphous pharmaceuticals in the supercooled and glassy States.* Mol Pharm, 2014. **11**(9): p. 3048-55.
15. Hancock, B.C., S.L. Shamblin, and G. Zografi, *Molecular mobility of amorphous pharmaceutical solids below their glass transition temperatures.* Pharm Res, 1995. **12**(6): p. 799-806.
16. Amidon, G.L., et al., *A theoretical basis for a biopharmaceutic drug classification: the correlation of in vitro drug product dissolution and in vivo bioavailability.* Pharm Res, 1995. **12**(3): p. 413-20.
17. Liu, B., et al., *Crystallization Risk Assessment of Amorphous Solid Dispersions by Physical Shelf-Life Modeling: A Practical Approach.* Mol Pharm, 2021. **18**(6): p. 2428-2437.

https://doi.org/10.24355/dbbs.084-202110251021-0

IN-LINE UV-VIS SPECTROSCOPY IN SMALL SCALE EXTRUSION AS PROCESS ANALYTICAL TECHNOLOGY DURING EARLY STAGE DEVELOPMENT OF AMORPHOUS SOLID DISPERSIONS

J. Winck[1], M. Daalmann[1], M. Thommes[1]

[1] TU Dortmund University; Emil-Figge-Str. 68; Dortmund / Germany; judith.winck@tu-dortmund.de

ABSTRACT

The poor solubility of a large number of active pharmaceutical ingredients (API) is a major challenge in pharmaceutical research. Therefore, the extrusion of amorphous solid dispersions (ASDs) is one promising approach to enhance the dissolution rate by molecularly dissolve the API in an amorphous carrier polymer. During ASD development, crucial parameters as the dissolution and the decomposition need to be monitored. Within this study, a small scale twin screw extruder was coupled with special ColVisTec UV-Vis probes that are characterized by their small dimensions. This setup enables a systematic formulation development and optimization based on in-line monitoring of crucial parameters using small amounts of material.

Keywords: hot melt extrusion (HME), micro compounder, formulation development, process analytical technology (PAT), UV-Vis spectroscopy

INTRODUCTION

A large number of the active pharmaceutical ingredients (API) that are on the market and the majority of those currently under development have a low solubility [Rodriguez-Aller, 2015]. However, the dissolution process is crucial for the systematic absorption of the active ingredient in the human body. A low solubility of APIs therefore often leads to a low bioavailability and thus an insufficient efficacy.

A common approach to improving bioavailability is to increase the rate of dissolution of the API by administering it in the amorphous state in which the energy to overcome the crystal lattice has already been applied. For the kinetic stabilization of the amorphous state, the active ingredient is embedded in an amorphous carrier polymer with high viscosity, creating an amorphous solid dispersion (ASD) [Vasconcelos, 2007].

Hot melt extrusion (HME) enables a solvent-free production of ASDs by mixing and dispersing processes inside the extruder. In order to process the highly viscous polymers, extrusion processes are usually carried out at elevated temperatures. Furthermore, the solubility temperature has to be reached, which states the minimum required temperature for a specific API content to be soluble in the carrier polymer. However, extrusion at elevated temperatures can cause mechanical as well as thermal decomposition, especially if polymer or API molecules are thermally unstable [Matić, 2020].

In ASD development, this interplay of completely dissolve the API and simultaneously avoid decomposition is a major challenge. Therefore, appropriate process conditions need to be identified during early stage process development. Within this study, the integration of an in-line UV-Vis spectrophotometer during small scale extrusion of ASDs is evaluated in order to develop a fast-working method to optimize process conditions based on reduced material consumption.

RESEARCH CONCEPT

Materials

Two formulations with different drug loads were investigated. Griseofulvin (GRI) (Fagron, Rotterdam, Netherlands) and Itraconazole (ITR) (Ria International India Pvt Ltd, Madurai, India) were used as model drugs.

https://doi.org/10.24355/dbbs.084-202110251021-0

Copovidone (PVPVA) (Plasdone S-630, Ashland Inc., Switzerland) was used as carrier polymer.

Extrusion

The extrusion was carried out using a DSM xplore micro compounder (Xplore Instruments BV, Sittard, Netherlands), a laboratory scale extruder with two intermeshing conical screws, a capacity of about 5 ml, and a die diameter of 3 mm. An air-cooled hopper was used in order to prevent the materials from sticking. 3 g of formulation were fed into the extruder, respectively. The screw speed was set to 50 rpm throughout the whole study. The residence time of the material was set by operating the extruder in the recirculation mode. Therefore, the valve between the screw tips and the die was turned to the recirculation channel and opened immediately after the desired residence time. The material temperature was adjusted by the barrel temperature and calibrated beforehand by using a Testo 875 IR camera (Testo SE & Co. KGaA, Lenzkirch, Germany).

A systematic parameter study was performed for three different drug weight fractions w, as listed in Table 1. Seven different temperatures in specific distance ΔT to the expected solubility temperature T_s were selected [Gottschalk, 2021]. For each temperature, the extrusion was performed with three different residence times t in order to investigate its influence in addition.

Table 1: Process conditions during the extrusion of GRI/PVPVA and ITR/PVPVA.

Parameter	Unit	Values
w (GRI/PVPVA)	[-]	0.15, 0.20, 0.25
w (ITR/PVPVA)	[-]	0.25, 0.30, 0.35
Residence time	[min]	1, 3, 10
ΔT to T_s	[K]	-10, -7, -3, 0, 3, 7, 10

Optical analysis

The presence of remaining drug crystals and coloring was investigated by a visual method. Therefore, the extrudates were placed on a black background and besides a yellowish coloring it was detected, whether they are transparent or opaque. Thereby, a transparent extrudate was assessed as an amorphous solid dispersion whereas an opaque extrudate was considered to contain unresolved crystals.

UV-Vis spectroscopy

The in-line UV-Vis spectroscopy was performed with an Inspectro X spectrophotometer (ColVisTec, Berlin, Germany) in the transmission mode. Due to the small dimensions of the extruder and the die channel a special pair of ColVisTec probes was implemented into the experimental setup that differ from the standard TPMP probes. A range of 224 to 820 nm and a sampling rate of 1 Hz was chosen. The obtained spectra were calibrated by using spectra of the pure polymer as a blank reference.

RESULTS AND DISCUSSION

In addition to the optical analysis and transmission spectra (data not shown), the extrusion of ADSs is evaluated based on the L* and b* value of the CIELAB color specification system. More specifically, the lightness increases with an increasing L* value, indicating the API dissolution in the polymer. Color changes from blue to yellow are represented by the b* value.

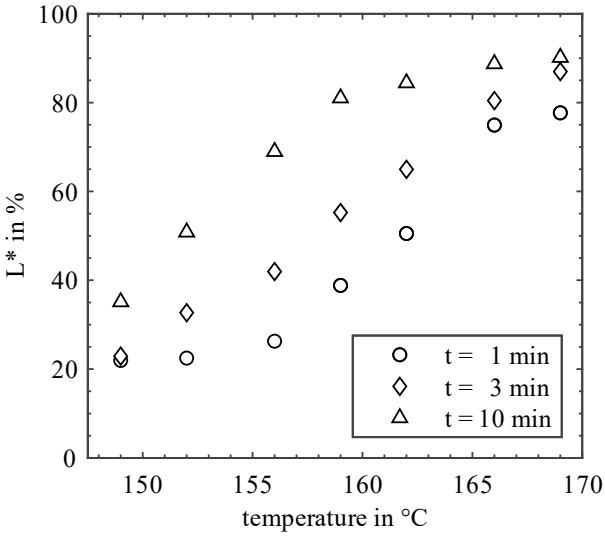

Figure 1: L* value of GRI/PVPVA/0.15 as a function of temperature and residence time.

Exemplary results shown for GRI/PVPVA/0.15 in figure 1 clearly indicate that the L* value increases with increasing temperature. In addition, an increase in the L* value with increasing residence time can be seen for a certain temperature. In particular at the temperatures of 156 °C, 159 °C and 162 °C, the major changes of L* values for different residence times can be found in comparison to the other temperatures. This shows that by reaching the solubility temperature of 159 °C and in a small temperature range of 3 °C below and above the

https://doi.org/10.24355/dbbs.084-202110251021-0

solubility temperature, an increasing lightness occurs. Here, the active ingredient is increasingly dissolved in the carrier polymer, so that the crystalline components decrease and the lightness increases as a result.

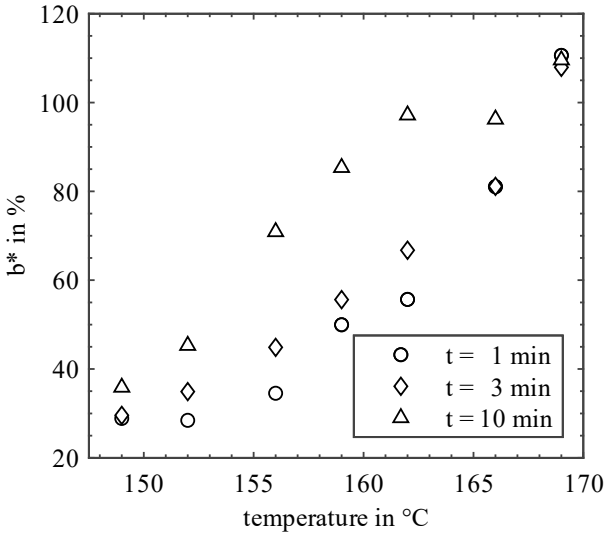

Figure 2: b* value of GRI/PVPVA as a function of temperature and residence time.

Figure 2 shows the influence of the residence time and the temperature on the b* value for GRI/PVPVA/0.15. An increase in the b* value can be seen for both increasing temperatures and increasing residence times. This is caused by an increasing thermal and mechanical stress resulting in material decomposition and thus a yellow or brown discoloration of the ASDs. Similar trends were also obtained for the other formulation ITR/PVPVA as well as for any drug weight fraction (data not shown).

CONCLUSIONS

A special UV-Vis probe, which measures low material quantities inside the small scale extruder, was integrated into the process. Based on a comparison with an optical inspection of the extrudates, the suitability of the in-line UV-Vis spectroscopy was confirmed. With the transmission spectra and the lightness value L*, remaining crystalline components were detected and thus the formation of ASDs could be assessed. Since color values were also determined, conclusions regarding the material decomposition were drawn.

The influence of temperature and residence time on the formation of ASDs was quantified. By comparing the temperature required for dissolution with the temperature of decomposition for a specific API content and residence time, suitable process regimes can be identified to finally optimize the whole process development.

ACKNOWLEDGMENT

The authors thank ColVisTec (Andreas Berghaus) and Ashland (Christian Muehlenfeld) for their technical support.

REFERENCES

Gottschalk, T.; Grönniger, B.; Ludwig, E.; Wolbert, F.; Feuerbach, T.; Winck, J.; Sadowski, G.; Thommes, M. (2021): Influence of residence time in manufacturing amorphous solid dispersions via hot melt extrusion. In: Proceedings of the 12th World Meeting on Pharmaceutics, Biopharmaceutics and Pharmaceutical Technology

Matić, J., Alva, C., Witschnigg, A., Eder, S., Reusch, K., Paudel, A.; Khinast, J. (2020) Towards predicting the product quality in hot-melt extrusion: Small scale extrusion. In: International journal of pharmaceutics: X 2, 100062. DOI: 10.1016/j.ijpx.2020.100062

Rodriguez-Aller, M.; Guillarme, D.; Veuthey, J.-L.; Gurny, R. (2015) Strategies for formulating and delivering poorly water-soluble drugs. In: Journal of Drug Delivery Science and Technology 30, 342–351. DOI: 10.1016/j.jddst.2015.05.009

Vasconcelos, T.; Sarmento, B.; Costa, P. (2007): Solid dispersions as strategy to improve oral bioavailability of poor water soluble drugs. In: Drug discovery today 12, 1068–1075. DOI: 10.1016/j.drudis.2007.09.005

https://doi.org/10.24355/dbbs.084-202110251021-0

BIPHASIC BIOCATALYTIC TESTOSTERONE DEHYDROGENATION IN MICROFLUIDIC DROPLETS

L. Xiang[1,2], J. Solarczek[3], A. Schallmey[3], I. Constantinou[1,2]

[1] Technische Universität Braunschweig, Institute for Microtechnology; 38124; Braunschweig, Germany; l.xiang@tu-braunschweig.de

[2] Technische Universität Braunschweig, Zentrum für Pharmaverfahrenstechnik (PVZ); 38106; Braunschweig, Germany

[3] Technische Universität Braunschweig, Institute for Biochemistry, Biotechnology and Bioinformatics; 38106; Braunschweig, Germany

ABSTRACT

Two-phase biocatalysis is commonly used for the bioconversion of water-insoluble chemical and pharmaceutical compounds. In research laboratories, such processes often take place in flasks and are driven and limited by slow diffusive processes. In this work, we developed droplet-based microfluidic systems and used them to perform testosterone dehydrogenation. The use of microdroplets as reaction vessels offers the advantage of greatly improved diffusion rates due to significantly increased surface-to-volume ratio. We found that indeed reaction time was reduced from tens of minutes to tens of seconds without sacrificing conversion efficiency. This demonstrates the potential of droplet-based two-phase biocatalysis.

Keywords: two-phase biocatalysis, microdroplets

INTRODUCTION

In biocatalysis, enzymes or whole cells are used as catalysts for chemical transformations. Compared to chemical methods, biocatalysis offers several advantages such as high specificity, environmental friendliness, and reduced energy requirements due to reactions at room temperature and atmospheric pressure [Anthonsen, 2000; Faber, 2011].

Enzymes used as catalysts for chemical reactions are generally less stable in organic media compared to their natural aqueous environment, but chemical and pharmaceutical compounds are often insoluble in water [Klibanov, 2001]. The use of aqueous/organic two-phase systems provides a solution to this problem. Such two-phase systems are now commonly used in multiple biotransformations [Adebar, 2019]. The addition of a non-polar organic phase as a substrate reservoir and product sink can ensure high substrate loadings while avoiding enzyme inhibition or inactivation.

Figure 1 shows a simplified example of a traditional aqueous/organic two-phase system. In this configuration, biocatalysis is driven by diffusion. The substrate diffuses into the aqueous phase, where it is converted by the enzyme. In turn, the product diffuses back into the organic phase, where it is collected. Diffusion is often facilitated by shaking the flasks or stirring their contents. Mixing increases the contact area between the two phases, but at the same time mechanical stress associated with shaking or stirring can cause enzyme denaturation. The formation of emulsions during stirring is also a limitation of such systems, as phases are difficult to separate for product collection. Additionally, the amount or type of organic phase can also have an inhibitory effect on the reaction, as it can impede enzyme activity.

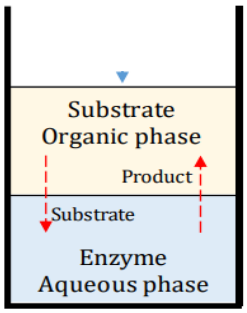

Figure 1: Aqueous/organic biphasic system

RESEARCH CONCEPT

In this work, we designed, fabricated, and tested microfluidic devices for droplet-based two-phase biocatalysis on-chip. The use of microfluidic droplets as

https://doi.org/10.24355/dbbs.084-202110251021-0

miniaturized reactors offers the advantage of greatly improved diffusion rates due to the significantly increased surface-to-volume ratio [Žnidaršič-Plazl, 2014; Fernandes, 2010]. In turn, higher diffusion rates can increase the reaction conversion rate. Another advantage of microfluidic droplets is lack of mechanical stress associated with their formation and their relative ease of separation compared to emulsions created by active mixing in flasks. Microdroplet separation ensures efficient product extraction.

ENZYME-BASED BIOCATALYTIC REACTION

17β-Hydroxysteroid dehydrogenases (17β-HSDs) are a type of NAD(P)-dependent oxidoreductases. Their main function is to participate in the metabolism of sex hormones by controlling the last step in the formation of androgens and estrogens. Thus, they play an important role in reproduction [Oppermann, 1996; Benach, 1996]. Herein, 17β-hydroxysteroid dehydrogenase is used for testosterone dehydrogenation to androstenedione, as shown in Figure 2 below.

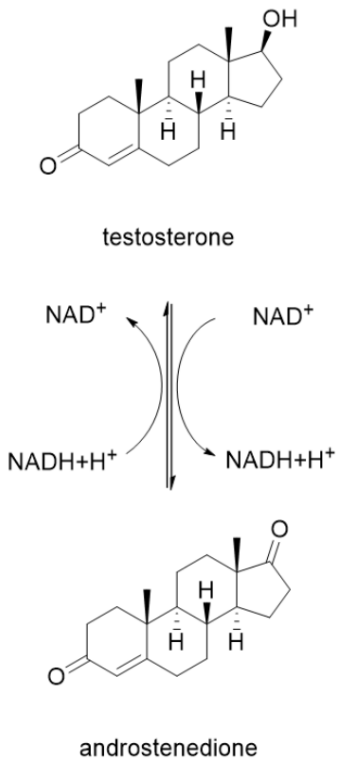

Figure 2: Conversion of testosterone to androstenedione catalyzed by 17β-hydroxysteroid dehydrogenase.

Androstenedione can be used as a precursor of hormones, such as male hormones and protein synthesis hormones, and can be used to synthesize pharmaceuticals such as spironolactone, hydrocortisone, prednisone oxide, and dexamethasone [Elks, 2014]. Testosterone is the main protein assimilation substance, and it is of great significance to health, affecting, among others, sexual desire, strength, and immune function [Mooradian, 1987].

MICROFLUIDIC DEVICE DESIGN AND FABRICATION

There are three typical microfluidic device architectures used to generate droplets: T-junctions, flow-focusing devices, and co-flowing devices [i Solvas, 2011]. The experiments described in this work were carried out in flow-focusing devices.

The droplets produced have an oil-in-water (O/W) structure. The continuous phase is a buffer containing the enzyme, and the discrete phase is an organic solvent containing the substrate testosterone. Figure 3 shows the geometry of the microfluidic device used in this study. To generate droplets, the continuous phase "squeezes" the fluid front of the dispersed phase from both sides of the intersection, and uses the "neck" structure of the channel downstream of the liquid front to form discrete droplets. The width of the continuous-phase microchannel, w_{con}, is 110 μm and the width of the discrete-phase microchannel, w_{di}, is 60 μm. The two phases converge in a narrow "neck" with a width of 50 μm and form droplets in a 400 μm channel.

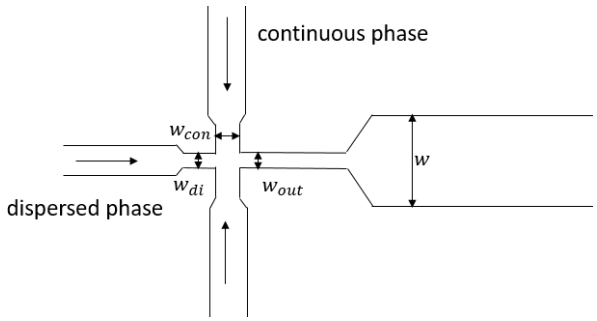

Figure 3: Geometry of microfluidic device used for droplet generation.

The microfluidic devices were fabricated in glass using femtosecond laser ablation. Glass was chosen due to its chemical inertness, which ensures no effects on the biocatalytic reaction. After laser ablation of microchannels, the glass wafer with a thickness of 700 nm was etched in hydrofluoric acid to remove surface defects, followed by cleaning in piranha solution (a mixture of sulfuric acid, water, and hydrogen peroxide), accompanied by an increase in surface hydrophilicity. To seal the microfluidic channels, the base wafer was thermally bonded to a cover glass wafer. The finished microfluidic device was therefore made exclusively out of transparent glass, which also allows the use of microscopy for process monitoring.

https://doi.org/10.24355/dbbs.084-202110251021-0

REACTION DETAILS

The aqueous phase and organic phase solutions were prepared before the start of the experiment. 50 µl of a 10 µg/µl enzyme solution, 1000 µl of 20 mM nicotinamide adenine dinucleotide (NAD^+) and 3450 µl of buffer were mixed to form the aqueous phase. The buffer was composed of 20 mM Tris-HCl and 25 mM sodium chloride at pH 9. Methyl tertiary butyl ether (MTBE) was chosen as the organic solvent, in which the concentration of testosterone was 10 mM. In addition, 1% Tween 20 was added to the aqueous phase as a surfactant to reduce the surface tension and promote the formation and stabilization of the droplets.

CONTINUOUS BIOCATALYTIC REACTIONS IN MICRODROPLETS

Syringe pumps were used to push the organic and aqueous phase into microchannels, and experiments were carried out at two flow rates. In sample 1, the flow rate of the organic phase was 1.5 µl/min, and the flow rate of the aqueous phase was 4.5 µl/min. In sample 2, the flow rates of the organic and aqueous phases were 3 µl/min and 9 µl/min, respectively. At the outlet of the microfluidic system 250 µl of liquid was collected for analysis. Ethyl acetate was added to the collection container at a ratio of 1:1 (ethyl acetate to reaction solution) to terminate the reaction. In addition, a 6 cm-long PTFE tube with an inner diameter of 0.25 mm was installed at the outlet of the glass microfluidic chip to provide a longer residence time for the reaction. The residence time (i.e. reaction time) of the reaction solution in the system was approximately 40 s (sample 1) and 20 s (sample 2).

The droplets generated in the microchannel are shown in Figure 4. The average droplet diameter was approximately 80 µm.

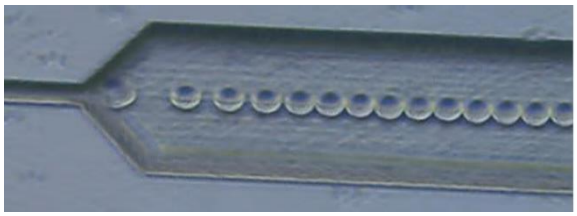

Figure 4: Microdroplets in the microchannel. The flow rate of the organic phase is 1.5 µl/min, and the flow rate of the water phase is 4.5 µl/min. Observed under a microscope. For scale, the width of the microchannel that contains droplets is 400 µm.

RESULTS AND DISCUSSION

High performance liquid chromatography (HPLC) was used for the detection of substrate and product in the solution. Figure 5 below shows the chromatogram of the reaction in sample 1. By calculating the ratio of the peak areas of the product and the substrate, the conversion of the substrate testosterone to the product androstenedione in the two reactions was determined as follows: sample 1: 91%, sample 2: 85%. The corresponding amount of the produced product were 0.5687 µmol and 0,53125 µmol, respectively.

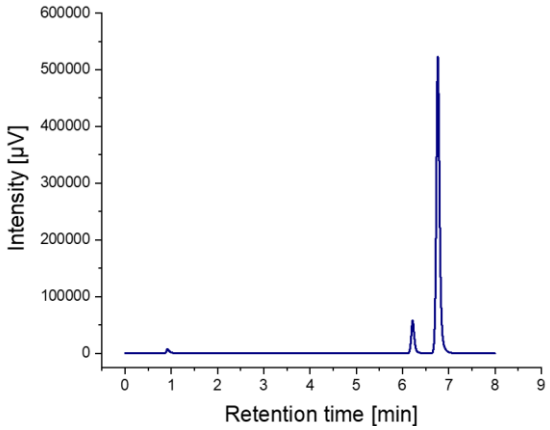

Figure 5: The chromatogram of the substrate and product in sample 1, where the abscissa represents the retention time and the ordinate represents the intensity. The retention times of testosterone and androstenedione are 6.2 min and 6.8 min respectively.

The same experiment was performed in a conventional batch reaction at the same substrate concentration of 10 mM and stirring at 900 rpm. The concentration of enzyme in the buffer was 50 µg/ml. As using large amounts of organic solvent can affect the activity of the enzyme, the ratio of the organic to aqueous phase used was 1:9. At a reaction time of 10 minutes, the conversion rate was 85 %. After 15 minutes, the conversion rate increased to 93 %.

CONCLUSIONS

The dehydrogenation reaction of testosterone catalyzed by 17β-HSD was realized in microdroplets and was compared to traditional batch experiments. We found that high conversion rates can be achieved in such miniaturized systems in significantly less time (tens of seconds) compared to the traditional setup (tens of minutes). This is partially due to much higher diffusion rates achieved in microsystems facilitated by the large droplet surface-to-volume areas. Therefore, such miniaturized reactors are a promising platform for the performance of two-phase biocatalysis.

ACKNOWLEDGMENT

This work has been performed within the framework of the SMART BIOTECS alliance between the Technische Universität Braunschweig and the Leibniz Universität

https://doi.org/10.24355/dbbs.084-202110251021-0

Hannover. This initiative is supported by the Ministry of Science and Culture (MWK) of Lower Saxony, Germany.

LX is financially supported through the 12plus6 initiative of the Faculty of Mechanical Engineering at Technische Universität Braunschweig.

NOMENCLATURE

w	the width of the microchannel, μm

SUBSCRIPT

con	continuous-phase
di	dispersed-phase
out	outlet

REFERENCES

Anthonsen, T. (2000): Reactions Catalyzed by Enzymes. In: Applied Biocatalysis (2nd ed.), S. 18–59.

Faber, K. (2011): Biocatalytic Applications. In: Biotransformations in Organic Chemistry (6th ed.), S. 29-333.

Klibanov, A. M. (2001): Improving enzymes by using them in organic solvents. In: Nature 409, S. 241–246. DOI: 10.1038/35051719.

Adebar, N.; Choi, J. E.; Schober, L.; Miyake, R.; Lura, T.; Kawabata, H.; Gröger, H. (2019): Overcoming Work-Up Limitations of Biphasic Biocatalytic Reaction Mixtures Through Liquid-Liquid Segmented Flow Processes. In: ChemCatChem 11, S. 5788–5793. DOI: 10.1002/cctc.201901107.

Žnidaršič-Plazl, P. (2014): Enzymatic microreactors utilizing non-aqueous media. In: Chimica Oggi - Chemistry Today 32(1), S. 54-60.

Fernandes, P. (2010): Miniaturization in Biocatalysis. In: Int. J. Mol. Sci. 11(3), S. 858-879. DOI: 10.3390/ijms11030858.

Oppermann, U. C.; Maser, E. (1996): Characterization of a 3 alpha-hydroxysteroid dehydrogenase/carbonyl reductase from the gram-negative bacterium Comamonas testosterone. In: European Journal of Biochemistry 241(3), S. 744-749. DOI: 10.1111/j.1432-1033.1996.00744.x.

Benach, J., et al. (1996): Crystallization and Crystal Packing of Recombinant 3 (or 17) β-Hydroxysteroid Dehydrogenase from Comamonas testosteroni ATTC 11996. In: European journal of biochemistry 236(1), S. 144-148. DOI: 10.1111/j.1432-1033.1996.t01-1-00144.x.

Elks, J. (2014): The Dictionary of Drugs: Chemical Data, Chemical Data, Structures and Bibliographies, S. 86.

Mooradian, A. D.; Morley, J. E.; Korenman, S. G. (1987): Biological actions of androgens. In: Endocrine Reviews 8 (1), S. 1–28. DOI: 10.1210/edrv-8-1-1.

i Solvas, X.C.; deMello, A. (2011): Droplet microfluidics: recent developments and future applications. In: Chemical Communications 47(7), S. 1936-1942. DOI: 10.1039/C0CC02474K.

https://doi.org/10.24355/dbbs.084-202110251021-0

IMPRINT

PUBLISHER

TU Braunschweig
Center of Pharmaceutical Engineering
Franz-Liszt-Str. 35a
38106 Braunschweig
Germany

The SPhERe 2021 is represented by
Prof. Dr.-Ing. Stephan Scholl
pvz-sphere@tu-braunschweig.de
www.pvz-sphere.de

SCIENTIFIC COMMITTEE & ORGANISATION

Dr. Gerlinde Benninger
Prof. Dr. Ludger Beerhues
Prof. Dr. Heike Bunjes
Prof. Dr. Andreas Dietzel
Prof. Dr.-Ing. Arno Kwade
Prof. Dr. Stephan Scholl (Conference Chair)

https://doi.org/10.24355/dbbs.084-202110251021-0